**TECHNISCHE
UNIVERSITÄT
WIEN**
Vienna University of Technology

_____

Dissertation

Experimental Investigation of Transition to Turbulence in a Torus

ausgeführt zum Zwecke der Erlangung des akademischen Grades eines

Doktors der technischen Wissenschaften unter der Leitung von

Univ. Prof. Dr. rer. nat. H. C. Kuhlmann

Institut für Strömungsmechanik und Wärmeübertragung

E 322

eingereicht an der

Technischen Universität Wien

Fakultät für Maschinenwesen und Betriebswissenschaften

von

DI Jakob Kühnen

9725513

Liechtensteinstr. 63/12, A-1090 Wien

Wien, im November 2012

_____

Unterschrift

Kurzfassung

Thema der vorliegenden Arbeit ist der Übergang einer laminaren (geordneten) Strömung zu einer turbulenten (chaotischen) Strömung in einem Torus. Die toroidale Geometrie steht hierbei als ein verallgemeinertes Modell für gekrümmte Rohre. Der Übergang zur Turbulenz in gekrümmten Rohren ist grundlegend anders als der Übergang in geraden Rohren. Das Einsetzen turbulenter Eigenschaften in Anwesenheit kleiner Störungen ist in gekrümmten Rohren zu deutlich höheren Reynolds-Zahlen (d.h. vor allem: zu höheren Strömungsgeschwindigkeiten) verschoben. Des Weiteren ändert sich auch das gesamte Übergangsszenario unter dem Einfluss der Rohrkrümmung fundamental. Eine vergleichsweise "sanfte" Abfolge von Übergängen statt eines plötzlichen, direkten Sprunges zu turbulenten Charakteristika ist zu beobachten. Ausgehend von einer stationären Grundströmung entwickelt sich bei steigender Reynoldszahl zunächst eine periodisch oszillierende Strömung, welche von einer quasi-periodischen und schließlich einer turbulenten Strömung mit chaotischem Verhalten abgelöst wird. Ein vergleichbares Übergangsszenario ist z.B. von der kanonischen Taylor-Couette-Strömung, der Strömung zwischen zwei konzentrisch rotierenden Zylindern, bekannt. Es entspricht dem Ruelle-Takens-Newhouse-Szenario, welches als eines von mehreren möglichen generischen Übergangsszenarien gilt.

Ziel der Arbeit war es, den Übergang zur Turbulenz in gekrümmten Rohren mittels modernster Messtechnik experimentell zu untersuchen. Besonderes Augenmerk wurde dabei auf die Untersuchung sogenannter "wandernder Wellen" bzw. kohärenter Strömungsstrukturen gelegt. Diese entwickeln sich oberhalb des ersten kritischen Transitionspunktes, der Grenze zwischen stationärer Grundströmung und periodisch oszillierender Strömung (primäre Instabilität). Das Hauptziel bestand darin, die physikalischen Eigenschaften und die wichtigsten Charakteristika der primären Instabilität sowie zumindest ansatzweise die nachfolgende Entwicklung bei höheren Reynolds-Zahlen (sekundäre und tertiäre Instabilität) in einem gekrümmten Rohr zu beschreiben.

Zu diesem Zweck wurde eine neuartige Versuchsanlage entworfen, aufgebaut, in Betrieb genommen und erfolgreich getestet. Mittels der Versuchsanlage kann eine exakt einstellbare Strömung in einem toroidalen Rohr erzeugt werden. Sie ist dahingehend optimiert, eine gekrümmte Rohrströmung mit nichtintrusiver Messtechnik bei beliebigen Durchflussraten bzw. Geschwindigkeiten zu untersuchen. Die Anlage besteht im Wesentlichen aus zwei runden Plexiglas-Scheiben, in welche jeweils eine konzentrische halbkreisförmige Nut gefräst wurde. Spiegelsymmetrisch aufeinandergelegt bilden die zwei Platten einen geschlossenen, toroidalen Hohlraum - ein (in sich) gekrümmtes Rohr. Die Strömung in dem geschlossenen Hohlraum wird durch eine rollende Stahlkugel unter Verwendung eines Magneten, der außerhalb auf einem rotierenden Arm angebracht ist, bewegt und angetrieben. Das Verhältnis von Krümmungsdurchmesser (Torusdurchmesser) D zu Rohrdurchmesser d beträgt bei allen in dieser Arbeit vorgestellten Ergebnissen 20,26.

Visuelle Beobachtungen, Laser-Doppler-Anemometrie, stereoskopische und hochfrequente Particle Image Velocimetry (S-PIV) sowie Druckdifferenzmessungen kamen bei den Experimenten zur Anwendung. Durch die Verwendung von S-PIV war es möglich, alle drei Komponen-

ten der Geschwindigkeitsvektoren in der Messebene, die den gesamten Querschnitt des Rohres umfasste, zu rekonstruieren. Da hydrodynamische Instabilitäten vor allem ein dynamisches Phänomen sind, ergaben die zeitaufgelösten S-PIV-Messungen ein umfassendes und vollständiges Bild des gesamten Strömungsfeldes während des Übergangs zur Turbulenz.

Bei der (kritischen) Reynolds-Zahl Re = $4080 \pm 2\%$ wurde ein superkritischer Übergang von einer stationären, laminaren Grundströmung zu einer laminaren Strömung, die in Strömungsrichtung periodisch moduliert ist, gefunden. Das auftretende Strömungsmuster ist nahezu ortsfest in einem Bezugssystem welches sich mit der die Strömung antreibenden Kugel bewegt, da die Wellengeschwindigkeit nur geringfügig oberhalb ($\sim 12\%$) der mittleren Geschwindigkeit der Strömung liegt. Die charakteristische Wellenlänge λ beträgt ca. $2d$ oder $11.25°$ für Re < 4350 und beginnt bei Re $\gtrsim 4350$ zwischen 2 und $4d$ zu schwanken. Gleich oberhalb der kritischen Reynoldszahl ist die Amplitude der Modulation in Strömungsrichtung sehr klein. Mit zunehmender Reynolds-Zahl wächst die Modulationsamplitude und die damit verbundenen Strömungsmuster werden deutlicher. Die Intensität der Geschwindigkeitsschwankungen in Strömungsrichtung liegt in der Größenordnung von bis zu 15% der mittleren Geschwindigkeit. Die Modulation des Geschwindigkeitsfeldes in Hauptstromrichtung konnte auch mit Druckdifferenzmessungen nachgewiesen werden. Zeitlich gemittelte Geschwindigkeitsprofile, insbesondere deren Veränderung bei Erhöhung der Reynolds-Zahl, sowie Untersuchungen des zeitabhängigen Strömungsfeldes im Bereich der ersten Instabilität werden in der vorliegenden Arbeit vorgestellt. Die Geschwindigkeitsschwankungen werden beschrieben und die Frequenzspektren mittels Fourieranalyse ausgewertet.

Eine einzelne Frequenz (f_1) und ihre 2. Harmonische ($2f_1$), die als "Fingerabdruck" der ersten Instabilität bezeichnet werden könnte, wurde in den Frequenzspektren im Bereich $4080 \leq$ Re $\lesssim 4400$ gefunden. f_1 ist auch noch bei höheren Reynoldszahlen, nach dem Einsetzen weiterer Frequenzen, nachweisbar und bleibt bis zum turbulenten Strömungszustand dominant. Bei der zweiten kritischen Reynoldszahl Re ≈ 4400 tritt ein Übergang zu einer Strömung mit zwei (oder eventuell mehr) Frequenzen f_1 und f_2 auf. Die beiden Frequenzen scheinen keinen gemeinsamen Teiler zu besitzen, also inkommensurabel zu sein. Somit wäre die Strömung quasi-periodisch. Der genaue Wert der zweiten Frequenz f_2 konnte lediglich auf einen Bereich nahe f_1 eingeschränkt, jedoch nicht eindeutig identifiziert werden. Der vermutlich quasiperiodische Zustand existiert bis zu Reynoldszahlen > 6000, deutlich dominiert von f_1. Einiges deutet darauf hin, dass die zweite Instabilität auf einer Instabilität der viskosen Grenzschicht beruht. Der Übergang bei noch höheren Reynolds-Zahlen zu eindeutiger Turbulenz mit breitbandigem Frequenzspektrum scheint in verschiedenen Bereichen des Rohrquerschnitts unterschiedlich zu sein. Hochfrequente Schwankungen der Geschwindigkeit in Strömungsrichtung wurden zuerst im Kernbereich der Strömung gefunden. Messungen des Druckverlusts zeigen einen deutlichen Knick in der Korrelation bei Re ≈ 8000 und deuten damit auf eine weitere kritische Reynolds-Zahl, welche die Schwelle zur Turbulenz mit breitbandigem Frequensprektrum über den gesamten Rohrquerschnitt darstellt.

Die vorliegenden Ergebnisse erweisen sich als kompatibel mit den – im Vergleich zu geraden Rohren sehr wenigen – publizierten experimentellen Ergebnissen in Bezug auf die allgemeinen

Merkmale des laminar-turbulenten Übergangsszenarios in gekrümmten Rohren. Ein Teil des Vergleichs basiert jedoch auf Vermutungen, da ein quantitativer Vergleich mit früheren Ergebnissen oft nicht möglich war. Alle Ergebnisse der vorliegenden Arbeit stützen die Sichtweise, dass der verwendete experimentelle Aufbau mit toroidaler Geometrie ein geeignetes Modell für gekrümmte Rohre im Allgemeinen ist und zu den gleichen Ergebnissen wie in offenen Systemen führt. Eine entscheidende Ursache für Abweichungen von einer absolut stetigen, ungestörten Grundströmung ist die die Strömung antreibende Kugel, welche eine konstante Störung der Strömung im Bereich der Kugel bewirkt. Darüber hinaus könnte die 2π–Periodizität der Geometrie eine wichtige Rolle bei der Auswahl spezifischer Wellenlängen und Wellengeschwindigkeiten der kohärenten Strukturen spielen.

Contents

Abstract

The central theme of the present thesis is the process of transition to turbulence in a torus, representing a model for curved pipes. Transition to turbulence in curved pipes is considerably different compared to transition in straight pipes, since the onset of turbulence is significantly delayed to higher Reynolds numbers even for small pipe curvature. Moreover, the whole transition scenario is substantially modified. A sequence of transitions instead of a sudden leap was found, leading from a steady basic flow trough periodic and quasi-periodic states to a chaotic behavior, exhibiting analogies with the canonical Taylor–Couette flow and accordance with the Ruelle-Takens-Newhouse-Scenario.

The aim of the work was to accurately investigate and measure transition to turbulence in curved pipe flow experimentally. Special attention was paid to the detection and investigation of traveling waves and coherent structures emerging with the first instability. The main objective was to reveal the physics and key points of the primary traveling wave instability and the subsequent development at higher Reynolds numbers in a curved pipe.

To that end a novel experiment was designed, set up, put into operation and successfully tested, which realizes a precisely adjustable flow in a toroidal pipe. The facility was designed and optimized to investigate curved pipe flow by state-of-the-art nonintrusive measurement techniques at arbitrary Reynolds numbers, i.e. at different flow rates. The novel facility consisted of two disks of plexiglas, where a concentric notch of (half-) circular cross sections had been machined out. When placed on one another mirror-symmetrically the two disks form a closed toroidal cavity, i.e. the actual curved tube. The flow was driven by a rolling sphere that is moved from outside the closed toroidal cavity using a magnet which is mounted on a rotating boom. The ratio of the coiling to the tube diameter was 20.26.

Visual observations, laser-Doppler velocimetry, high-speed stereoscopic particle image velocimetry (S-PIV) and pressure drop measurements have been used to investigate and capture the appearance and development of the transitional flow. Using S-PIV it was possible to reconstruct all three components of the velocity vectors in the measurement plane covering the entire cross-section of the tube. As hydrodynamic instability is a dynamic, time variant phenomenon, the time-resolved S-PIV measurements yielded a comprehensive picture of the whole flow field during transition to turbulence.

For a Reynolds number of 4080 a supercritical transition from the steady basic flow to a laminar flow which is periodically modulated in the streamwise (toroidal) direction was found. The emerging pattern is almost stationary in a frame of reference moving with the actuator, exhibiting a wave celerity slightly above ($\sim 12\%$) the mean bulk velocity of the flow depending on the Reynolds number. The characteristic wavelength λ was found to be approx. $2d$ or $11.25°$ for Re < 4350 and observed to start varying between 2 to $4d$ for Re $\gtrsim 4350$. Right above the critical Reynolds number the amplitude of the streamwise modulation is very small. With increasing Reynolds number, the modulation amplitude of the streamwise velocity grows and the associated flow pattern becomes more distinct. The intensity of the streamwise velocity fluctuations is of the order of up to 15% of the bulk velocity. The modulation of the streamwise

velocity field is also distinctly reflected in the streamwise pressure drop. Mean velocity profiles, especially for increasing Reynolds number, and investigations of the instantaneous flow field at the first instability are presented in the work. The large scale velocity fluctuations are described and the frequency spectra are analyzed.

The single dominant frequency (f_1), which could be regarded as the 'fingerprint' of the first instability, was found to be preserved to higher Reynolds numbers. At a second critical Reynolds number of ≈ 4400 a transition to a flow with two (or more) incommensurate frequencies f_1 and f_2 was found. The two frequencies seem to be irrationally related, i.e. the flow to be quasi-periodic. The exact value of the second frequency f_2 has not been identified though narrowed down to a value close to the one of f_1, the first dominant frequency. The presumably quasi-periodic state exists up to Reynolds numbers > 6000, still being dominated by a single frequency (f_1). Transition at higher Reynolds numbers to turbulence proper was observed to be considerably different in different areas of the cross section, as high frequency fluctuations of the streamwise velocity were found first in the high speed core region of the flow. Friction factor correlations based on the measured pressure drop show a soft kink at Re ≈ 8000, indicating a critical Reynolds number for high-frequency turbulent properties all over the cross section of the pipe and marking the threshold to explicit broadband turbulence.

The present results were found fully compatible with the few published experimental and computational results concerning the general features of transition in curved and helical pipes and related scenarios. Since the data published are sparse a good part of the comparison is based on conjectures. Quantitative comparisons with previous results are mostly not possible. The consistent findings, however, strongly support and promote the view that the present experimental setup and the toroidal geometry used is an appropriate model for curved pipe flows in general, yielding the same results as in open systems. A major source of deviation from a pure toroidal basic flow is the actuator (sphere), representing constant perturbation in the vicinity of the sphere triggering transition. Furthermore, the 2π–periodicity of the setup and the length of the actuator might play an important role in selecting the specific wavelengths and wave speeds of the coherent structures.

Acknowledgements

Nomenclature

Symbol	Units	Definition(s)
a	m	pipe cross section radius
d	m	$(= 2a)$ pipe cross section diameter
R	m	radius of coiling, radius of torus, radius of curvature
D	m	$(= 2R)$ diameter of torus
δ		$= a/R$, radius ratio, curvature ratio
A_r		$= R/a$, aspect ratio
A	m^2	cross-sectional area
r		distance from the center of the cross section of the pipe
α		poloidal angle in the cross section
φ		azimuthal or toroidal angle, angular distance between cross sections
$u = u_r$		(instantaneous) velocity component in the radial direction
$v = u_\alpha$		(instantaneous) velocity component in the tangential direction
$w = u_\varphi$		(instantaneous) velocity component in the streamwise direction
$\bar{u} = \bar{u}_r$		mean (time averaged) velocity component in the radial direction
$\bar{v} = \bar{u}_\alpha$		mean (time averaged) velocity component in the tangential direction
$\bar{w} = \bar{u}_\varphi$		mean (time averaged) velocity component in the streamwise direction
U	m/s	mean/bulk streamwise velocity (averaged over the entire cross section)
T	C°	temperature
t	s	time
p	N/m^2	pressure
Δp	N/m^2	pressure drop
ρ	kg/m^3	density
η	Pa·s	dynamic viscosity
ν	m^2/s	kinematic viscosity
Ω	s^{-1}	$= \Delta\varphi/\Delta t$ angular velocity of actuator
λ		wavelength
f	Hz	frequency
$\hat{f}$		$\hat{f} = fd/U$, normalized frequency
δx		deviation of x
Re		$= Ud/\nu$, Reynolds number
De		$= \mathrm{Re}\sqrt{\delta}$, Dean number

In some cases subscripts are used. The respective meaning is explained in the text.

Abbreviations

LDV   Laser Doppler Velocimetry

(S)PIV   (Stereoscopic) Particle Image Velocimetry

2D   two dimensional

3D   three dimensional

Denotations

Mean $\bar{u} = \sum_{i=1}^{N} \frac{u_i}{N}$, Mean value of u

RMS $\sigma = \sqrt{\sum_{i=1}^{N} \frac{(u_i - \bar{u})^2}{N}}$, Root Mean Square of u

         where N number of data points in a set

Declaration

Revised parts of the present thesis shall be published in journals. Some of the results were already presented at conferences and published in the conference proceedings, which are not separately quoted in this work. Furthermore, some (also revised) passages of the present text have already been used for proposals to the Austrian Science Fund. The published work (until November 21, 2012) and contributions to conference proceedings are listed below.

J. Kühnen, M. Holzner, B. Hof, H. Kuhlmann, Transition to turbulence in a torus, 15th ERCOFTAC Alpe Danube Adria Pilot-Center Meeting, Vienna, Austria, April 20th, 2012

J. Kühnen, M. Holzner, B. Hof, H. Kuhlmann, Time-resolved 3D-PIV measurements of traveling waves in a torus, 16th Int. Symp. on Applications of Laser Techniques to Fluid Mechanics, Lisbon, Portugal, 09-12 July, 2012

J. Kühnen, M. Holzner, B. Hof, H. Kuhlmann, Experimental investigation of transition to turbulence in a torus, 9th European Fluid Mechanics Conference, Rome, Italy, 9-13 September, 2012

Note

Supporting material to the present work can be found on the enclosed CD which contains the movie files quoted in the text, the control software of the torus, further design drawings and other documents.

1 Preamble

Flows in pipes are of fundamental scientific interest and of great technical importance. Two characteristic kinds of flows are commonly known to exist: the laminar and the turbulent regime. Or, in other words, on one hand the fully deterministic regime of highly ordered motion, where the fluid is moving in straight parallel 'layers' without cross currents perpendicular to the direction of the flow - and on the other hand the regime of chaotic property changes and fluid motions on various length scales. Even though these chaotic fluid motions are theoretically deterministic, in practise the experimenter deals with seemingly stochastic fluid motion due to the overall chaotic behavior of the flow, molecular diffusion and the non-reproducibility of the (exact) initial conditions (see e.g. Mullin 1993). Furthermore, the classification laminar or turbulent is physically not very precise. To keep things simple, in the present work *turbulence* just denotes a general state of chaotic fluid motion where high frequency flow fluctuations on various length scales, being *practically* random, are superimposed on the mean basic flow. As the word *laminar* is also somehow misleading by definition for curved pipes (see 2.3), laminar will just denote the steady basic flow state, where no fluctuations can be found.

Usually, the domain of *transition* from clearly laminar to definitely turbulent flow is not perceived as 'autonomous' regime. Certain aspects of flows in the transitional regime ('between' laminar and turbulent state), such as regular pattern formation and well-ordered coherent structures, i.e. flow structures which separate dynamically distinct regions within the flow, render the transitional regime unique though.

What has become entitled as *the turbulence problem* comprises two parts: the onset of turbulence, which is conceived as an instability of laminar flow; and fully developed turbulence, for which both empirical and statistical theories of turbulence have been developed. Up until the present time turbulence research has been inter- and transdisciplinary, attracting scientists and engineers from a variety of specialties and with diverse scientific and technological orientations (Eckert 2008). Only the first part, the onset of turbulence, is in the general focus of the present work.

Shear flows in general experience a more or less sudden transition from laminar to turbulent motion as the velocity increases, with a rather narrow domain of transitional flow. Amongst other canonical flows such as Plane–Couette flow (between two flat planes) or Taylor–Couette flow (between two rotating cylinders), the transition to turbulence in straight pipe flow has attracted much research effort since the pioneering work of Reynolds (1883). From a theoretical point of view the situation is paradox, since transition occurs despite the linear stability of the Hagen–Poiseuille flow (laminar flow in a straight cylindrical pipe). Progress in the understanding of the transition from laminar to turbulent flow in pipes has been slow since Reynolds' seminal investigations more than a century ago. During the last decade, however, a significant step forward has been made by combining concepts of nonlinear dynamical systems with numerical simulations. Major advances in measurement technology and scientific computing have led to deep insights into previously inaccessible details of pipe-turbulence transition. In particular, the transition in *straight cylindrical* pipes has thoroughly been investigated and is well documented.

Yet, the details of the transition process and why pipe flow becomes turbulent at all remain under discussion. Issues of the current debate are the question of whether turbulence in pipes is generally transient in nature or not, the exact scaling with Reynolds number of the characteristic lifetime τ of the turbulent state, the role of traveling waves in the transition process, and many more (Eckhardt et al. 2007).

It is well known that even in *gently curved* pipes the transition to turbulence is considerably affected by curvature and different from that in straight pipes. The major difference arises from the secondary motion of the flow induced by the curvature of the pipe. Compared to straight pipe-flow transition there has been much less research on transition to turbulence in curved and helical pipes, even though the latter are not of lesser importance: all practical piping systems, be it in the field of engineering and technology or in nature (e.g. blood flow), are more or less curved.

As pointed out by Piazza & Ciofalo (2011), a *toroidal* pipe flow configuration is the common asymptotic limit of two distinct classes of curved pipe flow configurations, both constituting important fluid mechanical domains: the flow in curved ducts and the flow in helical ducts with small pitch, both under the assumption of fully developed flow. Thus, curved and helical pipes can be studied as a toroidal pipe. This works well in theory, i.e. for analytical solutions and numerical calculations, but unlike in open configurations where a fluid can be e.g. pumped through the duct, the achievement of a constant flow rate in a closed torus has depicted a seemingly impossible obstacle up to date. At least to the authors knowledge so far no study has tried nor achieved to realize a *steady* flow in a torus for experimental investigations.

The rather simple mechanism used to accomplish precisely adjustable constant flow in a torus for the investigation presented here was by placing an adequate actuator, realized as an iron sphere or a custom-made plunger, into a torus made of plexiglas. The actuator was then controlled and moved from outside the torus via a magnet which was mounted on a rotating boom. This yielded a novel experimental facility perfectly suited for visual observations as well as LDV and SPIV (see section 3.2) measurements of the flow in a toroidal pipe. The setup enabled acquisition of all three components of the velocity vectors in a measurement plane covering the entire cross-section of the pipe to capture the appearance and development of transitional flow. Hence it provided an insight into the fully space and time resolved structure of the flow.

The present work is intended to contribute to the understanding of curved pipe-flow transition in the light of the advances and insights made for straight pipes within the last years, focusing on the recently detected traveling waves in transitional flow in straight pipes (Hof et al. 2004). The main objective is to reveal the physics of the primary traveling wave instability in a torus which serves as a general model for curved pipes.

The next section, after a brief introduction to the concept of hydrodynamic stability, will highlight previous work and the major advances on transition to turbulence in straight pipes. Subsequently the main work and findings on the general character of the flow and especially the transition to turbulence in curved pipes will be summarized. A comparison between transition in straight and curved pipes and some of the resulting questions are then discussed in the section thereafter. To confine the subject, only steady, incompressible flows in circular pipes of uniform

(or zero) curvature are considered in this work.

After providing an overview of the theoretical background the methods and measurement techniques applied will be discussed, followed by an in-depth consideration and presentation of the experimental facility and setup. The results will be provided in the chapter thereafter, followed by a discussion and conclusions.

2 Theoretical Background

In the following chapter a short introduction to hydrodynamic stability theory, including a brief excursion on the branching behavior of solutions and references for further reading, is provided. As curved pipes are, at least in some respects, very closely related to straight pipes, a short section is thereafter dedicated to transition to turbulence in straight pipes. Subsequently an in-depth consideration of curved pipes is presenting a literature review, basic facts and reference values concerning velocity and pressure distribution, friction factor and pressure loss, the critical Reynolds number for transition to take place and development lengths. Most importantly, stability and bifurcation scenarios are reviewed. A short comparison between the straight pipe and curved pipe scenario will close the chapter.

2.1 A brief introduction to hydrodynamic (in)stability

Natural systems in general are exposed to various kinds of disturbances and perturbations. These disturbances may lead to a change of the state of the system. If the system retains its state even under an imposed disturbance it is called stable, if the system changes its state it is called unstable. An unstable system can pass through an instability to a new stable state. Whether the state of the system changes or not depends on the system and the strength of the disturbance.

Hydrodynamic stability as a specific field and subject of fluid mechanics deals with the question of the general flow structure within a fluid which is realized under given conditions and perturbations. The definition of 'stability' is always related to a reference state, called the basic flow or base flow, e.g. $\boldsymbol{u}_0$. To put it simply, if a small perturbation $\delta\boldsymbol{u}$ added to the base flow grows within time the flow is unstable, while if $\delta\boldsymbol{u}$ decays it is called stable.

Such a basic flow is usually characterized through high symmetry, i.e. the underlying equations and boundary conditions are invariant under certain symmetry operations (Kuhlmann 2010). An important aspect of hydrodynamic stability is the change in the symmetry properties of the flow when the driving force of the flow is increased. In most cases, the symmetry of the flow is decreased when the driving force increases, i.e. the basic state becomes unstable. After obtaining a new equilibrium, i.e. a stable state again, the resulting flow structures can be both stationary and time dependent, often called modes.

The driving force is normally represented by a single parameter, e.g. the Reynolds number (see sec. 2.2). The value of the parameter where the symmetry is broken is called *critical* value. This change in flow regime can be described by a bifurcation diagram (bifurcation denominates a branching of the solutions). By observing the flow characteristics (i.e. the solutions of the governing Navier-Stokes equations or the new equilibrium states) either numerically or in an experiment, the critical points of the system for an increasing control parameter can be found. The number of solutions or their symmetry changes at the critical bifurcation-points can be determined. Numerically, both stable and unstable branches of solutions can be detected. Experimentally, however, only stable solutions are realized. They can be measured and represented by, e.g., a velocity at a fixed point in space as a function of the driving force.

The branching or bifurcating of solutions is a direct consequence of the nonlinearity of the Navier-Stokes equations. Over the years many different transition scenarios were found and described. A distinction between the various scenarios known can be made by their branching behavior. Saddle-node bifurcations, transcritical bifurcations, pitchfork bifurcations and Hopf bifurcations are the most important ones. Put simply, Hopf bifurcations mean that a steady base flow becomes oscillatory. They can be either supercritical or subcritical. Supercritical denotes a bifurcation where the bifurcating flow, after a decrease of the Reynolds number, returns back to the basic state at the same critical Reynolds number as during an increase of the Reynolds number. Subcritical denotes a bifurcation tainted with hysteresis, i.e. where the critical Reynolds number is below the critical Reynolds number of the origin.

Transition to turbulence by a series of bifurcations, where the caused hydrodynamic instabilities are, contrary to their fallacious name, stable states with a successive breaking of symmetries, is only one possible scenario. Scenarios where the intermediate steps on the way to turbulence are stable stages are standard but not a rule. Straight pipe flow is probably the most famous exceptional case, as there is no *stable* solution known except for the Hagen–Poiseuille flow. It is for this reason that the scenario in straight pipe flow has been described as bypass transition, i.e. a direct crossover to turbulence. Transition in *curved* pipes, however, is known to go through a series of stable states though.

The problem of transition to turbulence in shear flows is still not fully understood. Turbulence occurs on a complicated interaction of absorption, redistribution of energy between different degrees of freedom of the system and the production of energy (Kuhlmann 2010). This interaction is essential for the development of turbulence. For the emergence of chaotic flow three different 'generic' scenarios have been suggested to describe the transition from laminar to turbulent flow, called *Feigenbaum-scenario*, *Ruelle-Takens-Newhouse-scenario* and *Pomeau-Manneville-scenario* (*intermittency*) (Eckmann 1981, Kuhlmann 2010). Namely the Ruelle-Takens-Newhouse-scenario is interesting for the present work, as the results (see chapter 5) seem to support the respective scenario via incommensurate frequencies.

Newhouse et al. (1978) argued that, as a function of an external parameter, the route to chaos in a fluid flow is a transition sequence leading from stationary (S) to single periodic (P), double periodic (QP$_2$), triple periodic (QP$_3$) and, possibly, quadruply periodic (QP$_4$) motions, before the flow becomes chaotic (C). However, the quasi-periodic motions with 3 or 4 incommensurate frequencies were shown to be unstable with respect to small perturbations and may, hence, not be observed at all (van Heijst et al. 2004). If a system undergoes three Hopf bifurcations, starting from a stationary solution, as a parameter is varied, then it is likely that the system possesses a strange attractor with sensitivity to initial conditions after the third bifurcation. The power spectrum of such a system will exhibit one, then two, and possibly three independent basic frequencies. When the third frequency is about to appear, simultaneously some broad-band noise will appear if there is a strange attractor (Eckmann 1981).

Since the early works of von Helmholtz (1868), Kelvin (1871), Rayleigh (1879, 1880), Bénard (1900), Couette (1890), Taylor (1923) and – especially important for pipe flow – Reynolds (1883), several 'standard' systems have been established for studies of the transition behavior,

all characterized by a rather simple geometry. These include, among others, the Taylor-Couette and Rayleigh-Bénard system and the lid driven cavity. For more details on these standard systems and further reading on hydrodynamic stability in general see e.g. Chandrasekhar (1961), Benjamin (1978a,b), Drazin & Reid (1981), Drazin (2002), Schmid & Henningson (2001) and Kuhlmann (2010). See especially Iooss & Joseph (1997) for elementary stability and bifurcation theory and Eckert (2010) for an interesting consideration of historical aspects.

The topic dealt with in this work falls into the field of hydrodynamic stability, as transition to turbulence in a curved pipe is the consequence and result of a laminar base flow becoming unstable to (small) perturbations, causing a change to a different (stable) state. For the clarification of the process of transition to turbulence the sequence of different bifurcations and their branching behavior is an important concept hence.

2.1.1 Branching behavior

Since the topic is very broad and extensive, only a few cases of bifurcations which actually appeared in the experimental investigations (see sec. 5) are presented here. To illustrate the mechanism of a bifurcating system the model of a one-dimensional motion of a point without mass but subject to friction in the potential

$$\Phi(x) = -\frac{\mu}{2}x^2 + \frac{x^4}{4} \tag{1}$$

with the equation of motion

$$\dot{x} = -\nabla\Phi \tag{2}$$

is considered. μ characterizes the so-called control parameter, which corresponds to the Reynolds number in the present experiments. For $\mu < 0$ (a in figure 1) the flow is stable to all disturbances. Disturbances decay monotonously and exponentially with time. The equilibrium state $x_1 = 0$ (●) is called a fixed point.

For $\mu > 0$ (b in figure 1), however, two different stable states exist, while the originally stable state $x_1 = 0$ has become unstable, as (1) has three stationary solutions $x_1 = 0$ (unstable; ○) and $x_{2,3} = \pm\sqrt{\mu}$ (●; stable). Such a scenario is called pitchfork bifurcation and the branching is called super-critical, as the new flow structure, after it is fully developed, when subject to a quasi-static (i.e. infinitesimally slowly) decrease of the Reynolds number returns to the initial equilibrium state at the same critical Reynolds number as when Re was increased.

If the critical Reynolds number is below the Reynolds number which was critical for a quasi-static increase of the Reynolds number, then the branch is considered to be afflicted with hysteresis and called subcritical. This behavior can be described with

$$\Phi(x) = -\frac{\mu}{2}x^2 - \frac{x^4}{4}, \tag{3}$$

as shown in c) and d) of fig. 1.

In experimental studies it can be observed that the response of a continuously developing branch to a disturbance is considerably influenced by so-called critical-slowing-down, occuring in the immediate vicinity of the critical point. Close to the critical point the time required by
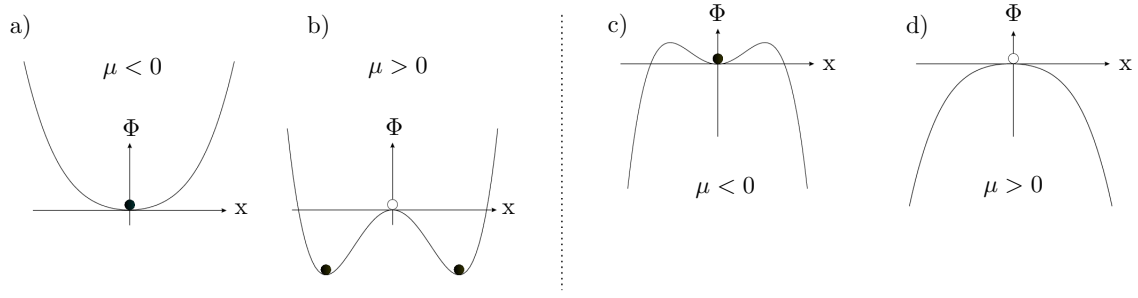
Figure 1: Model of a massless point in a potential. Points indicated with • denote stable, those indicated with ○ unstable states.

the dynamic system to reach a new equilibrium state, after changing the control parameter μ, is very high and tends to infinity at exactly the critical point. For the mechanical model of equation 2 this means, if $x(t=0) = x_0$ does not lie at the fixed point of the basic system and the difference is very small, the (linearized) solution of the equation of motion can be expressed by

$$x(t) \approx x_0 e^{\mu t} \ . \tag{4}$$

For $\mu \to \mu_c = 0$ the time required to change the deviation from the basic solution diverges with $1/\mu$ (see fig. 2).

To reduce the effect of critical slowing down to an acceptable level, the time after changes of the control parameter in the vicinity of its critical value (for example in determining the critical Reynolds number) has to be long enough (see sec. 3.1).
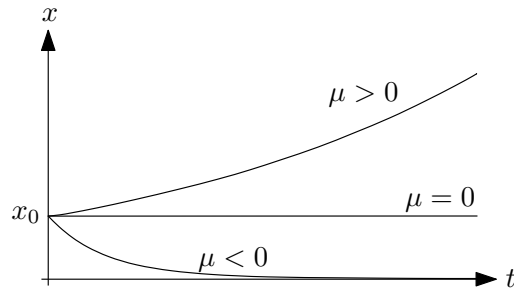
Figure 2: Critical-slowing-down in the vicinity of $\mu \to \mu_c = 0$.

2.2 Review of the transition scenario in straight circular pipes

Transition to turbulence in straight pipes is one of the oldest and most fundamental problems of fluid mechanics. In straight pipes the fully developed laminar flow exhibits the well known parabolic Hagen–Poiseuille profile for the axial velocity with the maximum at the pipe axis, without any radial or circumferential velocity components. As single governing parameter to describe the ratio of inertial to viscous forces, guaranteeing dynamic similitude between different pipe flow configurations, the dimensionless Reynolds number

$$\mathrm{Re} = \frac{Ud}{\nu} \tag{5}$$

is used. Re is based on the mean velocity U of the flow, the pipe diameter d and the kinematic viscosity ν. For Reynolds numbers $\lesssim 2040$ (Avila et al. 2011) the flow in a straight pipe can be expected to be laminar, while above this value it is *usually* found to be turbulent.

When the Reynolds number of an originally laminar flow is increased and perturbations of the flow exceed a minimum threshold, transition to turbulence occurs despite the linear stability of the Hagen–Poiseuille flow. The linear transient growth of initially small perturbations (Trefethen et al. 1993, Schmid & Henningson 1994), the establishment of a self-sustained nonlinear process (Waleffe 1997), and the organization of the flow around exact solutions of the Navier- Stokes equations (Faisst & Eckhardt 2003, Wedin & Kerswell 2004) have been suggested as transition scenarios.

Most recent of origin is the consideration of pipe flow in terms of a dynamical system. In such an approach the laminar flow corresponds to a fixed point in phase space. The basin of attraction of this fixed point is a complicated manifold and it shrinks as the Reynolds number increases. It has been shown that the dynamics in phase space of the turbulent state depends on the existence of periodic orbits, representing traveling waves, which have first been found in plane Couette flow (see Waleffe 1998, 2001, 2003) and, thereafter, in pipe flow (Faisst & Eckhardt 2003, Wedin & Kerswell 2004, Hof et al. 2004). For reviews see Kerswell (2005) and Eckhardt et al. (2007). On an increase of the Reynolds number all periodic orbits (waves) are created by saddle-node bifurcations and they are all unstable.

The unstable states are numerically found to exist down to flow rates significantly below those at which transition is observed to occur (Kerswell 2005, Pringle & Kerswell 2007). Stability analyses have shown that the unstable solutions have one (or only very few) unstable eigenvalues of the linear-stability problem. As a result the system may approach (but not reach) the unstable orbit from the many stable directions in phase space, stay close to it for a significant amount of time, and finally be rejected from it, eventually escaping to the laminar state (Faisst & Eckhardt 2004). Such a behavior is commonly called a chaotic saddle. Based on these observations several attempts have been made to construct minimal models of turbulence which reflect many features of the full system (Waleffe 1997, Moehlis et al. 2004). One of these features is the observed intermittency (Eckhardt et al. 2002), where turbulent spots occur in the form of localized patches that are surrounded by laminar flow.

The unstable solutions share many features with the coherent structures observed in experiments. These structures consist of three elements: stream-wise vortices (rolls), streaks, and
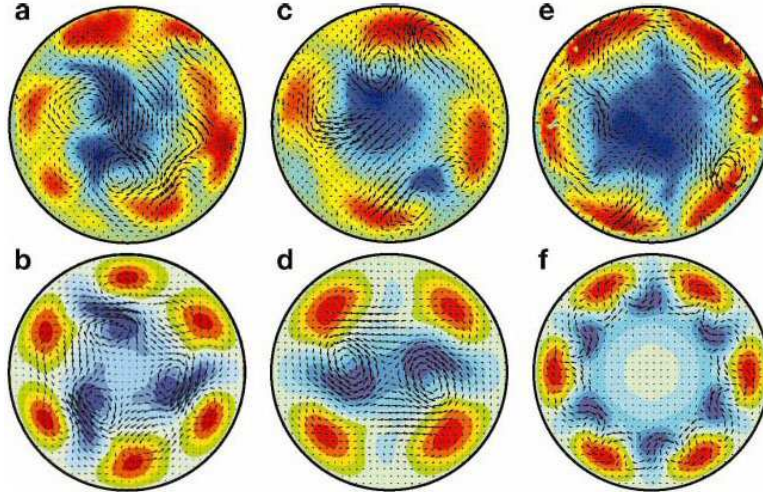
Figure 3: Velocity fields measured by PIV by (Hof et al. 2004) (top row) and corresponding numerical solutions (bottom row), showing cross sections of a traveling wave at different positions along the wave. The frames are at times 0, 1/8, 2/8, and 3/8 of a period and at a fixed position along the axis. The velocity components in the plane are indicated by arrows. For the axial component the difference to a parabolic profile with the same mean speed is color coded. Regions where the fluid flows faster are shown in red and correspond to high-speed streaks. Similarly, regions where the speed is lower are shown in blue and correspond to low-speed streaks. The figure is taken from Eckhardt et al. (2007).

waves (streak instability). They act together such as to reinforce each other symbiotically against viscous decay (Hamilton et al. 1995, Waleffe 1997, Duggleby et al. 2007). An important idea is that these coherent structures are related to the exact unstable solutions. Therefore, the term *exact coherent structures* has been coined by Waleffe (1998, 2001, 2003). They are supposed to act as organizing centers for the turbulence quasi-cycle found by Hamilton et al. (1995). However, the relation of the coherent structures to the exact solutions is not yet fully explored.

The experiments of Reynolds (1883) and later those of Wygnanski & Champagne (1973), Wygnanski et al. (1975), Bandyopadhyay (1986), and others revealed that the development of the flow depends solely on the Reynolds number. While no *sustained* transition is possible to find for Re < 1760 (i.e. all perturbations immediately decay), localized turbulent states (*slugs* and *puffs*) can be generated by suitable localized perturbations (characterized by strength and azimuthal symmetry) at Re > 1760.

However, theory does not yet provide any satisfactory explanation for the localized states. The threshold amplitude of the initial perturbation that is required to establish a sustained turbulent state was found to be a decreasing function of the Reynolds number (Darbyshire & Mullin 1995). Hof et al. (2003) made this result more precise by establishing that the threshold amplitude for transition to occur scales with Re^{-1} in the range $2000 < Re < 20000$. These results support the theoretical picture of a decreasing basin of attraction of the laminar fixed point. The phase-space dynamics described above may explain some of the experimental observations such as, e.g., the fractal boundary of the basin of attraction of the Hagen–Poiseuille fixed point.

Figure 4: Numerical simulation of a traveling wave at Re = 2215 by Mellibovsky & Eckhardt (2011). Left: cross-sectional axial velocity contours. In-plane velocity vectors are also displayed. Right: axial vorticity isosurfaces. Fluid flows rightwards. Blue (dark gray) for negative, yellow (light) for positive.
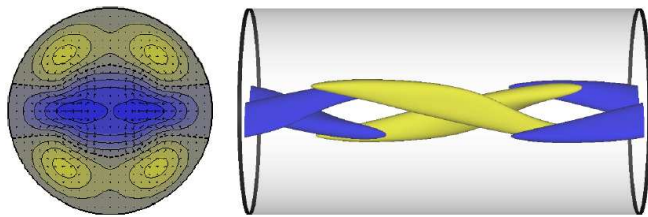
Experimental results on transitional pipe flow have been reviewed by Mullin (2011). Peixinho & Mullin (2006), Mullin & Peixinho (2006), and Faisst & Eckhardt (2004) found that the lifetime of an initial perturbation scales like $\tau \sim (\mathrm{Re} - \mathrm{Re}_c)$, where Re_c depends on the perturbation amplitude. Generally, the lifetime of turbulence has been observed to increase rapidly with Reynolds number but there is currently no accord on the exact scaling behavior. In particular, it is not clear whether a critical point exists where turbulence becomes sustained or if it remains transient. Accurate measurements of Hof et al. (2008) and Kuik et al. (2010) revealed for a wider measurement range, however, that the turbulent state remains transient with a lifetime that grows super-exponentially with Re. To determine the critical point for the onset of sustained turbulence, Avila et al. (2011) compared the time scale for turbulence to spread with the time scale for turbulence to decay, i.e. the mean lifetime of a puff before decaying or splitting. They found that both curves correspond to superexponential scaling with Re and have a crossover at $\mathrm{Re} = 2040 \pm 10$, determining the transition between transient and sustained turbulence in pipe flow in the thermodynamic limit.

Concerning the structure of the turbulent flow Eliahou et al. (1998) have shown experimentally that stream-wise rolls, generated by suitable initial perturbations, become unstable to azimuthal perturbations. Their results support the model of a self-sustained process proposed by Waleffe (1997) (see also Nikitin 1994, Zikanov 1996). Further support of the theory is due to Hof et al. (2004) and e.g. Mellibovsky & Eckhardt (2011, 2012) by showing that the pipe flow exhibits three-dimensional structures very similar to the exact unstable solutions for a substantial period of time (fig. 3 and 4).

This observation is enabled by the fact that the dynamical system typically stays close to an unstable orbit discussed above for a significant amount of time if the Reynolds number is not too high.

2.3 Review of the flow in curved circular pipes

The laminar flow in even weakly curved pipes differs considerably from the one in straight pipes. In curved pipes an imbalance between the cross-stream pressure gradient and the centrifugal force induces a secondary motion. Typically, the location of the maximum streamwise velocity is shifted toward the outer wall and two counter-rotating so-called Dean vortices (Dean 1927, 1928) are created due to the secondary flow. At low Reynolds numbers the Dean vortices are steady and placed symmetrically with respect to the plane of symmetry. The flow at low Reynolds numbers is commonly called laminar. It must be noted, however, that *laminar* in the sense of "fluid flows in parallel layers without lateral mixing" is already inconsistent and somehow misleading by definition for curved pipe flow due to the Dean vortex pattern.

Amongst others, Williams et al. (1902), Eustice (1910, 1911) and in particular Taylor (1929), White (1929) and Adler (1934) already observed the fundamental and significant characteristics of curved pipe flow. First of all they noticed in their experiments that the location of the maximum axial velocity is shifted to the outer wall of the pipe and that a secondary flow evolves due to curvature. More surprising, and still not well understood, they found that the flow in curved pipes is laminar up to substantially higher Reynolds numbers than in straight pipes, exceeding the critical Reynolds number for straight pipes (≈ 2040, subject to the remarks in sec. 2.2) by a factor of two or more. They further noticed that transition to turbulence is not as abrupt as in a straight pipe but occurs gradually, without any remarkable jumps or discontinuities in the parametrical correlations. And they also witnessed that a dye streak introduced into the flow starts to oscillate periodically for Re $\gtrsim$ 5000, i.e. in the transitional regime, providing a first hint at a hydrodynamic instability.

In numerical simulations and theoretical analyses curved pipes are usually modeled in a toroidal coordinate system. Torsion in helically coiled pipes is taken into account by using helical coordinates (see e.g. Germano 1982, 1989, Liu & Masliyah 1993, Hüttl et al. 1999). In experiments helically coiled pipes with negligible torsion (small pitch, i.e. a small increase of height per turn) have always been an obvious first choice for the investigation of curved pipe flow. Due to the similar characteristics of the flow in curved and helically coiled pipes they are frequently treated simultaneously. Helically coiled pipes, representing a particular class of curved pipes, are of great importance in practical engineering applications such as heat exchangers and chemical reactors. They have received much attention concerning their augmented heat transfer characteristics due to the secondary flow. Since the focus of this work is on the transition scenario and its flow characteristics the vast area of heat transfer enhancement (for a recent review, see Naphon & Wongwises 2006) is not considered. As the experimental setup has zero pitch, the influence of torsion is also not considered. It should be noted, however, that a strong torsion (large pitch) in curved pipe flow may have an effect which is contrary to that of curvature (Yamamoto et al. 1994, 1995, 2002).

Dean (1927, 1928), using analytical solutions of simplified Navier-Stokes equations for flow in a coiled pipe of small curvature, was the first to show that only two parameters, namely the ratio $\delta = a/R$ of the radius of the pipe a to the radius of coiling R, mostly called radius ratio

CONTOURS OF CONST. AXIAL VELOCITY
------ SECONDARY STREAMLINES
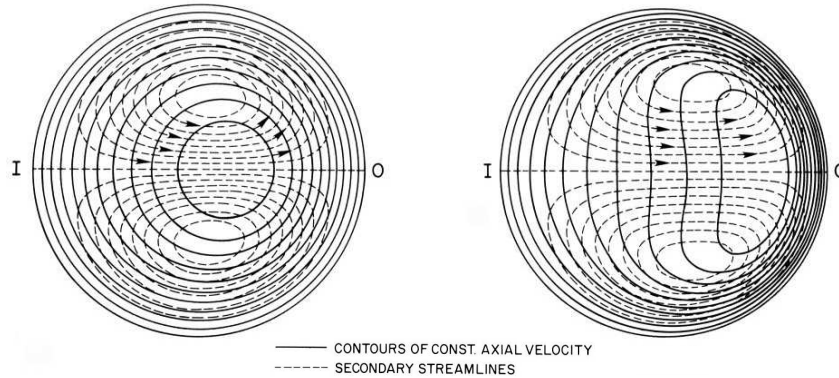
Figure 5: Numerical computations of secondary streamlines and axial-velocity contours at low (left, De = 96) and intermediate (right, De = 606) Dean numbers (McConalogue & Srivastava 1968). I denotes inner bend, O outer bend. The location of maximum axial velocity is moving outward with increasing Dean number, while the secondary streamlines continue to show a vortex-like appearance. The figure is taken from Berger et al. (1983).

or curvature ratio, and the later called Dean number

$$\mathrm{De} = \mathrm{Re}\sqrt{\delta} \tag{6}$$

characterize the flow in a curved pipe. The Dean number plays the role of the Reynolds number (see eq. 5) as in straight pipes, while δ is a more detailed measure of the effect of geometry and the extent to which the centrifugal force varies on the cross section. Thus δ affects the balance of inertia, viscous, and centrifugal forces (Berger et al. 1983).

Comprehensive reviews of the numerous theoretical, numerical and experimental works on laminar flow in curved pipes until the early 1980s are given by Ward-Smith (1980) and Berger et al. (1983), with some additional information in the brief review of Ito (1987). The theoretical works mainly dealt with the development and structure of primary and secondary flow in curved pipes, in order to confirm, extend and refine the early findings of Dean and co-evals by computing finite-difference solutions of the Navier-Stokes equations. As one example, the early numerical computations of secondary streamlines and axial-velocity contours at low and intermediate Dean numbers are shown in fig. 5. The experimental works put the primary emphasis on measurements of the friction factor (see 2.3.3), since the friction factor is of fundamental importance for industrial applications. Visual inspections by dye-injection (Eustice 1910, 1911) and more quantitative measurements with Pitot-tubes (Adler 1934) and later on measurements with Laser-Doppler Velocimetry (Agrawal et al. 1978) were conducted to explore velocity distributions (see 2.3.2), entry flows and development lengths (see 2.3.5). Comparison with theory and numerical computation yielded consistent results.

A characteristic feature of transition to turbulence in curved pipe flow, which was first adumbrated by Taylor (1929), later confirmed by Sreenivasan & Strykowski (1983) and Webster & Humphrey (1993, 1997) and very recently brought up again by Piazza & Ciofalo (2011), is the existence of a sequence of bifurcations to turbulence via a traveling-wave instability of the Dean flow (see 2.3.6). This known but not yet fully explored traveling-wave instability
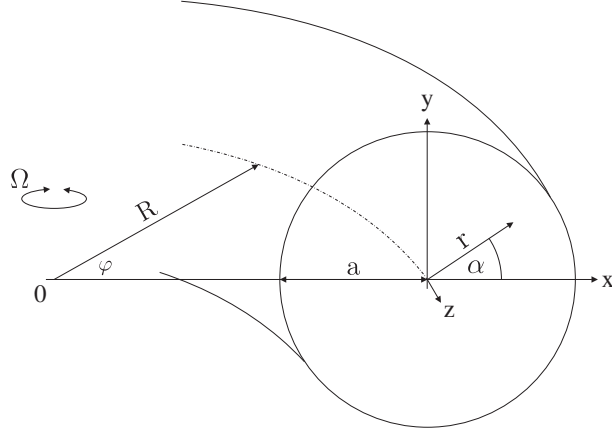
Figure 6: A pipe with radius a coiled in a circle with radius R shown in the toroidal (r, α, φ) coordinates system as used within this work. Also shown is the cartesian (x, y, z) coordinate system used locally in plane for constant φ. Ω denotes the angular velocity of the actuator driving the flow.

has provided the main motivation for the experiments in the torus employed in this work.

While certain aspects of curved pipe flow are going to be described in more detail in the following section, the key features of the transition in curved pipes are as follows.

1. pipe curvature has a strongly stabilizing effect regarding the onset of turbulence,

2. transition to turbulence occurs gradually (as opposed to straight pipes),

3. stable traveling waves arise in the transitional flow (differing from straight pipes, too), and

4. turbulent flow from a straight pipe can be fully or partially relaminarized by passage through a curved (helical) pipe.

2.3.1 Coordinate system and governing equations

Flow through a curved pipe with radius a, coiled in a circle with radius R, is usually treated in a toroidal coordinate system (r, α, φ) as shown in fig. 6, where r denotes the distance from the center of the cross section of the pipe, α the angle between the radius vector and the plane of symmetry, i.e. the poloidal angle in the cross section, and φ the azimuthal or toroidal angle, i.e. the angular distance between two cross sections. The corresponding velocity components are $u = u_r$ in the radial, $v = u_\alpha$ in the poloidal (tangential) and $w = u_\varphi$ in the azimuthal (streamwise) direction. The toroidal geometry provides an ideal domain, with well defined boundary conditions, to investigate curved pipe flow.

The equations describing an incompressible three-dimensional flow with constant properties are the continuity and Navier-Stokes equations for the conservation of mass and momentum

$$\frac{\partial \boldsymbol{u}}{\partial t} + \boldsymbol{u} \cdot \nabla \boldsymbol{u} = -\frac{1}{\rho} \nabla p + \nu \nabla^2 \boldsymbol{u} \tag{7}$$

$$\nabla \cdot \boldsymbol{u} = 0 \tag{8}$$

According to Webster & Humphrey (1997) they can be written in toroidal coordinates as follows.

Continuity equation

$$\frac{1}{r\xi}\left(\frac{\partial}{\partial r}(r\xi u_r) + \frac{\partial}{\partial \alpha}(\xi u_\alpha) + \frac{\partial}{\partial \varphi}(r u_\varphi)\right) = 0 \ , \tag{9}$$

r momentum equation

$$\frac{\partial u_r}{\partial t} + (\boldsymbol{u}\cdot\nabla)u_r - \frac{u_\alpha^2}{r} - \frac{\cos\alpha}{\xi}u_\varphi^2$$
$$= -\frac{1}{\rho}\frac{\partial p}{\partial r} + \nu\left[\nabla^2 u_r - \frac{2}{r^2}\frac{\partial u_\alpha}{\partial \alpha} - \frac{u_r}{r^2} + \frac{\sin\alpha}{r\xi}u_\alpha + \frac{\cos\alpha}{\xi^2}\left(u_\alpha\sin\alpha - u_r\cos\alpha - 2\frac{\partial u_\varphi}{\partial \varphi}\right)\right] \ , \tag{10}$$

α momentum equation

$$\frac{\partial u_\alpha}{\partial t} + (\boldsymbol{u}\cdot\nabla)u_\alpha + \frac{u_r u_\alpha}{r} + \frac{\sin\alpha}{\xi}u_\varphi^2$$
$$= -\frac{1}{\rho}\frac{1}{r}\frac{\partial p}{\partial \alpha} + \nu\left[\nabla^2 u_\alpha + \frac{2}{r^2}\frac{\partial u_r}{\partial \alpha} - \frac{u_\alpha}{r^2} - \frac{\sin\alpha}{r\xi}u_r - \frac{\sin\alpha}{\xi^2}\left(u_\alpha\sin\alpha - u_r\cos\alpha - 2\frac{\partial u_\varphi}{\partial \varphi}\right)\right] \ , \tag{11}$$

φ momentum equation

$$\frac{\partial u_\varphi}{\partial t} + (\boldsymbol{u}\cdot\nabla)u_\varphi + \frac{u_\varphi}{\xi}(u_r\cos\alpha - u_\alpha\sin\alpha)$$
$$= -\frac{1}{\rho}\frac{1}{\xi}\frac{\partial p}{\partial \varphi} + \nu\left[\nabla^2 u_\varphi + \frac{2}{\xi^2}\left(\frac{\partial u_r}{\partial \varphi}\cos\alpha - \frac{\partial u_\alpha}{\partial \varphi}\sin\alpha - \frac{u_\varphi}{2}\right)\right] \ , \tag{12}$$

where

$$\xi = R + r\cos\alpha \ ,$$

$$(\boldsymbol{u}\cdot\nabla) = u_r\frac{\partial}{\partial r} + \frac{u_\alpha}{r}\frac{\partial}{\partial \alpha} + \frac{u_\varphi}{\xi}\frac{\partial}{\partial \varphi} \ ,$$

and

$$\nabla^2 = \frac{1}{r\xi}\left[\frac{\partial}{\partial r}\left(r\xi\frac{\partial}{\partial r}\right) + \frac{1}{r}\frac{\partial}{\partial \alpha}\left(\xi\frac{\partial}{\partial \alpha}\right) + \frac{1}{\xi}\frac{\partial}{\partial \varphi}\left(r\frac{\partial}{\partial \varphi}\right)\right] \ .$$

As Webster & Humphrey (1997) point out, the respective curvatures of two of the toroidal coordinate axes (α and φ) lead to the appearance of several centrifugal and Coriolis force terms in the equations for conservation of momentum. For example, in the r-momentum equation, the two additional terms correspond to centrifugal forces and result from the cross-stream velocity (u_α^2/r) and streamwise velocity ($\cos\alpha u_\varphi^2/\xi$), respectively. It is the centrifugal force terms involving the streamwise velocity component that are primarily responsible for the counter-rotating Dean vortices.
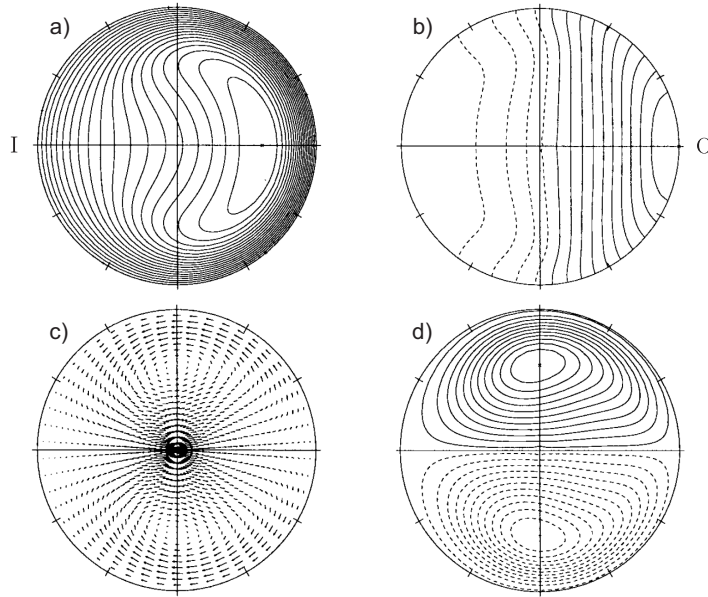
Figure 7: Laminar flow in a curved pipe, Re $= 1000, \delta = 0.01$. a) iso-contours of the streamwise (axial) velocity, b) pressure distribution, c) vector plot of the secondary flow, d) contour lines of the streamfunction. I denotes inner bend, O outer bend. From Hüttl et al. (1999).

2.3.2 Velocity and pressure distribution

The overall fluid mechanics of laminar and also turbulent flow in curved pipes is well understood. About the qualitative and quantitative characterization of both clearly laminar and turbulent flow there is common consensus, although the exact quantitative results of the various studies differ. Quite recent of origin the main results can be found consolidated and clearly represented in (Hüttl et al. 1999) for laminar and in (Hüttl & Friedrich 2000, 2001) for turbulent flow.

The bending of the duct causes a centrifugal force on the flow directed opposite to the direction of the bend, while a cross-stream pressure gradient, balancing the centrifugal force, gives rise to secondary flow. Hüttl et al. (1999) point out that the centrifugal force acting on the flow is proportional to the mean velocity squared and the curvature of the pipe, as indicated by the Dean number (De $= \mathrm{Re}\sqrt{a/R} = (Ud/\nu)\sqrt{a/R}$). Close to the wall, where the velocity is small, the centrifugal force is small, too. In return, close to the center of the curved pipe where the velocity is high, the centrifugal force has a maximum and acts radially outwards. Near the wall the pressure gradient can not balance the radially outward centrifugal force and consequently the flow is forced inwards and finally towards the center of the torus. Due to continuity, the rapidly moving central part of the mean flow is forced outward. This mechanism gives rise to the so called secondary flow perpendicular to the main flow direction. The streamwise velocity profile is considerably modified and a significant increase in drag is observed. The in-plane velocities of the secondary flow are in the range of one magnitude lower than the streamwise flow.

Fig. 7, taken from Hüttl et al. (1999), shows the characteristic contour lines (a) of the streamwise (axial) velocity that are symmetric to the horizontal axis but asymmetric about an imaginary vertical midplane. The position of the maximum is forced outwards, yielding a steep

25
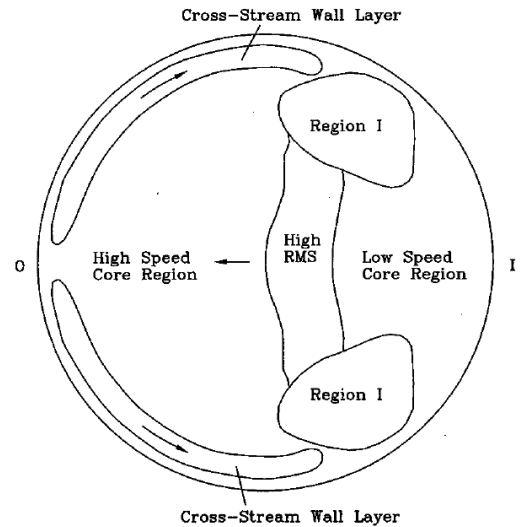
Figure 8: Sketch indicating characteristic regions of the flow in the coiled pipe cross section. Region I and especially the region of high RMS emerge during transition to turbulence. I denotes inner bend, O outer bend. From Webster & Humphrey (1997).

velocity gradient near the outer wall. The contour lines, which would be circles for flow in a straight pipe, are deformed. The contour lines of the pressure (b) are almost rectilinear and perpendicular to the horizontal axis in the core of the cross-section. As there is no pressure minimum visible in the center of the recirculation cells, (b) also highlights that the term Dean *vortex* is inadequate if a pressure-minimum criterion is used to define vortices. *Dean vortex* is used in the very general sense of *circular movement around a common center* hence (on definitions of vortices see e.g. Lugt 1979, Jeong & Hussain 1995). (c) is showing the secondary flow visualized by vector plots and (d) the corresponding contour lines of the streamfunction. The outwards movement of the cross-stream flow in the core region and inwards movement at the wall as well as the bifurcation at the outer wall and the confluence at the inner wall, dividing the upper and lower half of the cross-section into two symmetric recirculation cells, are clearly visible. By comparing the structure of the cross-stream velocity vectors of (c) with the streamwise velocity contours of (a) it becomes clear that fluid with high streamwise velocity in the outer half of the cross section is convected toward the inner wall by the cross-stream flow leading to the elongated contour shapes of the streamwise flow. With increasing Reynolds number and/or increasing curvature the pressure-driven wall layers returning the cross-stream flow to the inner wall become thinner and are confined to a distance $\approx 0.1a$ from the wall (Webster & Humphrey 1997).

From Webster & Humphrey (1997) the useful concept of characterizing and labeling regions of the cross section is adopted. Fig. 8 shows a summary sketch of the regions of flow in the pipe cross section presenting the most relevant features. They are described here in order to facilitate later discussion of the complex cross-stream motion. The regions of pressure driven flow directed toward the inner half of the pipe cross section are denoted as the *cross-stream wall layers*. The *core region* corresponds to the bulk of the cross-stream flow, which is centrifugally driven toward the outer wall. This is further subdivided into *high-speed* and *lowspeed* regions to indicate the relative magnitude of the streamwise velocity. *Region I* indicates the regions near the top and bottom walls in the inner half of the pipe cross section, where Webster & Humphrey

26

(1997) observed the streamwise RMS velocity (i.e. the fluctuations of the streamwise velocity in the transitional regime) to be the largest. A high RMS region connecting the two Regions I is also shown.

For fully developed turbulent flow the effects of curvature on the overall picture of the mean flow are qualitatively similar. Even though there are rather few studies on fully developed, statistically steady turbulent flow in curved and helically coiled pipes, e.g. Patankar et al. (1975), Lin & Ebadian (1999) and Hüttl & Friedrich (2000, 2001) show the truncation (i.e. a decrease of the maximum, see also sec. 5.3.2) of the streamwise velocity profile for turbulent flow. The more uniform distribution of the velocity over the cross section for turbulent flow is also typical for straight pipe flow. At the same time the Dean vortices are maintained.

2.3.3 Friction factor and pressure loss

Since exact knowledge of the friction factor is very important for industrial dimensioning and design, most of the early investigations of curved and helical pipe flow were motivated by the search for reliable correlations for pressure drop. The well known major difficulties of finding an universal and all-purpose applicable law apply similarly for curved pipes as for straight pipes (among many others, see e.g. Nikuradse 1933, Colebrook 1938, Moody 1944, Romeo et al. 2002, Shockling et al. 2006, Allen et al. 2007).

In short, the energy loss or pressure difference Δp due to friction for a Newtonian liquid flowing through a straight pipe can be calculated with the Darcy-Weisbach equation (Moody 1944)

$$\Delta p = \frac{\rho u^2}{2} \cdot f_D \cdot \frac{L}{d} \tag{13}$$

In this equation f_D is the so-called Darcy (or also Moody) friction factor and ρ the density, u the bulk (mean) velocity, L the length of the pipe and d the hydraulic diameter of the pipe. Also the Fanning friction factor defined as

$$f_F = \frac{f_D}{4} \tag{14}$$

is commonly used. In this work only the Fanning friction factor will be used.

For laminar flow the friction factor is easily obtained from the Hagen-Poiseuille equation

$$f = \frac{16}{\text{Re}} \tag{15}$$

Since, roughly guessed, more than a hundred of correlations for turbulent flow in straight pipes have been published, only the easy to use *explicit* approximation for turbulent flow in smooth pipes and $\text{Re} < 10^5$, called Blasius correlation with

$$f = \frac{0.3164}{4 Re^{0.25}} \tag{16}$$

is noteworthy. It is widely accepted that the Blasius friction relationship provides the best representation of friction factor data of available formulations for $\text{Re} < 10^5$ (McKeon et al. 2005). For further particulars concerning pressure drop in straight pipes reference to the above cited literature is made.
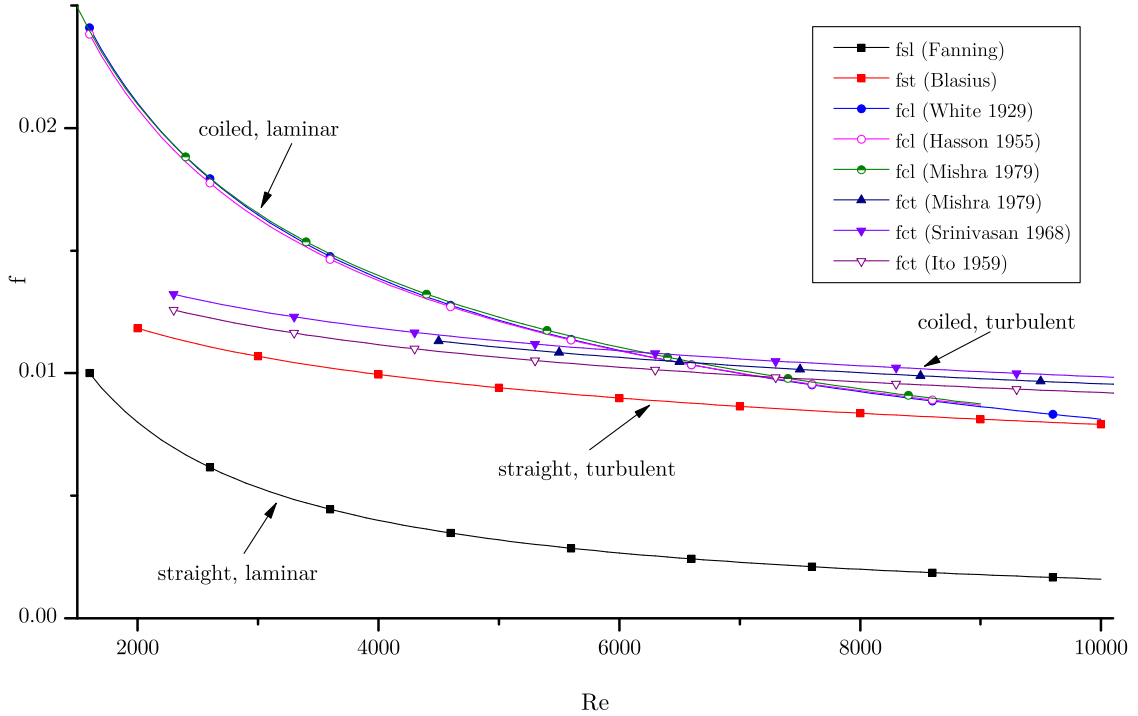
Figure 9: Graphical representation of selected friction factors for straight and coiled (same as in table 1, drawn here for $a/R = 0.049$) pipes, in each case for laminar and turbulent flow. The correlations for f_{CL} match so well that they almost superpose for the resolution provided. Some graphs are cut at the range of validity specified by the respective authors (see table 1). For the calculation of f_{CL} (15) was used, also above $\text{Re} = 2000$.

The friction factor correlations for curved pipe flow (f_{curved}), which can be found in the literature, are mostly expressed compared to the friction factor in a straight pipe ($f_{straight}$). Due to the lack of global solutions for the whole geometrical range, a number of design correlations were developed for the friction factor with the applicability of each correlation restricted to certain geometrical or flow conditions. Disagreement often occurred between investigators on the relevant dimensionless groups and form of dependency in the design correlations. Some of the proposed correlations have at least one of the following disadvantages: (a) the formulas are only applicable in a limited range of Dean numbers, (b) correlations do not satisfy the condition $f_{curved} \rightarrow f_{straight}$ if $\text{De} \rightarrow 0$ (Vashisth et al. 2008). However, most studies agree that the friction factor ratio $f_{curved}/f_{straight}$ scales with $\text{De}^{1/2}$, at least for large Dean numbers (Berger et al. 1983).

As pointed out by Vashisth et al. (2008), expressing the pressure drop in a coiled tube in comparison to that in a straight tube causes additional problems. The ratio for laminar flow, f_{CL}/f_{SL}, should in the strict sense be used only up to the value of a Reynolds number equal to the critical Reynolds number of flow in straight tubes, i.e., ≈ 2000. Beyond this value, the flow in the straight tube *usually* ceases to be laminar, whereas in coiled tubes, it persists to be laminar up to much higher Reynolds number, so the use of a different correlation for f_S above $\text{Re} = 2000$ will result in an additional break in the correlation, without any actual physical

Reference	Correlation	Range of Validity
Mishra & Gupta (1979)	$\dfrac{f_{CL}}{f_{SL}} = 1 + 0.033(\log \mathrm{De})^4$	laminar; $1 < \mathrm{De} < 3000$
Hasson (1955)	$\dfrac{f_{CL}}{f_{SL}} = 0.0969\sqrt{\mathrm{De}} + 0.556$	laminar; $30 < \mathrm{De} < 2000$
White (1929)	$\dfrac{f_{CL}}{f_{SL}} = \left\{ 1 - \left[1 - \left(\dfrac{11.6}{\mathrm{De}} \right)^{0.45} \right]^{\frac{1}{0.45}} \right\}^{-1}$	laminar; $12 < \mathrm{De} < 2000$
Mishra & Gupta (1979)	$f_{CT} = f_{ST} + 0.0075 \left(\frac{a}{R} \right)^{1/2}$	turbulent; $4500 < \mathrm{Re} < 10^5$, $0.003 < a/R < 0.15$
Ito (1959)	$f_{CT} = \frac{1}{4} \left(\frac{a}{R} \right)^{0.5} \left\{ 0.029 + 0.304 \left[Re \left(\frac{a}{R} \right)^2 \right]^{-0.25} \right\}$	turb.; $0.034 < \mathrm{Re} \left(\frac{a}{R} \right)^2 < 300$ $0.0012 < \frac{a}{R} < 0.067$
Srinivasan et al. (1968)	$f_{CT} = \dfrac{0.084 \left(\frac{a}{R} \right)^{0.2}}{\mathrm{De}^{0.2}}$	turb., $\mathrm{De}_c < \mathrm{De} < 14000$ $0.0097 < a/R < 0.15$

Table 1: Table of selected friction factor correlations in curved pipes. f_{CL} denotes the friction factor for laminar and f_{CT} for turbulent flow. More comprehensive collections of correlations can be found in e.g. Ali (2001), Naphon & Wongwises (2006), Vashisth et al. (2008) and Gupta et al. (2011).

background in the curved pipe flow. At the same time it seems acceptable to use f_{SL} even above Re = 2000 since the flow in a straight pipe *can* be laminar even for higher Re (see section 2.2).

Table 1 provides an overview of a few selectively chosen, exemplary friction factor correlations for laminar and turbulent flow in curved pipes. As depicted in figure 9, especially the available correlations for laminar flow in a curved pipe agree very well. The correlations for turbulent flow in curved pipes scatter more but still correspond well. Not surprisingly, it can be clearly seen that for both the laminar and the turbulent case the correlations for curved pipe flow show higher friction factors than for straight pipes. It is worth noting, however, that the difference between curved and straight pipes is by far less for turbulent flow than it is for laminar flow, and that there is no or less discontinuity for the curved pipe correlations as the correlations cross and overlap in the range of approx. 6000 < Re < 7000. This indicates the challenge of delineating exact boundaries between the laminar and turbulent regime in curved pipe flow, as will be also further discussed in section 2.3.4. The most striking fact visible in figure 9, that the friction factor for laminar flow in a curved pipe is actually *higher* than that for turbulent flow in a curved pipe in the low Reynolds numbers regime (below Re $\approx$ 6000 in the case displayed), is hardly ever mentioned nor explained in the literature known to the author.

Ali (2001) tried to develop generalized pressure drop correlations for isothermal flow through regular helical coil tubes, i.e. also for the zero pitch case of a torus, and provides a good overview of the various obstacles connected with it. He points out that in fact most available correlations show a break at a certain Reynolds number, and that f_C and Re do not characterize the coil flow completely. Therefore, one will get different curves for different curvature of the coils. Furthermore, he conjectures the existence of *four* regimes of curved pipe flow. In the proposed scenario the low laminar flow regime extends approximately up to a first critical Reynolds number of 500, as the secondary flow effect on pressure drop seems to be comparatively less in this regime, although there is a continuous increase in the intensity of secondary flow with Reynolds number. The second regime of laminar flow extends up to a second critical Reynolds number of approximately 6300. In this regime, the continuous increase of secondary flow in coiled tubes causes a continuous increase in the coiling effect factor. Hereafter, in the third regime of 'mixed' (i.e. laminar and turbulent) flow, turbulence sets in. The coiling effect factor tends to increase slightly up to a third critical Reynolds number of approximately 10.000, till the intensity of turbulence in coil flow becomes comparable to that in the straight tube. Thereafter, the presence of secondary flow over and above turbulence in the coiled tube tends to increase the coiling effect factor once again. Yet the four regimes proposed by Ali (2001) are derived from a solely empirical and a little vague observation of friction factor data and lack of physical explanation.

Cioncolini & Santini (2006) carried out an an experimental study to investigate the transition from laminar to turbulent flow in helically coiled pipes. They tested twelve coils with aspect ratios $A_r = R/a$ ranging from 6.9 to 369, and the relation between the onset of turbulence and coil curvature was analyzed from direct observation of the experimental friction factor profiles. They found only a soft kink in the $f(\text{Re})$ curve, indicating transition to turbulence.

Reference	Correlation	Condition	Re_{crit} for $A_r = 20.26$
Ito (1959)	$\text{Re}_{crit} = 20.000/(A_r)^{0.32}$	$15 < A_r < 860$	7.637
Kubair & Varrier (1961)	$\text{Re}_{crit} = 12.730/(A_r)^{0.32}$	$10 < A_r < 2000$	4.861
Srinivasan et al. (1968)	$\text{Re}_{crit} = 2100[1 + 12/(A_r)^{0.25}]$	$A_r < 200$	13.978
Cioncolini & Santini (2006)	$\text{Re}_{crit} = 30.000(A_r)^{-0.47}$ $\text{Re}_{crit} = 12.500(A_r)^{-0.31}$	$A_r \leq 24$ $30 \leq A_r \leq 110$	7.295

Table 2: Table of selected correlations for the critical Reynolds number (on the basis of Vashisth et al. (2008), table 4). The exemplary application of the correlations to $A_r = R/a = 20.26$ (as used in section 4.1) immediately shows the extremely inconsistent definition of a critical Reynolds number varying from 4.861 to 13.978 among the authors cited.

2.3.4 Critical Dean and Reynolds numbers

Even though the exact value and its circumstances are still a subject to various investigations, the critical Reynolds number for transition to turbulence in straight pipes can be narrowed down to $\text{Re} \approx 2040$ (see sec. 2.2) quite well. In straight pipes the transition to turbulence can be described as catastrophic, i.e. it is abrupt and distinct. The transition scenario in curved pipes is fundamentally different from the one in straight circular pipes: the transition is continuous and the onset of turbulence arises at markedly higher Reynolds numbers, depending on the curvature of the pipe. This impact of curvature has not been explained satisfactorily yet, although phenomenological conjectures have been formulated (Berger et al. 1983). The potential reason behind stabilizing the laminar flow is the secondary flow in a curved tube, resulting into a higher critical Reynolds number.

The seemingly continuous transition scenario has inflicted major difficulties in finding a critical threshold. Most correlations for the critical Reynolds or Dean number for transition in curved pipes are based on empirical relations found in friction factor measurements. As can be retrieved from the exemplary selection shown in table 2 there is everything but good agreement amongst the various correlations published, apart from the fact that they all agree on a considerably higher Reynolds number.

Of more relevance for the current work are the observations of Sreenivasan & Strykowski (1983). In an investigation focusing on relaminarization phenomena they noticed that the critical Reynolds number for transition in a curved pipe is different at different locations of the cross-section. Their hot-wire traces, reproduced in fig. 10, were taken in the horizontal midplane of the cross section about $0.25\,a$ from the inner and outer wall respectively of a curved pipe. Near

the outer wall, they found transition to occur by the formation and coalescence of 'bursts' of high-frequency turbulence. Near the inside wall, on the other hand, they found a completely different process: a disturbance at a selected frequency grew to a fairly large amplitude before higher harmonics started to appear (the third trace from the bottom on the left). Soon after, higher and higher frequencies started to appear in a relatively short span of Reynolds numbers.

They approached this observation by determining an upper and lower critical Reynolds number (see fig. 11). They also found that the critical Reynolds number, which corresponds to the first appearance of turbulence everywhere at the chosen cross-section ('lower critical'), reaches a maximum value and then drops as the curvature increases. The more important observation of a single selected frequency for Re $\approx$ 5000 will be taken up again in the sec. 2.3.6.

Figure 10: Typical oscillograms of hot-wire traces during transition (R: Reynolds number) in a coiled pipe with radius ratio $\delta = 0.058$, taken at $0.25\,a$ from the inner and outer walls respectively. From Sreenivasan & Strykowski (1983). Near the inside wall, a periodic signal grows to a fairly large amplitude before higher harmonics start to appear. Near the outside wall transition occurs by the formation and coalescence of bursts of turbulence.
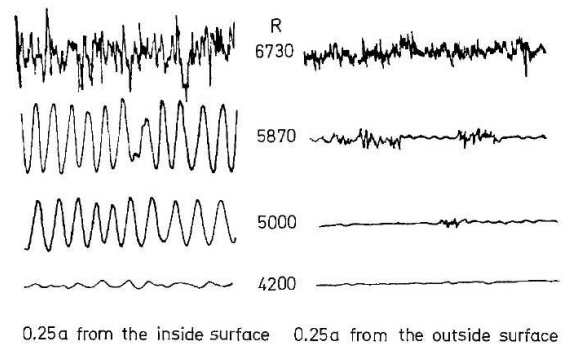
2.3.5 Development lengths

The distance from the inlet of a pipe to the first location of a fully developed pipe flow defines the hydrodynamic entrance or development length L. Superimposed diffusion and convection, together with order-of-magnitude considerations, suggest that the normalized development length can be expressed as $L/d = C_0 + C_1 \mathrm{Re}$ with $C_0 = 0.619$ for $\mathrm{Re} \to 0$ and $C_1 = 0.0567$ for $\mathrm{Re} \to \infty$ in straight pipe flow (Durst et al. 2005). Mostly in the literature a correlation of the form $L/d = C\mathrm{Re}$ is being used, where $0.049 < C < 0.068$ (see table 1 in Durst et al. (2005)).

As already shown for friction-factor correlations (sec. 2.3.3), correlations for development

Figure 11: Asymptotic values of the critical Reynolds numbers in the curved pipe section, measured at the end of 20 coils, as functions of the radius ratio (from Sreenivasan & Strykowski 1983). The strong increase of the critical Reynolds numbers for small curvature is readily seen. The conservative lower value of Re ($\bar{R}_{cr}$) corresponds to the first appearance of a burst near the outer wall (see fig. 10) of the curved pipe.
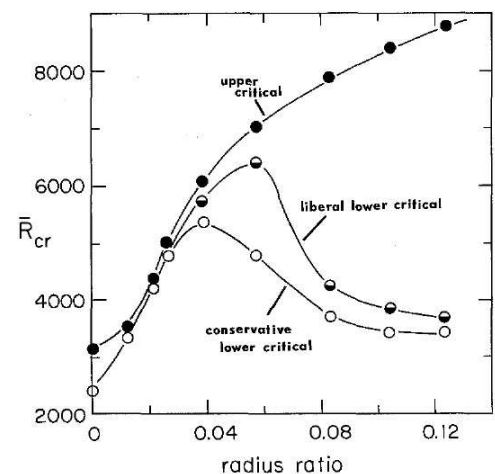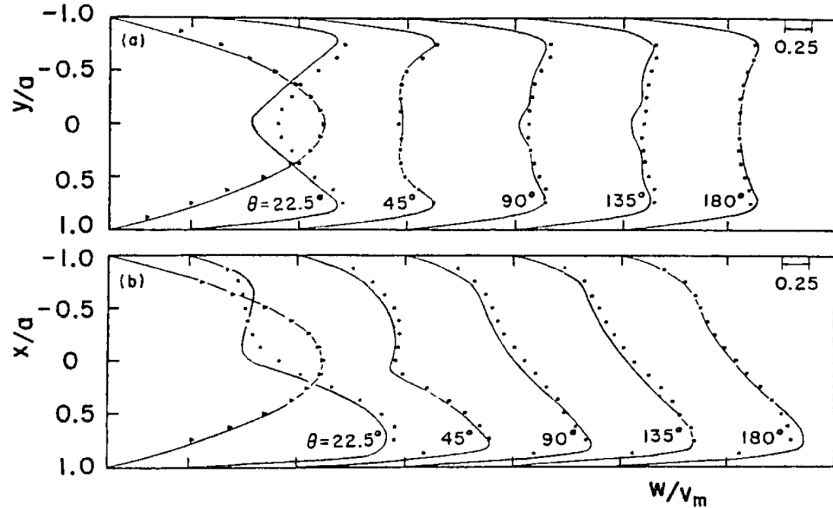
Figure 12: Development of axial velocity profiles with parabolic profile at the inlet for $R/a = 29.1$ and De $= 372$. Numerical results from Patankar et al. (1974) (line) in comparison to the experimental results (dots) of Austin & Seader (1974) (figure taken from Ito 1987). a) vertical plane and b) plane of symmetry.

lengths in curved pipes (L_c) are often expressed in relation to the one in straight pipes (L_s) too. A number of analytical (Singh 1974, Yao & Berger 1975), numerical (Patankar et al. 1974, Humphery 1977, Guan & Martonen 2000) and experimental (Austin & Seader 1974, Agrawal et al. 1978, Bovendeerd et al. 1987) correlations have been proposed by various workers for entry development in curved tubes. For a more detailed review see e.g. Vashisth et al. (2008) and, in particular, Berger et al. (1983).

Apart from agreeing in a substantially shorter development length in curved pipes compared to that in straight pipes no common consensus can be found. Exemplary the correlation of Yao & Berger (1975)

$$L_c = e_1 a(\text{Re})^{1/2}\delta^{-1/4} \tag{17}$$

where e_1 is weakly dependent on δ and Re and lies between 2 and 4 is quoted. Simple considerations show that only for very small Re and large δ a flow could hence ever become fully developed within a torus, i.e. within one revolution of a curved pipe. For transitional Reynolds numbers in the range of 5000 and a $\delta = 0.049$ as used in the experiments described below a fully developed flow seems far out of reach.

Complementary, the results from Patankar et al. (1974) and Austin & Seader (1974) are reproduced in fig. 12, showing a 'practically' fully developed flow after about 90° of the bend. But even if the development length to establish a sufficiently (95 %) developed laminar flow is estimated based on the correlation for straight circular pipes after the much shorter distance

$$L_{95}/d \approx \text{Re}/30 \tag{18}$$

(Tritton 1988), for Re $= 4\,000$ this condition requires a development length of $133\,d$ for the experimental setup used in sec. 4.1, where the arc length of the torus at $r = 0$ is $\approx 64d$. As

(18) cannot even be roughly satisfied hence, the development length needs further attention and investigation (see sec. 5).

2.3.6 Stability, bifurcations and traveling waves in curved pipes

Since transition to turbulence in curved pipes is in the main focus of this work, emphasis is put on previous works and literature dealing with transitional phenomena in curved pipe flow. The literature is rather scarce though.

One of the first documented observations of the transition scenario in curved pipes, derived from experiments with color injections into a helical pipe, reads as follows:

As in Reynolds' experiments with a straight pipe, it was found that the flow was steady up to a certain speed. At this speed the color band began to vibrate in an irregular manner, but it still seemed to retain its identity through at least on whole turn of the helix. This indicates that the unsteadiness was not at first of a type which gives rise to diffusion of momentum by eddies and hence to a rapid rise in resistance. [...] On increasing the speed this irregular vibration increased in violence till, at a point which could be measured with some accuracy, the stream became completely turbulent so that the identity of the color band was lost in a distance of a few millimeters from its source (Taylor 1929).

Already 54 years later, Sreenivasan & Strykowski (1983) – investigating flow at low Reynolds number regime that was turbulent in a straight pipe becoming laminar in a subsequent coiled section – were the first to describe large differences between transition near the inner and outer walls of a coiled pipe (see sec. 2.3.4). As was already shown in fig. 10, near the inside wall a disturbance at a selected frequency was found to grow to a fairly large amplitude before higher harmonics started to appear. Soon after, higher and higher frequencies started to appear in a relatively short span of Reynolds numbers.

Webster & Humphrey (1993) were the first to quantitatively investigate the unsteady three-dimensional flow through a helical pipe during transition with visual observations and LDV measurements, revealing distinct periodic low frequency flow oscillations in the range $5060 < \mathrm{Re} < 6330$ and $A_r = 18.2$. They observed the onset of a periodic signal at around $\mathrm{Re}_{crit} = 5060$ and the onset of turbulent fluctuations at $\mathrm{Re} = 6330$. They specified the nondimensional frequencies found with $fd/U = 0.25$ (i.e. $0.95\,\mathrm{Hz}$ at $\mathrm{Re} = 5480$) and 0.5 respectively. For $\mathrm{Re} = 5060$ they determined the wavelength λ to be $18.4°$ or $(2\pi c)/20$ and the wave phase speed (celerity) to be $16.3°/\mathrm{s}$ or $0.825U$. They assumed the mechanism of the periodic flow to result from an instability of the outward-directed midplane jet.

Soon later Webster & Humphrey (1997), by performing complementary numerical calculations for one Reynolds number (5480) only, found a traveling wave perturbation to the fully developed Dean vortex flow solution. As they chose the length of the computational domain equal to the experimentally measured wavelength, the traveling wave was forced to exhibit a priori prescribed features.

In discussing their results, Webster & Humphrey (1997) point out that the flow was perfectly symmetric about the midplane at every instant and at every streamwise location, thus the

Figure 13: One (at $7/8\lambda$) out of a sequence of 8 instantaneous velocity fields of one full wavelength. Upper part: the cross-stream velocity perturbation vector field (velocity fluctuations). Lower part: contours of the instantaneous streamwise velocity component. From Webster & Humphrey (1997).
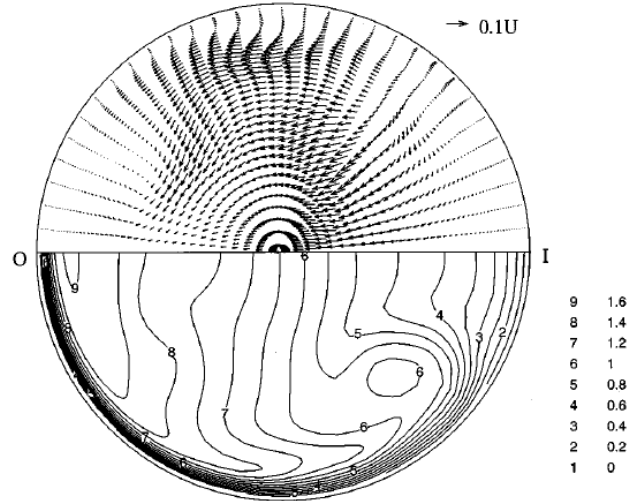
instability is a varicose mode. The mode showed oscillating velocities with maximum RMS (root mean square) values in the proximity of the inner turning point of the Dean vortices, i.e. Region 1 (see fig. 8). Fig. 13 shows one figure (at $7/8\lambda$) out of a sequence of instantaneous velocity fields at pipe cross sections spaced $\lambda/8$ increments apart. The cross section is divided at the midplane. The upper portion shows the cross-stream velocity perturbation, i.e. the cross-stream velocity field minus the cross-stream mean velocity ($u_r - \bar{u}_r$, $u_\alpha - \bar{u}_\alpha$). The lower portion shows contours of the instantaneous streamwise velocity component u_φ. Even though quantitative comparison with experiments was not possible for Webster & Humphrey (1997) due to the purely qualitative (flow-visualization) nature of the numerical results, many interesting features of the instability were quite clearly compiled.

By comparing the location and shape of the contours of streamwise velocity for 8 different locations within one full wavelength λ they verified that the streamwise velocity varies significantly in Region I (see fig. 8) due to a periodic convection from the cross-stream wall layers into Region I. Furthermore, the perturbation velocity vectors showed that the cross-stream flow varies significantly during one wavelength both in the core region and in the wall layers.

Webster & Humphrey (1997) explicate that when the streamwise velocity is relatively large in Region I, the centrifugal force is correspondingly large and directed toward the outer wall. The cross-stream velocity component in the wall layer directed toward the inner wall is thus reduced and its ability to convect fluid with large streamwise velocity into Region I is correspondingly diminished. The centrifugal force thus decreases, which increases the cross-stream wall layer flow toward the inner wall, which in turn increases the streamwise velocity in Region I. This cycle repeats itself indefinitely since it is energized by the bulk streamwise velocity through the periodic variation in centrifugal force.

They hence conclude from their results that energy is transferred to the traveling wave from the mean flow through a complex interaction between the centripetal acceleration in the inner half of the pipe cross-section and the flow in the cross-stream wall layer. And as the flow perturbation consists of a pair of counter-rotating vortices aligned in the cross-stream circumferential direction they suggest that the traveling wave is a result of a *centrifugal instability of the cross-stream*

*flow* (distinct from the centrifugal force due to the streamwise velocity).

Only recently Piazza & Ciofalo (2011) investigated the flow in toroidal pipes of circular cross-section by three-dimensional, time-dependent numerical simulations using a finite volume method. The computational domain included a whole torus. Radius ratios δ of 0.3 and 0.1 were examined by imposing a streamwise forcing term, where the magnitude determined the bulk Reynolds number, which ranged from ≈ 3500 to ≈ 14.700. They detected consecutive transitions from stationary to periodic, quasi-periodic and ultimately chaotic flow.

For $\delta = 0.3$ and $4556 < \mathrm{Re} < 4605$ a supercritical Hopf bifurcation was found, giving rise to a traveling wave which took the form of a varicose streamwise modulation of the Dean vortex ring intensity. Subsequently they found a secondary Hopf bifurcation for $5042 < \mathrm{Re} < 5270$ which led to a quasi-periodic flow characterized by two independent fundamental frequencies associated with distinct traveling waves. The first wave was described to affect mainly the Dean vortex rings and to be similar to that observed in purely periodic flow. The second wave was described to be localized mainly in the secondary flow boundary layers and manifesting itself as an array of oblique vortices produced at the edge of the Dean vortex regions. Both the periodic and the quasi-periodic regimes found were characterized by an instantaneous anti-symmetry of the oscillatory components with respect to the equatorial midplane of the torus.

For $\delta = 0.1$ Piazza & Ciofalo (2011) found a direct transition from a steady to a quasi-periodic flow between $5139 < \mathrm{Re} < 5208$ associated with hysteresis. Starting from the quasiperiodic solution and letting the Reynolds number decrease, they obtained both quasi-periodic and periodic stable solutions at Reynolds numbers below the critical value, suggesting the existence of a subcritical Hopf bifurcation followed by a secondary Hopf bifurcation. Piazza & Ciofalo (2011) also point out that the traveling waves for $\delta = 0.1$ were instantaneously symmetric with respect to the equatorial midplane of the torus. Based on an analysis of Rayleigh's centrifugal stability criterion and their numerical results they support the view, as opposed to Webster & Humphrey (1997), that the transition from stationary to unsteady regimes is driven by a *centrifugal instability of the main (streamwise) flow located in the Dean vortex region, and not of the secondary flow*.

Even though the results of Webster & Humphrey (1997) and Piazza & Ciofalo (2011) partly contradict the experimental results to be presented in this work, the existence of a sequence of bifurcations to turbulence via a (traveling-wave) instability of the Dean flow can be considered well established.

The situation is considerably different for a number of two-dimensional studies on transition and stability in curved pipes which found bifurcations from the two vortex or Dean flow to a 4-vortex solution (see fig. 14). These studies are of theoretical interest only, since the perturbation modes found are not the three-dimensional modes which develop in a three-dimensional configuration. For the sake of completeness the investigations of e.g. Dennis & Ng (1982), Nandakumar & Masliyah (1982), Daskopoulos & Lenhoff (1989), Yanase et al. (1989), Dennis & Riley (1991), Jayanti & Hewitt (1992) and Siggers & Waters (2005) should be mentioned which demonstrated that four-vortex modes can develop as a second family of solutions at sufficiently high Dean numbers. For flows restricted to two dimensions Dennis & Ng (1982)
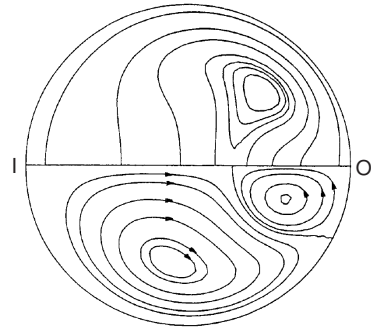
Figure 14: Four vortex solution for laminar flow in a curved pipe. From Nandakumar & Masliyah (1982). Upper half: lines of constant axial velocity, lower half: streamlines of secondary flow. The figure is taken from Ito (1987).

specified the critical Dean number to be $\mathrm{De}_{crit} = 956$, above which dual solutions can be found. For the geometry of the experimental setup used in this work this would correspond to a critical Reynolds number of 4303 above which 4-vortex flow could appear.

As an exception to the 'rule' established in sec. 1 to consider merely steady state flow, the work of Madden & Mullin (1994), del Pino et al. (2008) and Hewitt et al. (2011) is also mentioned. They used a torus model similar to the one presented in sec. 4.1, without internal actuator though, to experimentally investigate the *transient* flow during spin-up from rest and spin-down from solid-body rotation. Transition to a transient turbulent state was found triggered by a small-scale wavelike instability. The wave formed on a front that propagated from the inner wall of the toroidal container (after the torus was stopped). The wavelike instabilities that were observed in their experiments were of very short wavelength, presumably scaling with the boundary-layer thickness.

2.4 Comparison

The flow in a curved pipe may on one side be considered as a simple and minor modification of the flow through a straight pipe. On the other side, the effects of centrifugal forces change the flow fundamentally and make the flow in curved pipes substantially more complex. The mere existence of secondary flow due to curvature changes the transition scenario completely. A strongly stabilizing effect regarding the onset of turbulence and the occurrence of a gradual transition scenario are the most obvious consequences of curvature. While in straight pipes only unstable traveling wave solutions have been found stable traveling waves exist in curved pipe flow.

Theoretically, the limit and distinction between straight and curved pipes is easy and clear. One might hence expect stable traveling waves even for very slightly curved pipes. It would be interesting to know if the stable waves in curved pipes are 'connected' to the unstable waves in straight pipes. This would be achieved by the homotopy method, but is beyond the scope of the present study.

In this context it is interesting to note that Draad & Nieuwstadt (1998) have shown that even the Coriolis force due to the rotation of the earth can strongly distort the laminar velocity profile in a long straight pipe-flow facility. Velocity measurements taken in their facility exhibited an asymmetric velocity profile both in the vertical as well as horizontal direction with velocities that deviated strongly from the parabolic Hagen-Poiseuille profile.

3 Methods

The following chapter starts with a consideration of relevant system parameters, length and time scales. Subsequently, all measurement techniques applied, such as visual observations, laser-Doppler and particle-imaging velocimetry are introduced and discussed. A short introduction to their properties, conditions and operating modes is provided, supplemented by relevant crosslinks to the experimental setup and actual implementations in the experiments.

3.1 System parameter, length and time scales

Experiments with different dimensions and numerical calculations can be made comparable by means of the concept of dynamic similarity. Dynamic similarity of different systems is given if e.g. the ratio of forces in the systems under consideration is equal (Buckingham 1915, Spurk 1992). The similarity parameter commonly used in straight pipes is the Reynolds number Re (see sec. 2.2), describing the ratio of inertial forces to viscous forces by means of the internal diameter of the tube d, the average velocity normal to a cross section of the tube U and the kinematic viscosity ν of the fluid. These forces are relevant, as changes in the flow structure are initiated by diffusive and convective processes.

For the characterization of curved pipe flow an additional dimensionless parameter is needed, the Dean number De (see sec. 2.3), accounting for the aspect ratio $A_r = D/d$ or radius ratio $\delta = a/R$ of the curved pipe (the redundant definition of A_r and δ is mentioned since both are very common in the literature). As in this work the radius ratio is a constant value, for convenience the Reynolds number is used as determining parameter. The conversion factor between any Reynolds number indicated in this work and the correlating Dean number is just $\sqrt{\delta} = \sqrt{0.049}$, as indicated by (6) and table 3.

To determine the Reynolds number in the experimental setup described in sec. 4.1, apart from the given tube diameter d for the geometry, the values of U and ν need to be determined. U is determined via the angular velocity Ω of the actuator (sec. 4.4) driving the flow. The kinematic viscosity ν of the fluid is determined from a measured correlation valid for the actual temperature (sec. 4.2.2).

Due to the known circumstances established in sec. 2.3, the transition to turbulence in a curved pipe can roughly be expected to take place in the range $2000 < \text{Re} < 12.000$. This range specifies the basic design parameter for the experimental facility, i.e., the setup should allow the variation of the Reynolds number from 2000 to 12.000.

From chapter 2.1.1 it is known that a certain amount of time may elapse before the system, disturbed by an increase or decrease of the Reynolds number, reaches a new balanced state. Furthermore, the time span needed until the flow reaches the new equilibrium state tends to infinity in the immediate vicinity of the critical point. An estimate for the scaling of the time required to reach the new equilibrium state can be derived from the diffusion of momentum.

In cases where diffusion is the slowest physical process the diffusion of momentum can be

described by the diffusion equation

$$\frac{\partial u}{\partial t} = \nu \frac{\partial^2 u}{\partial x^2} \tag{19}$$

As a first approximation this gives

$$\frac{\Delta u}{\Delta t} = \nu \frac{\Delta u}{\Delta x^2} \tag{20}$$

and hence

$$\Delta t = \frac{\Delta x^2}{\nu} \tag{21}$$

for the period Δt in which momentum diffuses by the length Δx. Δt thus indicates the magnitude by which a perturbation spreads by Δx on behalf of diffusion.

If the diameter d of the tube is inserted for Δx and $\nu = 1.6$ mm^2/s (see sec. 4.2) for the viscosity, the time for momentum to diffuse by Δx amounts to $\Delta t = 574$ s. If the full length of the torus is considered for Δx, Δt amounts to even 640 hours.

For a good approximation of the formation of the asymptotic ($t \to \infty$) final state indeed the length of the torus is crucial, since momentum must diffuse over the entire length. Experimental observations have confirmed that the change in the flow from quasi-two-dimensional to three-dimensional structures (i.e. the first appearance of an instability) in fact takes a few minutes. The time needed to reach the new equilibrium state in the vicinity of the critical point was observed to be $\Delta t \approx 300 - 480$ s for $\mathrm{Re}_{crit} \approx \pm 20$. The time scale to reach the asymptotic final state, however, can be considerably higher (theoretically: $t \to \infty$).

For the sake of completeness the convective time scale shall also be mentioned. The advection equation

$$\frac{\partial u}{\partial t} + u \frac{\partial u}{\partial x} = 0 \tag{22}$$

can be approximated as

$$\Delta t = \frac{\Delta x}{u} \quad . \tag{23}$$

With

$$\Delta x = d \quad \text{and} \quad u = \mathrm{Re}\frac{\nu}{d} \tag{24}$$

this yields

$$\Delta t = \frac{1}{\mathrm{Re}} \frac{d^2}{\nu} \tag{25}$$

for the duration of the convective transport over a length d. For $\mathrm{Re} \gg 1$ this time-span is negligible compared to (21), showing that for the Reynolds numbers under consideration momentum diffusion is the slowest process.

3.2 Measurement techniques

Hydrodynamic instability is a dynamic phenomenon, best seen and demonstrated in motion pictures or animated graphics. Time-resolved measurements, photography and movie shots are an intrinsic ingredient for the investigation of such phenomena hence. Primarily used were Laser-Doppler velocimetry and particle-image velocimetry as two non-contact optical measurement methods, in which the flow is not disrupted by the insertion of a probe.

In the following the main methods applied are briefly described. For further and more detailed information on the measurement techniques described in this section see, e.g., Durst et al. (1987) and Ruck (1990) for LDV and Westerweel (1993), Prasad (2000), van Doorne (2004), van Doorne & Westerweel (2007), Raffel et al. (2007), Adrian & Westerweel (2011) for PIV.

3.2.1 Visual observations

For preliminary investigations, the flow was visualized by addition of suspensions of anisotropic light-reflecting glitter particles (see sec. 4.3 for specification). This allowed visual identification of pertinent flow structures. To ensure correct interpretation of results gathered with more sophisticated measurement techniques such as LDV and PIV, it is helpful to have information about the flow structures in advance. Furthermore, the critical parameters can be very well determined or at least narrowed down by visual examinations. In order to obtain as much information as possible about the existing structures, extensive visual examinations were performed.

Still photographs as well as video recordings were made with a *Nikon* D 7000 DSLR (digital single lens reflex) camera. This camera has a 23.6 x 15.6 mm CMOS sensor with 16.2 million effective pixels and is able to record movies with a frame size of 1.920 x 1.080 pixels at 24 fps (frames per second). For the video recordings the camera was mounted on an additional boom which rotated at the same speed as the boom for the actuator (see sec. 4.1). The setup hence allowed tracking and measurement of coherent structures by observations in the frame of reference rotating with the angular velocity of the sphere, as the camera (and hence the frame of reference) followed the flow practically exactly at the mean velocity. Since the mean flow velocity in the torus is $\sim 3\%$ less than the velocity of the actuator, the camera moved approximately with $1.03\,U$, i.e. slightly faster than the mean velocity (see sec. 5).

3.2.2 Laser-Doppler velocimetry

Laser-Doppler velocimetry (LDV) is based on the measurable frequency shift (Doppler effect) occurring at a relative motion of transmitter and receiver of a wave to each other. The realization of this physical effect for LDV measurement devices means that a laser beam is split into two beams with the aid of a beam splitter. At the measurement point these rays are made to cross. An interference fringe pattern is formed in the crossing volume. A particle (see sec. 4.3 for specification) which moves along with the fluid through the stripe pattern generates a scattered light signal in a photodetector whose frequency is proportional to the velocity component perpendicular to the fringes. LDV hence provides the local velocity at a point in the flow with

high temporal resolution and rather small amounts of data (the data rate used in the present setup was about 150 to 200Hz).

For investigations with LDV a 2D-LDV system (DANTEC Dynamics, argon-ion-laser model 5500A, 750 mW, class IV) was available at the laboratory. It was primarily used to record velocity time-series of the streamwise (azimuthal) velocity component at single points within the flow. Furthermore, velocity profiles of the streamwise velocity at Re = 2000 and Re = 3000 (i.e. in the still clearly laminar regime) were measured to compare the results with numerical data and PIV measurements.

3.2.3 Particle-image velocimetry

Particle-image velocimetry is based on the approximation $u \cong \Delta s/\Delta t$ for the velocity u, where Δs is the displacement of a (fluid or tracer) particle and Δt the time span. What makes PIV such a powerful tool in experimental fluid mechanics is that this simple principle can be applied simultaneously and fully automated to a huge amount of particles by means of modern measurement technology and data processing. The method is capable of measuring an entire flow field hence.

In 2D particle-image velocimetry velocity vectors are captured in a plane. The beam of a pulsed laser is expanded to a plane by means of a light-sheet optics or a lens system. The measurement plane is illuminated twice within a defined time interval Δt. With a camera, which is aligned normal to the illuminated plane, the light reflected from tracer particles seeded into the flow is captured. This creates 2 snapshots of particles which follow the flow. Camera and laser pulses are synchronized. The two resulting images are then evaluated by comparison.

The amount of data resulting from PIV measurements is substantially greater than that from LDV measurements. The maximum frame rate of the camera, limiting the temporal resolution of the PIV, is almost irrelevant for the present measurements. Currently common high-speed cameras and lasers provide maximum frame rates in the range of 1000 Hz and above, which is more than sufficient to resolve and capture the time-scales of the flow phenomena under investigation.

Stereoscopic or 3D PIV utilizes two cameras with separate viewing angles that look from different directions to the light sheet (i.e. the measurement plane). Each camera measures the particle displacement perpendicular to its viewing direction. To capture the displacement of the third axis two different projections of the velocity are obtained, one from each camera, and the complete velocity vector can therefore be reconstructed, as illustrated in fig. 15.

For the calculation of the 3D-vector fields, the two 2D-vector fields are mapped (dewarped) from the image planes onto the measurement plane of the light sheet and interpolated on a common grid. Then the displacement vectors from both cameras are combined to calculate the three components of the particle displacement. The dewarping could, in principle, be based on the exact knowledge of the geometry of the setup, but a software-based calibration procedure is advantageous to handle since all image distortions arising from imperfect lenses or light path irregularities (e.g. from air/glass/water interfaces) are compensated for automatically in one
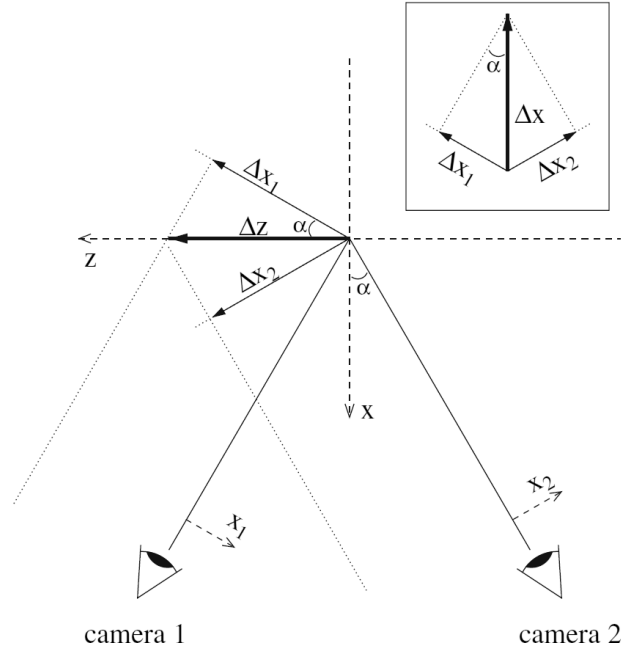
Figure 15: Illustration of the principle of stereoscopic PIV. A particle displacement Δz is observed by two cameras. Cameras 1 and 2 measure the projected displacements Δx_1 and Δx_2, from which the real displacement Δz can be reconstructed if the projection angle (α) is known. The inset shows the projection of a particle displacement Δx. The figure is taken from van Doorne & Westerweel (2007).

step too.

Both cameras have to be focused on the same plane in the flow and must be very accurately calibrated by means of a calibration target (see sec. 4.7). A major obstacle for an exact calibration is the need to position the calibration plate exactly at the same position as the light sheet, which can be quite tricky and difficult to accomplish. After calibration with the calibration target a so called self calibration procedure on particle images was used, where (calibrated) PIV images are employed for further refinement of the calibration, i.e. the mapping function (Wieneke 2005).

To obtain a completely *time-resolved* measurement of the velocity over the entire circular cross-section of the pipe, a high sampling frequency of the PIV system is needed. This allows to reconstruct 3D velocity fields applying Taylor's hypothesis (Taylor 1938). Converting time into space using the average streamwise velocity, a quasi-three-dimensional flow field is obtained which provides a good representation of the instantaneous three-dimensional flow structure. Since the light sheet in a 3D PIV setup can be oriented perpendicular to the main flow direction and, therefore, all flow structures are advected through the measurement plane, all three components of the velocity vectors in the measurement plane covering the entire cross-section of the pipe can be reconstructed by using two cameras (see fig. 16).

Previous investigators (van Doorne & Westerweel 2007) have shown the possibilities and potential of (High-Speed) Stereoscopic Particle Imaging Velocimetry (3D–SPIV) to investigate and capture the appearance and development of transitional flow in a pipe. The same principle shall
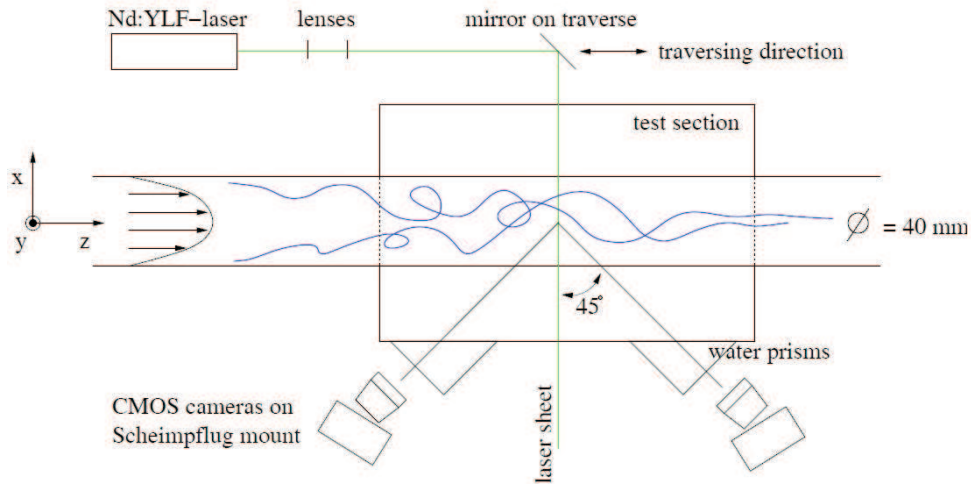
Figure 16: Schematic of High Speed Stereoscopic-PIV system with transparent test section for a straight pipe (from van Doorne 2004). Since the laser light sheet in this setup is oriented perpendicular to the main flow direction and, therefore, all flow structures are advected through the measurement plane, it is possible to reconstruct all three components of the velocity vectors in the measurement plane covering the entire cross-section of the pipe by using two cameras.

be applied in the experimental setup used for this work (see fig. 25).

For 2D-PIV measurements, a PIV system supplied by *DANTEC Dynamics* was available at the laboratory. It consisted of a double cavity SOLO PIV 200XT (Nd-Yag Laser, 200mJ/15Hz per cavity) including a FlowSense 2M camera kit (two FlowSense cameras, 1600×1200 px, max. 30Hz full frame, with 60 mm Nikon lenses, Scheimpflug-mounts etc.). Furthermore, a high-speed extension for frame rates of 1kHz a Nd:YLF Pegasus TR Laser (10 mJ with a repetition rate per head up to 10 kHz) and a NanoSense Mk III camera (1 kHz, 1280×1024 px, 2 GB, 60 mm lens) was available.

A stereo PIV high-speed system has been used to measure the three components of the velocity vectors over a cross section perpendicular to the flow and hence investigate and capture the appearance and development of transitional flow. It consisted of a pulsed *Quantronix* Darwin Duo laser (diode pumped Nd:YLF laser, wavelength 527 nm, 60 mJ total energy) and two *LaVision* Phantom high-speed cameras with a full resolution of 2400×1900 px. The actual resolution used was 1456×1704 px. The temporal resolution was set to 100 Hz.

The evaluation of the 3D-vector fields from the PIV images (fig. 17) was performed with commercial PIV-software (DaVis 8, *LaVision*). The interrogation area was 32×32 px with an overlap of 50%. The maximum particle displacement (between two frames) was approx. 11 px in horizontal and 8 px in vertical direction. Subsequently the acquired data were analyzed and exploited with *Mathworks* Matlab R2011b.

Figure 17: Raw image (one frame) of the light sheet in the cross-section of the tube with illuminated particles as seen by camera 1. As the camera is tilted approx. 45° and its axis also not perfectly aligned with the axis of the tube the circular cross-section is severely warped, causing an elliptic shape. Subsequent dewarping is done by means of a mapping function which is determined from the calibration images.
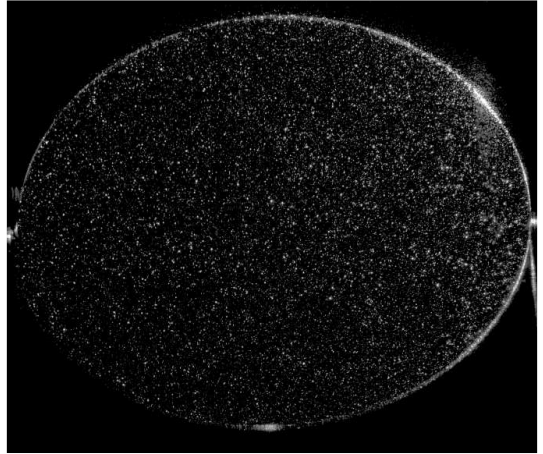
3.2.4 Pressure drop measurements

The pressure drop between two pressure holes (bore holes with internal diameter of 1 mm) was determined using a differential pressure sensor (*Validyne* DP103, ultra low range wet-wet differential pressure transducer). The pressure transducer was calibrated using a manometer (*Betz*) and had a full range of 140 Pa with an accuracy better than 0.35 Pa. The pressure holes were located at the top of the upper side of the tube ($\alpha = \pi$). The sampling rate was 10 ms. For all pressure drop measurements tap water was used as working fluid.

4 Experimental setup

In the following chapter the working principle and the main components of the experimental setup are presented and explained in detail. Furthermore, the fluids used for the experiments, the particles used for visualization and the actuator used to drive the flow are discussed. Remarks on some further components, such as the prism and the calibration target for 3D-PIV measurements, are given. As the experimental setup was more a permanently developing experiment in itself than a perfect final state throughout this work, some major modifications are described in the section about subsequent automatization. Considerations of errors and their quantification as well as a summary table of the design parameters conclude the chapter.

4.1 Working principle and main components of the experimental facility

To study hydrodynamic (in)stability in a toroidal domain not only permits systematic investigation of curved pipe flow but also combines aspects of symmetry with practicability. The geometry of a torus can be considered as a long pipe of circular cross-section which is bent into a circle so that its ends meet. To experimentally investigate the flow in a torus by means of optical visualization techniques, laser-Doppler velocimetry and particle-image velocimetry, a novel experiment had to be 'invented' and set up. The main challenge was to constantly drive the flow in a closed cavity such as a torus. The rather simple mechanism used to accomplish precisely adjustable constant flow in the torus was by placing an adequate actuator, realized as an iron sphere or a custom-made plunger, into it. The actuator is then controlled and moved from outside the cavity via a magnet.

Figure 18 provides a sketch of the driving mechanism and the main parts of the experimental setup. Two highly transparent and polished plexiglass disks, where a concentric notch of (half-) circular cross sections has been machined out, are put together such that they generate a toroidal cavity. The toroidal cavity is filled with fluid. The steel sphere is driven by a magnet mounted on a rotating arm. To achieve a constant, precisely adjustable flow rate in the torus the boom is rotated, and thereby drives the sphere and hence the flow, by an electric gear motor and a sensor to measure the angular velocity (both not shown in fig. 18).

When measuring flow details with PIV a large tube diameter d is desirable. van Doorne (2004) and Hof et al. (2004) used tube diameters of $40\,\mathrm{mm}$ for their PIV measurements in straight pipes. To machine such a diameter or radius respectively as a concentric notch into the plexiglas disks would require the use of a computer numerically controlled machine which was not available at our workshop. For our workshop the maximum producible radius for the tube with custom made circular profiled form cutter blades was about $30\,\mathrm{mm}$. Commercially available ferromagnetic spheres have standardized sizes in mm-increments. Since rolling motion of the ferromagnetic sphere had to be permitted in the tube, which was used as actuator (see 4.4.1) in the experimental facility, a diameter of $30.3\,\mathrm{mm}$ was chosen for the tube.

As small radius ratios are in the focus of interest, a large coiling diameter of the torus was desirable as well. As our workshop is limited to overall diameters of turning workpieces of maximum of $700\,\mathrm{mm}$ due to the existing turning lathe, the plexiglass disks were first roughly
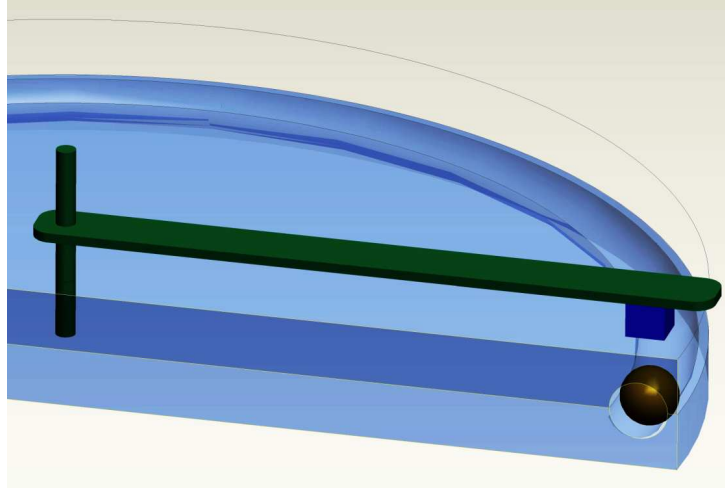
Figure 18: Illustration of the mechanism used to accomplish constant flow in a torus: two disks of plexiglas, where a concentric notch of (half-) circular cross sections has been machined out, and a rotating boom driving a sphere by means of a magnet.

cut to 700 mm and then machined to an outer diameter of 680 mm. As some supporting area with space for bolting the two disks together and also gasket contact face is needed, a diameter of $D = 614$ mm was chosen for the torus, yielding a radius ratio (aspect ratio) of $\delta = d/D = 30.3$ mm/614 mm $= 0.0493$. To achieve a surface finish of the tube comparable to glass pipes, its surface was polished. The manufacturing tolerance of the torus dimensions is $D = 614 \pm 0.1$ mm and $d = 30.3 \pm 0.03$ mm respectively.

Figure 19 provides a more detailed assembly drawing with the main parts of the experimental setup. The shaft (1) is rotating around the torus axis, driven by a geared direct current motor, and a rotating boom (2) directly connected to the shaft. A flat pot magnet (3) with threaded stem is incorporated to the rotating boom right below the centerline of the tube, leaving an adjustable distance of 1 mm to the lower plexiglass disk (4). Upper (5) and lower disk are bolted (6) together and sealed using a 2.5 mm rubber O-ring (7) in a 2.2 x 2.5 mm notch. Before tightening the bolts the O-ring protruded the notch 0.3 mm. A total of 32 (16 outside and 16 within the torus-notch, in a distance of $\varphi = 22.5°$) screws is used to ensure leakproof tightness.

Figure 20 is showing a picture of the experimental setup without the torus plates, i.e. the stand with base plate, drive mechanism, shaft and rotating boom. The drive system consists of a geared direct current motor (nominal voltage 24V, nominal power 35W, nominal torque 3Nm) in connection with a belt drive (large pulley: 72 teeth, small driving pulley: 15 teeth, toothed belt made of rubber composite: lenght = 819 mm, width = 13 mm). As the motor's characteristic curve of rotation speed vs. torque indicated quickly decreasing torque at low rotational speed, the belt drive and hence a gear reduction was chosen to ensure sufficient torque and running smoothness at very low rotational speed of the boom. To avoid any slippage or clearance, the belt drive had to be correctly tensioned via the tightening arm.

The speed of the motor is manually regulated via a *Philips* PE 1647 power supply serving as constant voltage source. It can be continuously adjusted with coarse and fine potentiometer
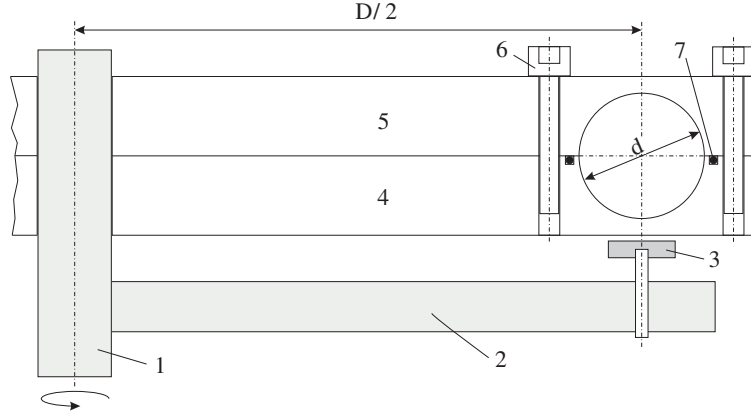
Figure 19: Assembly drawing of the experimental setup. 1 shaft, driven by a motor, 2 rotating boom, 3 magnet, 4 lower plexiglass disk, 5 upper plexiglass disk, 6 screws, 7 O-ring seal. The diameter of the torus $D = 614\,\text{mm}$, the diameter of the tube $d = 30.3\,\text{mm}$. Drawing not to scale.

to an output of $0 - 75\,\text{V}$ and $0 - 14\,\text{A}$ respectively. The stability against mains variations is specified to be $\leq 0.02\%$ or $2\,\text{mV}$. To measure the resulting rotational frequency Ω_r of the rotating arm, needed to determine the speed of the sphere, a very simple revolution-counter was used. The revolution counter was just a reed switch (electrical switch, operated by an applied magnetic field) connected to a stopwatch. The reed switch was mounted right under the lower plexiglas disk at a fixed location, pulsing when the pot magnet passes by, yielding one pulse/display update per revolution. The deviation of revolution times for a fixed voltage input was determined to be $\leq 0.3\,\text{s}$ (Panzer 2012).

To detect the temperature of the fluid in the torus, two very small Platinum SMD Flat Chip temperature sensors (*Vishay Beyschlag*, PTS 0603, $100\,\Omega$, $\text{L x W} = 1.55\,\text{x}\,0.85\,\text{mm}$) were used. Every sensor is mounted on the front end of a bracket pin with a diameter of $2\,\text{mm}$. The bracket pins are plugged in holes which were drilled into the upper plexiglas disk in a distance of $\varphi = \pi/2$, located at the top of the upper side of the tube ($\alpha = \pi$). The holes would just not shove through into the toroidal volume but leave a thin wall of approx. $0.08\,\text{mm}$ between the temperature sensors and the fluid in the torus. For data acquisition the two sensors were connected to a *Validyne* UPC 2100 PCI sensor interface card. The mean value of the two sensor signals, averaged over $20\,\text{s}$, was taken to determine the temperature in the torus with an accuracy of $\pm 0.1°\text{C}$.

Based on the measured revolution times and temperature in the torus, the bulk velocity, the viscosity (see 4.2.2) and hence the Reynolds number of the flow was computed. A change in Reynolds number was solely possible by manually changing the input voltage, i.e. the revolution time. It is important to notice that the designated Reynolds number for all measurements was based on the bulk velocity of the actuator, i.e. the rotation time of the boom. Since a small inevitable leak flow appears between actuator and torus wall, the actual mean velocity of the flow would always be slightly lower than the bulk velocity of the actuator.

As there was no automatic (re-)adjustment of the appointed angular velocity and no temperature controlled environment, the temperature had to be monitored frequently and, if needed,
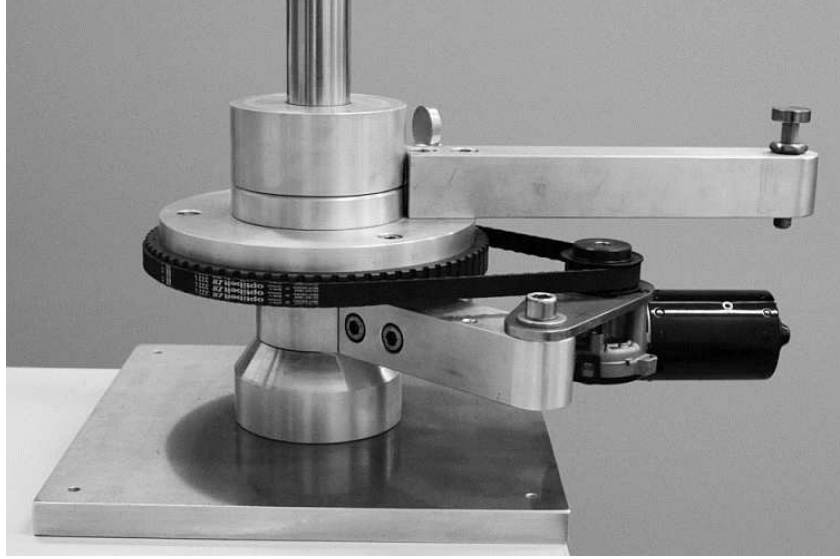
Figure 20: Picture of the bare stand where the torus is mounted on, consisting of base plate, drive mechanism (geared direct current motor with belt drive), shaft and rotating boom with the incorporated flat pot magnet. The motor is installed on a tightening arm to allow tensioning of the belt.

the revolution time reset. Although the low level of automation of the experimental setup left a lot of space for improvement and further automation (see 4.8), this setup already provided the possibility to investigate to flow in the torus for adjustable Reynolds numbers ranging from 0 to 15 000 with an accuracy of better than ±3%. By means of a larger driving pulley, i.e. a different gear transmission ratio, even higher Reynolds numbers would be easily achievable.

4.2 Fluids

As working fluids either pure tap water (for pressure drop measurements) or an refractive index matched mixture of distilled water and ammonium thiocyanate (for all other investigations, i.e. visual observations, LDV and PIV measurements) were used. For the tap water available correlations for the dynamic viscosity and density were employed. According to Kestin et al. (1978) or Weast & Astle (1988) the dynamic viscosity of (distilled) water for temperatures ranging from 10 to 35°C can be approximated by

$$\eta_w = 1.77721 - 0.05798\,T + 0.00125\,T^2 - 1.66039 \times 10^{-5}\,T^3 + 9.814 \times 10^{-8}\,T^4\,[\text{mPa·s}] \quad (26)$$

4.2.1 Matching the index of refraction

When viewed from the outside, objects placed inside containers with cylindrical walls (e.g. test tubes, beakers, pipes) appear distorted because of the curvature of the interfaces and the differing refractive indices of the media, generating phenomena such as unwanted displacement, hidden regions and multiple images (Lowe & Kutt 1992). Optical observations and measurements are strongly affected or even vitiated hence. To minimize the problems arising from the differing refractive indices the index of refraction of water ($n_w = 1.33$) can be changed by adding e.g.
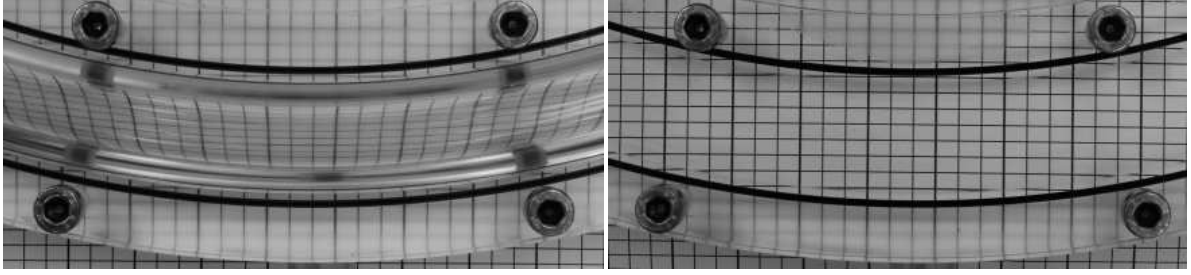
Figure 21: Two photos of a short section of the torus from above. To illustrate the effect of refractive index matching, a checkered pattern was printed on a sheet of paper and put below the plexiglas disks. The picture on the left was made with an empty torus, while on the right side the torus is filled with index matched fluid (distilled water with ammonium thiocyanate).

salt, glycerin or organic liquids (Budwig 1994, Hopkins et al. 2000) to match the refractive index of the plexiglass plates ($n_p = 1.492$).

As the refractive index of materials varies with the wavelength of light, some chromatic dispersion at the boundary between fluid and plexiglas at ambient light is unavoidable even in matched systems. The effect of dispersion is well known from prisms which cause different colors to refract at different angles, splitting white light into a rainbow. For that reason, in visual observations such as photographs as well as video recordings the wall of the torus will sometimes appear a little blurred and colored. Also for LDA-measurements, if more than one velocity is measured at the same time, matching indices of refraction for both beam wavelengths simultaneously is impossible, as the index of refraction is different for the green component of laser light and for the blue one. Only for PIV-measurements, where only one wavelength is used to illuminate the light sheet, a perfect index matching would be possible.

Since the index of refraction is temperature-dependent as well, matching indices of refraction was done accurately only to the second decimal point, yielding a tolerance of $n_w = 1.492 \pm 0.004$ measured with an *Abbe* refractometer. The two pictures in fig. 21 show gridlines as seen through the torus model from above when filled with air (left) and the index matched fluid (right). For the matching mixture, the distortion disappeared completely. The temperature dependency of the refractive index at room temperature variations was unrecognizable for the eye and found negligible.

As index matching agent ammonium thiocyanate was used. It is the salt of the ammonium cation and the thiocyanate anion, the chemical formula is NH_4SCN. The hygroscopic solid crystals are color- and odorless with a density of $1.305\,\text{g/cm}^3$. Ammonium thiocyanate is used in the manufacture of e.g. herbicides and well known to analog photographers as a stabilizing agent in photography. Due to its high solubility in water (Foote 1921, Dang et al. 2009) it serves well to change the refractive index of water from 1.33 to 1.492 without huge changes of the viscosity. The mixing ratio of ammonium thiocyanate per distilled water (weight proportion) for the index matched fluid was determined to be 1.58 at a room temperature of 25°C.
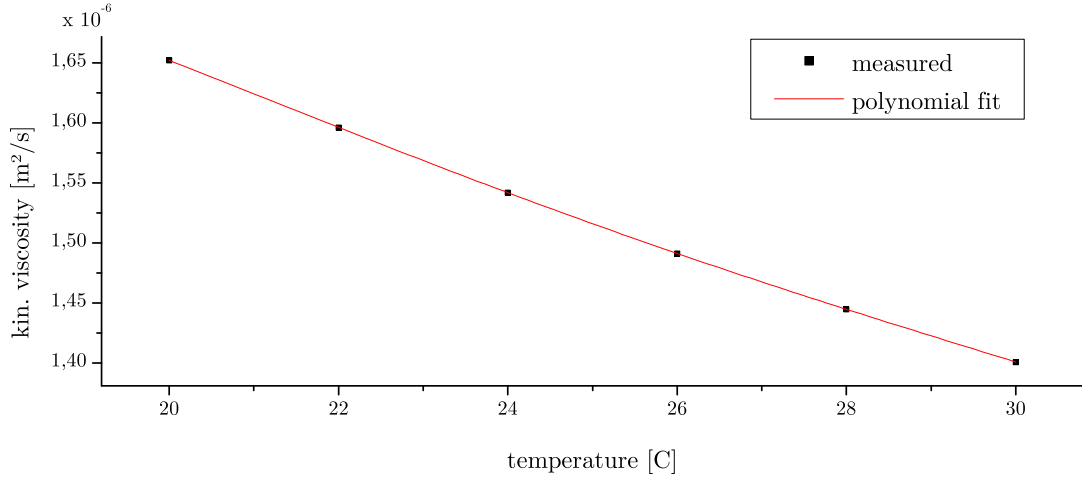
Figure 22: The kinematic viscosity of the refractive index matched fluid.

4.2.2 Viscosity of the matched fluid

As the addition of ammonium thiocyanate increases the viscosity of distilled water, the kinematic viscosity of the index matched fluid was determined by means of a *Schott* Cannon-Fenske capillary viscometer. For temperatures ranging from 20 to 30°C the measured values of the kinematic viscosity of the index matched fluid can be very well fitted by the polynomial

$$\nu_{matched} = 4.5 \times 10^{-7} + 2.7 \times 10^{-7}\,T - 1.8 \times 10^{-8}\,T^2 + 4.9 \times 10^{-10}\,T^3 - 4.9 \times 10^{-12}\,T^4\,[\text{m}^2/\text{s}] \quad (27)$$

as plotted in fig. 22. The error bars are too small to be seen on this scale. Subsequent verification of the viscosity after intensive measurement campaigns with the same fluid exhibited only minor changes.

4.3 Glitter and seeding particles

For visual observations, still photographs and video recordings polyester glitter from *Sigmund Lindner GmbH* was used. Glitter made of aluminum might have scratched the plexiglas severely. The smallest available particles with $0.05 \times 0.05 \times 0.012$ mm brought the best results concerning conspicuity of the observed patterns. Polyester glitter with dimensions $0.075 \times 0.075 \times 0.012$ mm, $0.05 \times 0.1 \times 0.012$ mm and $0.1 \times 0.2 \times 0.012$ mm were also tried but would not increase the visibility and tended to get stuck in the gap between actuator and torus wall and block the actuator. About 10 g of $0.05 \times 0.05 \times 0.012$ mm admixture of glitter to the fluid was found to be the optimum between high visibility and the least probability for the actuator to get stuck.

For PIV and LDV measurements silver-coated hollow glass spheres (S-HGS-10, mean diameter $10\,\mu$m, $\rho = 1.4\,[\text{g/cm}^3]$, *Dantec Dynamics*) were the stringent choice as seeding particles, since polyamide seeding particles or hollow glass spheres, both having a refractive index close to 1.5, would not be visible in the index matched fluid used (see 4.2.1).

4.4 Actuator

4.4.1 Sphere

The simplest way to drive the flow in the torus via a magnet from outside was by using a ferromagnetic stainless chromium steel sphere (AISI 52100, 100Cr6, 1.3505, *Spherotech GmbH*) as an actuator. To permit rolling motion of the sphere, the diameter of the tube $d = 30.3\,\text{mm}$ was chosen slightly larger than the diameter of the sphere $d_s = 30\,\text{mm}$, leaving a small sickle-shaped gap of max. $0.3\,\text{mm}$ at the upper half between torus wall and sphere. The total area of the gap was $A_{gap} = 14.2\,\text{mm}^2$. As the ammonium thiocyanate made the index matched fluid very oxidizing, the sphere had to be nickel coated, otherwise the sphere was severely corroded within a few days of use. The thickness of the coating ($\sim 5\mu\text{m}$) was negligible.

Through the gap between sphere and tube wall a small leak flow would arise. When the fluid in the torus has reached constant velocity after spin up from rest the sphere just has to balance the minor friction losses in the tube. According to the correlations provided in e.g. table 1 the pressure loss for the full torus length is expected to be in the range of $100\,\text{Pa}$ at a Reynolds number of $10\,000$. As $A_{gap}/A_{tube} = 0.0196$ simple considerations (under the simplifying assumption of uniform velocity over the cross section and the sphere moving without rolling motion) suggest a leak flow of $< 1\%$ of the mean mass flux through the tube.

It is very important to know the exact mass flux (or bulk velocity) to determine the Reynolds number. The rolling motion of the sphere and the boundary effects within the sickle shaped gap are making an exact computation of the leak flow difficult. Still the actual mean velocity and hence Reynolds number in the torus must be slightly lower than the one based on the revolution of the sphere and rotating arm respectively. Not only for this reason but also to reduce the leak flow as far as possible further designs of actuators were tested as described in the next section. Furthermore, the actual flow rate and hence the leakage was determined by means of PIV measurements (see 5.2) and pressure loss measurements (see 5.6). In anticipation of the results it can be said that, by measurements, the actual mean velocity of the flow was found to be 3% less than the velocity of the sphere.

4.4.2 Plunger with sphere

The rolling motion of the sphere induces disturbances into the flow, possibly changing the flow fundamentally. To avoid interaction of the flow with the rolling motion of the sphere, minimize the gap between actuator and torus wall and hence the leak flow, and also to enable better comparability with numerical simulations, two kinds of specially designed plungers were tested and used. The first plunger (P1) was machined in form of a slightly modified cylindrical block with a diameter of $30.1\,\text{mm}$. The total area of the gap was reduced to $9.49\,\text{mm}^2$ or 1.3% of the tubes cross section hence. Figure 23 provides a sketch of the plunger 1 made of polyoxymethylene (POM). POM is an engineering thermoplastic used in precision parts, exhibiting high rigidity and stiffness, dimensional stability, low water absorption, excellent resistance to chemicals and sliding friction properties.

A bore of $20\,\text{mm}$ diameter was drilled into that plunger, providing space for a nickel coated
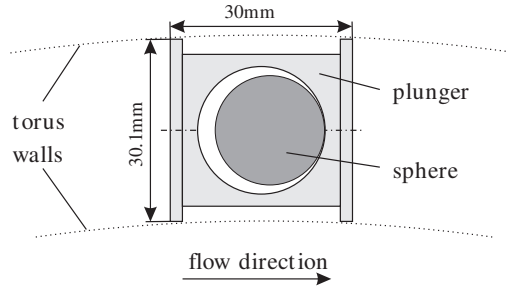
Figure 23: Sketch of the first type of plunger within the torus. A small sphere of $d_s = 18$mm placed inside the plunger is used as object of magnetic attraction to move it. Only the translatory moving walls of the plunger instead of the rolling motion of the sphere would interact with the flow in the torus.
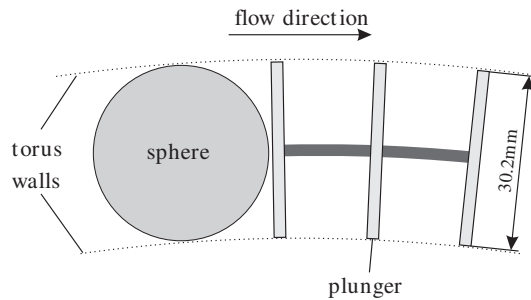
Figure 24: Sketch of the second type of plunger within the torus. A sphere of $d_s = 30$mm is used as object of magnetic attraction to push and move a plunger consisting of 3 thin circular plates (POM). The plates are incorporated by a small bracket bent to the radius of the torus.

steel sphere with 18 mm diameter. This steel sphere was also controlled by the magnet from outside, but its rolling motion would not influence the flow in the torus. As the plunger was cylindrical, its shape did not perfectly match the slightly curved torus. Due to the lubrication of the fluid between the two solid surfaces of tube and plunger, the plunger would slide through the tube very well without excessive stresses or seizures at the wall. Only very mild wear, mostly originating from the tracer particles in the fluid, was the consequence.

A custom made plunger accounting for the curvature of the tube, using a computer numerically controlled machine for fabrication, could further improve the fit of the plunger to the torus. Since such a CNC–machine was not available at our workshop, an equivalent effect was accomplished by using a design of a plunger as shown in fig. 24 (P2). 3 thin circular plates (thickness 1 mm, cross-sectional diameter 30.2 mm) made of POM were jointed by a small bracket which was bent to the radius of the torus. The bracket was placed in the lower quarter of the circular plates to achieve a low lying center of gravity. The total area of the gap was reduced to 4.75 mm^2 or less than 0.7% of the tubes cross section hence. The sphere with $d_s = 30$ mm (see 4.4.1) was used to move the plunger.

This design promised to be the tightest solution, i.e. the solution with the least leak flow. With pure water it worked well. Unfortunately, the addition of tracer particles prevented this solution, as the tracer particles would get stuck between actuator and torus wall after one or

two turns and hence block the actuator.

As the investigation of the influence of the design type of the actuator on the flow field brought no substantial differences (see sec. 5.2.1) between the sphere-only solution and plunger design 1, only the sphere was used for the measurements.

4.5 Magnet

A flat pot magnet with threaded stem to mount it onto the rotating boom was used. According to manufacturers information the pot magnet had approx. 216 N (equivalent to 22 kg bearing capacity) adhesive force perpendicular to the surface to which the magnet should stick. However, this is only a theoretical maximum value, which can only be obtained under direct contact between the magnet and the object. The actual adhesive force decreases quickly with increasing distance and is also influenced by the alloy of the object of magnetic attraction. Since the distance between magnet and sphere in the setup is 5 mm (see fig.19), the actual adhesive force imposed on the sphere is about 0.49 to 0.98 N (0.05 to 0.1 kg). This was found sufficient to control the sphere in the liquid-filled torus. Only in the case of very fast or jerky acceleration or deceleration the sphere would not follow the magnet.

4.6 Setup for 3D-PIV with a prism

Figure 25 provides a sketch of the setup which was used for stereoscopic PIV, showing the arrangement of plexiglass disks, light sheet and cameras. As already mentioned in sec. 3.2.3, two cameras in a 45°-degree viewing angle were used for 3D–PIV measurements.
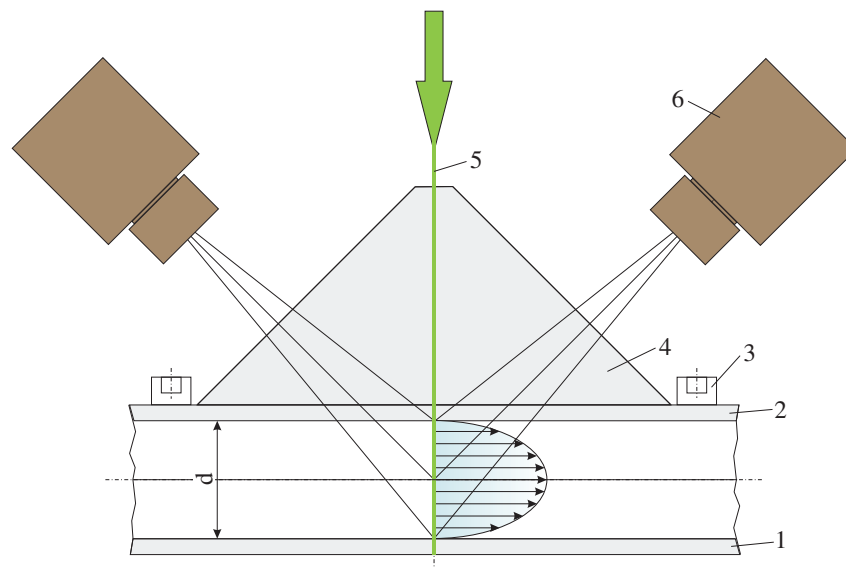
Figure 25: Sketch (side view) of the stereoscopic PIV system. To reduce optical reflections, a prism is placed on the upper plexiglas disk of the torus. 1 lower plexiglass disk, 2 upper plexiglass disk, 3 screws, 4 prism, 5 light sheet, 6 cameras. Between 2 and 4 a few drops of glycerine were used to enable seamless contact. Drawing not to scale.

An image distortion which results from the 45 degree viewing angle is that parallel lines become non-parallel in the calibration image (van Doorne & Westerweel 2007). This has to be adjusted by the use of a mapping function as described in sec. 3.2.3. Furthermore, from the 45°-degree viewing angle the light would be refracted at the wall of the plexiglass plate, which would reduce the effective viewing angle of the cameras and additionally degrade the image quality. Hence, on one side of the two plexiglass plates a prism, also made of plexiglass, was attached. The prism acts as a triangular window for the two cameras, so that they 'look' at a surface perpendicular to their viewing direction.

4.7 Calibration target

The calibration target, needed for the calibration of the 3D-PIV measurements, was a custom made (by *Die Signmaker GmbH*, Göttingen), 5 mm spaced lattice of black dots with a diameter of 1 mm printed on both sides of a 1.5 mm plexi-glass plate as shown in fig. 26. The plate had a cross-sectional diameter of 30 mm, i.e. slightly less than the diameter of the tube. The plate was kept in position (congruent with the light sheet of the laser) for the calibration procedure by a tiny locking screw drilled into the torus wall. Calibration was made by means of a software-based process employing one calibration image each from every camera (see sec. 3.2.3). After the calibration images were shot the screw and hence also the plate could be released. The experimental setup was too sensitive to be disassembled after calibration, as dismantling and repeated assembly would have caused small displacements and hence spoiled the calibration. So the calibration plate was just left in the torus and went with the flow. After a few turns of the actuator the calibration plate would then be located in the perturbed zone in front of the actuator (see sec. 5.2.1), not perturbing or changing the flow additionally to the actuator.

Figure 26: Front side of the calibration target. On the back side the same pattern was printed, though shifted such that one point on the front side would be in the center of four points on the backside. The square, printed on one side only, was used to enable orientation of the experimenter, since otherwise a clear identification and allocation of the respective sides of the target on the calibration images would not be possible.
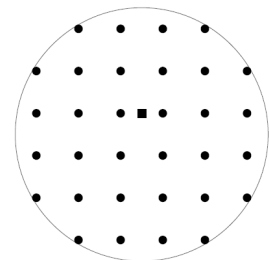
A major disadvantage of the custom made calibration target was its relatively low precision. As the lattice of black dots was *printed* on both sides the accuracy achievable ($\pm 0.05 - 0.1$ mm) is about a magnitude lower compared to calibration targets which are produced by means of CNC-machines. Furthermore, the printed shapes of the dots are not as clearly contoured and sharp-cut, but tend to frazzle at the borders.

The problem arising from dimensional deviations within the lattice of black dots is that during the calibration procedure the software 'assumes' the lattice to be in fact perfectly aligned and that deviations of the lattice in the calibration image come from *optical* distortions. An actual deviation of the lattice is hence corrupting the whole process of calibration and causes severe impact on all following steps. Future investigations should, therefore, invest more thought into

an improved calibration target and an enhanced calibration procedure.

4.8 Automatization

In the first, non-automated setup, the velocity and hence the Reynolds number was measured manually and only once per revolution by using the relation $U = \pi D / \Delta t$, where Δt was determined once per revolution by means of a revolution counter consisting of a reed switch connected to a stopwatch. This yielded a relatively large error δU due to the inaccuracy in determining Δt. It also turned out that the motor did not keep the speed precisely and therefore the revolution time sometimes deviated with up to $\approx 0.3\,\mathrm{s}$ per turn.

To increase usability and operability of the setup and to reduce the error due to rotation rate fluctuations of the motor the experimental facility was fully automated after the first successful test runs. A combination of a program written and compiled with *LabView* and a system consisting of controller unit (LSC 30/2, 4-Q-DC, *maxon motor ag*), USB data acquisition card (*National Instruments* 6008) and direct current motor (RE 25, *maxon motor ag*) with speedometer (DCT 22, *maxon motor ag*) and planetary gear (GP 32, *maxon motor ag*) was used to automatically determine the Reynolds number (Schwegel 2012). I.e., the *LabView* program contained the functional relationship between viscosity, temperature and the geometrical data based on which the required speed was calculated and implemented. If needed, the program can be updated with regard to these data. Optionally, an automatic mode can be used to increase or decrease the Reynolds numbers in a defined step size and at defined time steps set by the experimenter. The error due to deviations of the velocity (δU) was hence made negligible and the total error in terms of the Reynolds number halved (see sec. 4.9.1).

4.9 Sources of errors and their quantification

Two main sources of errors have to be accounted for in the current work: errors from setting up and determining the Reynolds number in the experiment and errors from measuring the flow field by means of PIV or LDV. The following detailed error analysis is an attempt to quantify and estimate these errors. Advantageously, in the present experimental setup the mean velocity – which was (then) going to be measured – was (theoretically) exactly adjustable by setting the rotation rate of the boom. I.e., the information available about the flow field prior to the evaluation of the measurements is providing a reliable orientation for the assessment of the results.

4.9.1 Reynolds number

The driving force in the experiment is solely represented by the Reynolds number, which is assigned by the given geometry, the bulk velocity and the kinematic viscosity of the fluid. As these independent variables are each afflicted with errors, it is essential to know the associated deviations. $\delta \mathrm{Re}$ can be determined by a Taylor series expansion to be

$$|\delta \mathrm{Re}| \leq |\frac{\partial \mathrm{Re}}{\partial d} \cdot \delta d| + |\frac{\partial \mathrm{Re}}{\partial U} \cdot \delta U| + |\frac{\partial \mathrm{Re}}{\partial \nu} \cdot \delta \nu| \tag{28}$$

and hence

$$|\delta\mathrm{Re}| \leq |\frac{U}{\nu} \cdot \delta d| + |\frac{d}{\nu} \cdot \delta U| + |\frac{dU}{\nu^2} \cdot \delta\nu| \qquad (29)$$

The manufacturing tolerance of the pipe dimensions was $\pm 0.03\,\mathrm{mm}$ for the diameter d, resulting in a relatively small contribution $(U/\nu)\delta d$ to the deviation of the Reynolds number. As already mentioned in sec. 4.8, in the first, non-automated setup, the velocity was measured manually and only once per revolution by using the relation $U = \pi D/\Delta t$. This yielded a relatively large error δU due to the inaccuracy in determining Δt. The influence of the manufacturing tolerance of the torus diameter ($D = 614 \pm 0.1\,\mathrm{mm}$) on the velocity was negligible. The subsequent automatization practically eliminated the inaccuracy in determining Δt, δU can hence be treated as negligible.

By far the largest contribution comes from the determination of the kinematic viscosity. The correlation for the viscosity (27) was measured with an accuracy of $\pm 1\%$ full scale range specified by the manufacturer (see sec. 4.2.2)). The systematic error $\delta\nu_s$ is $\nu/100$ hence. The temperature T is measured at two different locations (see 4.1) during the experiments. The mean value of both locations is used to determine the temperature. The accuracy is specified to be $\delta T = \pm 0.1$. The absolute error due to the viscosity yields $\delta\nu = |\delta\nu_s| + |\frac{\partial\nu}{\partial T} \cdot \delta T|$ hence.

According to (29) and for a temperature of $23°\mathrm{C}$ and a Reynolds number of 5000 (i.e. a velocity of $0.31\,\mathrm{m/s}$) this yields an absolute deviation of the Reynolds number $\delta\mathrm{Re} = \pm 65$ or $\pm 1.3\%$. Strictly speaking, this is true only for the actuator. I.e., if there was no leak flow at all, the Reynolds number could be specified with $\pm 1.3\%$. To account for the (measured) leak flow of 3% (see sec. 4.4.1), which is additionally afflicted with measurement uncertainty, the total deviation of the Reynolds number in the experiment is estimated to be $\delta\mathrm{Re} = \pm 2\%$.

4.9.2 Measurements

Since LDV and PIV are nonintrusive measurement techniques, the prospect of obtaining accurate results is very good. Still a big amount of various errors is part of these in details very sophisticated measurement techniques. For LDV the correct positioning of the measurement volume is essential and one of the major error sources. The statistical error of the LDV measurements depends greatly on the number of signals over which is averaged. For 3D-PIV major error sources are the so called correlation-noise, bias and peak-locking, errors in the mapping from the image plane to the measurement plane which can lead to a mismatch (misregistration) of the two dewarped vector fields (i.e. errors in the 2D mapping function which is derived from the calibration images or result from a misalignment of the laser light sheet and the calibration plane), the signal-to-noise ratio, the fraction of spurious vectors, the spatial resolution, and the temporal resolutions of the measurements (van Doorne & Westerweel 2007).

There is sufficient literature available (Goldstein 1996, Raffel et al. 2007, Tropea et al. 2007) dealing with all aspects of measurement accuracy and error sources. For both techniques, LDV and PIV, the total error can be reliably assumed to be less than 1%, i.e. the error lies within the range of the symbols used in the velocity profiles in the figures.

The best way to check and verify that no major errors have slipped in is by comparing the

results from PIV measurements with results from LDV measurements. If reliable numerical results are available a matching of the results can give further support. The first step in the evaluation of the results is hence going to be a comparison and verification of the same flow measured/computed with different techniques.

4.10 Summary table of design parameters and basic data

|		
Torus	tube diameter	$30.3\,\mathrm{mm}$
	torus diameter	$614\,\mathrm{mm}$
	curvature ratio δ	0.0493
	material	plexi-glass
Flow	fluid	water or index-matched fluid
	Re	between 1000 and 15 000
	$\delta\mathrm{Re}$	$\pm 2\%$
	$\nu_{matched}$	see eq. 27
	actuator	nickel coated steel sphere

Table 3: Overview of the relevant experimental parameters.

5 Results

In the first instance results from visual observations are presented in this chapter. Subsequently a quantitative evaluation of the experimental setup with considerations of the influence of the actuator, a comparison of velocity profiles measured by different methods and an evaluation of the cross sectional flow field is presented. Then a presentation of mean velocity profiles, especially for increasing Reynolds number, leads to investigations of the instantaneous flow field at the first instability. The large scale velocity fluctuations are described and the frequency spectrum of the velocity fluctuations is analyzed. Furthermore, the first critical Reynolds number is determined and the bifurcation scenario investigated. Considerations of the flow field at higher Reynolds number, i.e. above the second critical Reynolds number, complete the chapter.

Movies and animations of the phenomena discussed in the text are provided on the enclosed CD. They are referred to as *mov-X*, where *X* is the name of the respective movie file.


Figure 27: Reference system valid for all figures presented in the following, unless stated differently. The outside of the bend is at the left, the inside of the bend at the right of the figures cross section. *x* and *y* provide the coordinates as given in figure 6. Horizontal (velocity) profiles denominate a cut along A-A', vertical profiles along B-B'. Denomination of the characteristic areas (wall layer, core region, region 1) within the cross section are the same as in fig. 8.
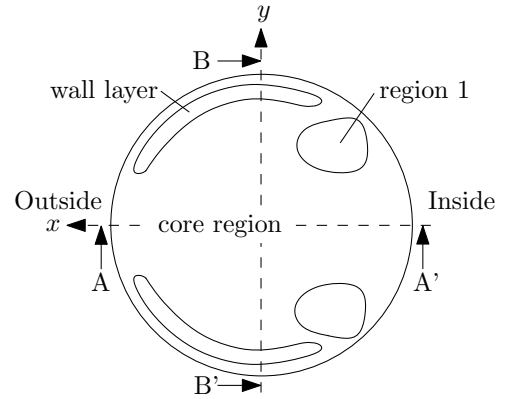
5.1 Flow visualization

By means of rather simple flow visualization techniques a lot of information about the object to be examined can be acquired. To this end the flow in the torus was seeded with glitter particles (see sec. 4.3) which reflect the light and visualize the flow field. This allowed preliminary investigations and visual identification of pertinent flow structures. The degree of conspicuity was limited, as the particles tended to get stuck in the gap between actuator and torus wall and would, hence, block the actuator. Therefore, only a limited amount of particles could be used. Even though the flow was quite well observable for a direct observer this yielded an insufficient presentability for movie recordings and especially for photography. Hence only a few examples are presented here.

At low Reynolds numbers the typical appearance of the (laminar) flow was as shown in fig. 28 (a) for Re = 3000. The lower figure (b) shows the sphere (actuator) in the middle of the frame. The upper figure (a) was shot at the moment when the sphere was exactly on the other side of the torus, i.e. for $\Delta\varphi = 180°$. The black stripe, approx. two thirds from the outside of the tube, is characteristic for the appearance of the (developed) laminar flow field. Hence the black stripe is not seen in the lower picture, where the motion of the sphere is disturbing the flow field.
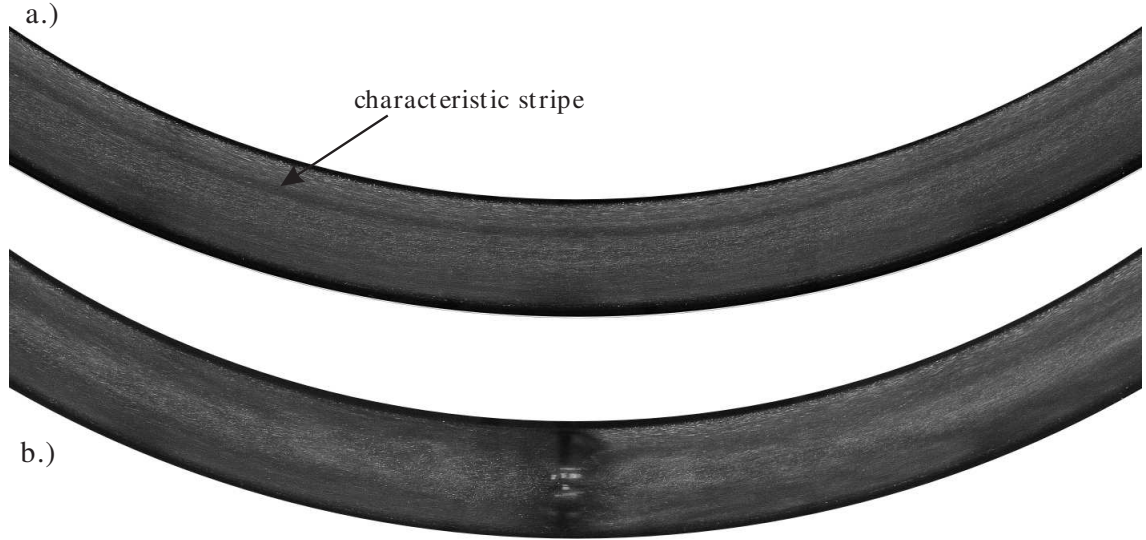
Figure 28: 2 photos of a torus-section ($\Delta\varphi \cong 68°$) from above at Re = 3000. (a) shows the characteristic laminar flow, recognizable from the black stripe approx. one third from the inner side of the tube. (b) shows the disturbed flow field in front and behind the actuator.

By observing the length of the disturbed zone in front and behind the actuator with increasing Reynolds number, a first estimate of the influence of the actuator can be acquired. As shown in fig. 29 the disturbance appeared to be always stronger in front of the actuator. For Re = 3500 the visible disturbance has a length of $\approx 12d$ or 20% of the total torus length respectively.
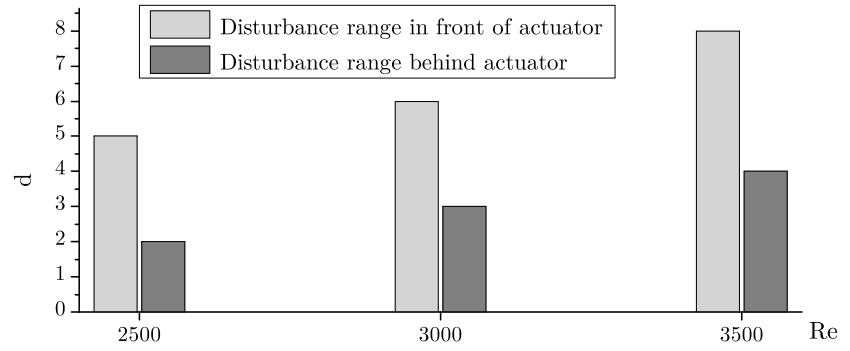
With increasing Reynolds number, at approx. Re = 4100, the black stripe which is characteristic for the laminar flow, was observed to develop an initially barely visible modulation. At approx. Re = 4200 and then very pronounced at Re = 4300 regular patterns within the flow become visible (see *mov-Re4350.1turn.bw.indeo.960x540.avi*). These patterns exhibit a wave-like modulation and seem to be more distinct in the inner half of the tube.

Fig. 30 shows a short section ($\Delta\varphi \cong 24°$) of the torus at Re = 4350 showing one full wavelength of the observed pattern. The characteristic wavelength λ is estimated to be approx. $\Delta\varphi = 11.3 - 14.1°$ ($\simeq 2 - 2.5\,d$) for Re < 4350 and is observed to start varying between $2 - 4\,d$ for Re $\gtrapprox$ 4350. The patterns move with a celerity (wave speed) c of approx. $1.13\,U$, i.e. about 10% faster than the bulk velocity. At Reynolds numbers above $\cong$ 4580 the regular modulation seems disturbed, i.e. it is sometimes periodic and sometimes irregular. For Re $\gtrapprox$ 5050 a clear distinction of single wavelengths is no longer possible.

The estimates for the wavelength λ from the still photographs and the wave speed estimates from the video recordings yield the wave frequency f according to $f = c/\lambda$. f is hence determined to be $\cong 3.2\,\mathrm{Hz}$. As the bulk velocity was $\cong 0.2\,[\mathrm{m/s}]$ this yielded a nondimensional frequency $\hat{f} = fd/U$ of $\cong 0.5$.

Summing up the main results from flow visualization, above Re $\approx$ 4100 a supercritical transition to a flow which is periodically modulated in the streamwise (axial) direction of the tube was found. The periodic pattern is almost stationary in a frame of reference moving with the actuator, exhibiting a celerity slightly above the bulk velocity of the flow weakly depending on

Figure 29: Disturbance range, expressed in diameter, in front of and behind the actuator as determined from mere visual observations. In front of the actuator the disturbance looks about twice as long.

the Reynolds number. The wavy modulation is very weak for Reynolds numbers slightly above the critical Reynolds number. With increasing Reynolds number, the modulation of the axial velocity becomes more distinct.
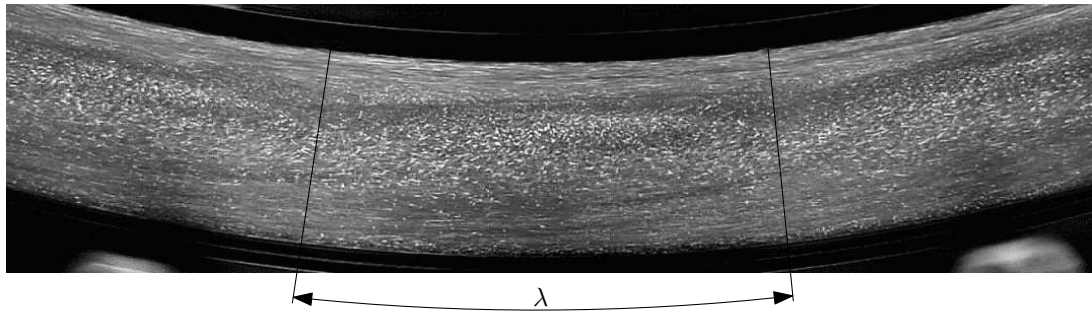
Figure 30: Still picture from a movie (see *mov-Re4350.1turn.bw.indeo.960x540.avi*) of a short section of the torus from above at Re = 4350. The camera was following the flow at the bulk velocity. The wavy modulation of the flow is difficult to recognize in the photograph, but clearly visible to a direct observer or in the motion pictures.
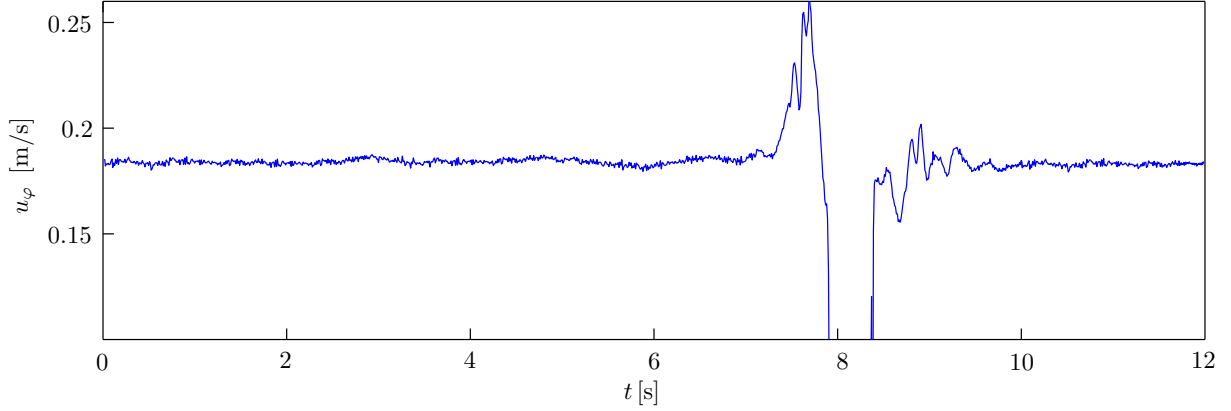
Figure 31: Time trace of the streamwise velocity at $x, y = [-0.3\,a, 0.6\,a]$ and Re $= 3600$. A typical PIV-run of $12\,\mathrm{s}$, comprising approx. one full revolution of the actuator, is displayed. At Re $= 3600$ the flow is still clearly laminar and the deviation from a straight line is due to measurement noise and possible deviations of the actuator, i.e. a slight inconstancy of the drive. The transit of the actuator through the measurement plane after $\sim 8\,\mathrm{s}$ is clear-cut.

5.2 Quantitative evaluation of the experimental setup

As considerations of the development lengths in a torus (see sec. 2.3.5) have shown that the flow can not be fully developed *within one revolution*, as a first step the 'degree of development' has to be assessed. This goes hand in hand with a quantitative evaluation of the influence of the actuator, i.e. to which extent and range the actuator disturbs the flow field in the torus. Furthermore, a comparison of results obtained with different measurement techniques and computational data is needed to assess the quality of the results and their validity.

Apart from a small deviation due to the minor leak flow past the actuator the bulk velocity and hence the mean flow rate is well known previous to every measurement as the velocity (Reynolds number) is adjusted and set by the experimenter. In return this fact can be employed to determine the amount of leak flow by comparing the mean velocity obtained from measurements with the one set before.

5.2.1 Influence of actuator

In anticipation of the results measured with PIV presented further below, fig. 31 shows the streamwise velocity u_φ at the point $x, y = [-0.3\,a, 0.6\,a]$ and Re $= 3600$ for approx. one full revolution of the actuator. As will be shown later, this point of the cross section is where the first instability is observed best (sec. 5.4.2). At Re $= 3600$ the flow is laminar and the small fluctuations of the velocity visible in fig. 31 are due to the minor noise of the PIV data and possible deviations of the actuator, i.e. a slight inconstancy of the drive. The RMS of the streamwise velocity, except for the vicinity of the actuator, is 0.78% of the mean value.

In the proximity of the actuator the flow is disturbed. In front of the actuator, about $1\,\mathrm{s}$ before it actually transits, a steep increase of the velocity can be seen. Behind the actuator the velocity is also considerably disturbed, although the deviation from the mean laminar value is
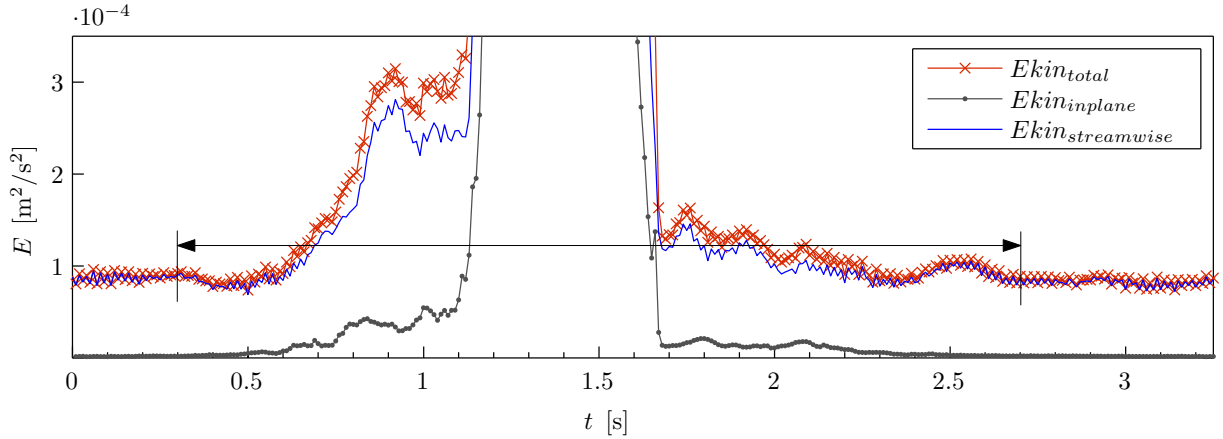
Figure 32: Transit of the actuator through the measurement plane at Re = 3600. In-plane, streamwise and total kinetic energy of the velocity fluctuations, averaged over the cross-sectional plane as a function of time.

not as large (in the monitoring point). Visual observations showed that the extent of the region of disturbed flow increases with increasing Reynolds number and has a length of $\simeq 20\%$ of the total torus length for Re = 3600.

Fig. 32 shows the kinetic energy of the velocity fluctuations of the flow, subdivided into streamwise and in-plane components and averaged over the cross-sectional plane as a function of time. I.e., $Ekin_{streamwise} = (u - \bar{u})^2$, $Ekin_{inplane} = (v - \bar{v})^2 + (w - \bar{w})^2$. Note that the kinetic energy has units of velocity squared, not energy, since the constant mass/2 has been neglected.

The figure shows the direct vicinity of the actuator, i.e. the part of a revolution when the actuator passes through the measurement plane. The area highlighted by the horizontal arrow indicates the range of the flow which is obviously disturbed by the actuator. Ahead of and behind this range the kinetic energy of the fluctuation velocity is nearly constant and very small. The total range of disturbance by the actuator is hence determined to be 2.4 s or 14.73 d respectively, which is $\simeq 23\%$ or $0.46\,\pi$ of the total torus length. The overall difference of the disturbance in front of the actuator ($\simeq 6.75\,d$) and behind the actuator ($\simeq 7.98\,d$) is noticeable but not as profound as assumed from the visual observations.

Fig. 33 shows a time trace of the streamwise velocity at the same location as fig. 31, but at Re = 4300. A very distinct and substantial periodic modulation of the streamwise velocity can be observed. In the vicinity of the actuator the modulation is considerably disturbed. The frequency of the modulation is visible already in the closer vicinity of the actuator, but the amplitude is considerably lower. In the section marked as 'used range' the amplitude of the modulation is constant within $\simeq \pm 10\%$, the flow is considered as periodic and fully developed (i.e. independent of the actuator and time-invariant in a reference system moving with the wave celerity) hence. All data used for the analysis of the flow field, the instability etc. was taken from this range.

At slightly higher Reynolds numbers a second frequency and for even higher Reynolds numbers, a more and more chaotic perturbation appears whose details will be discussed below. For
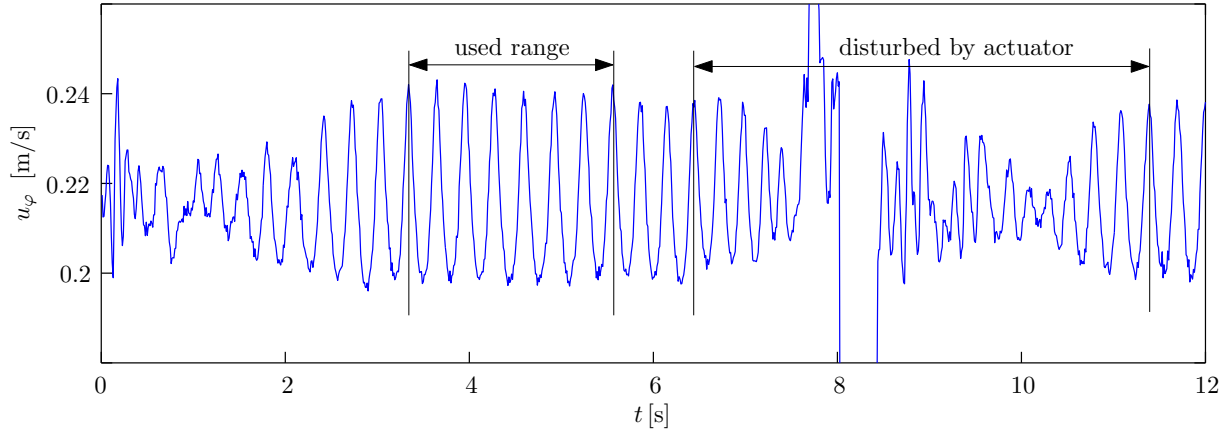
Figure 33: Time trace of the streamwise velocity at $x, y = [-0.3\,a, 0.6\,a]$ and Re $= 4300$. Due to the higher velocity more than one full revolution of the actuator is captured. The streamwise velocity is periodically modulated. In the vicinity of the actuator the modulation is considerably disturbed. In the section marked as 'used range' the flow is considered as (sufficiently) fully developed, only this section has been employed for the analysis of the instability and the flow field hence. The duration of $2.25\,\mathrm{s}$ of the 'used range' corresponds to $0.5\,\mathrm{m}$ or $\simeq 26\%$ of one full revolution.

the evaluation of the influence of the actuator and the assessment of the degree of development of the flow field fig. 34 shows an example of a time trace at Re $= 4700$. A modulation of the flow is still obvious, but neither the frequency nor the amplitudes have a constant value. A clear cut delimitation of the area which is perturbed by the actuator is not possible anymore. By extrapolating the results obtained at lower Reynolds numbers for the range perturbed by the actuator it seems acceptable to consider a range of $\simeq 15\%$ of one torus length directly opposing the actuator as 'fully developed' flow field for $4500 \leq$ Re ≤ 6000. I.e., if the actuator is considered to be located at the toroidal angle $\varphi = 0$ only the range $[0.85\pi, 1.15\pi]$ is examined. The definition of 'fully developed' in the sense of a time invariant flow field when moving with the wave celerity is obviously inconsistent though in this case.
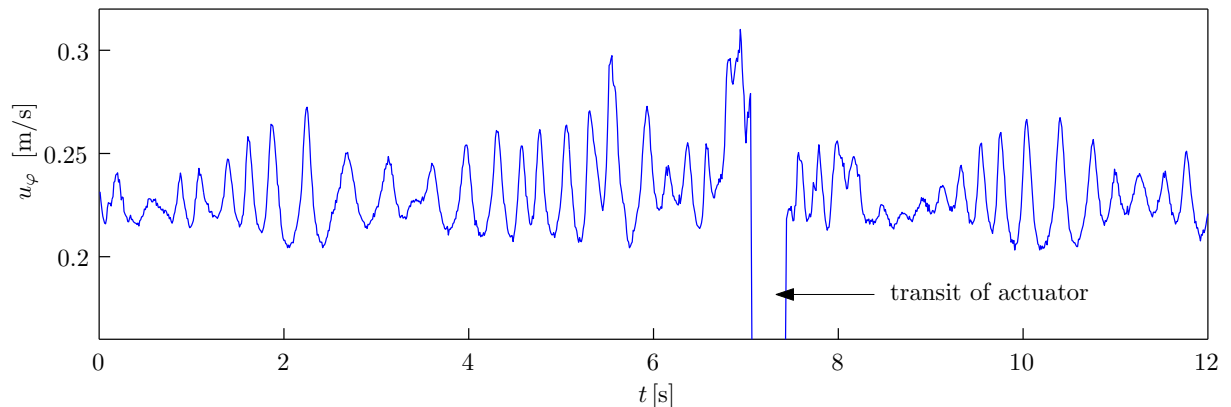
Figure 34: Time trace of the streamwise velocity at $x, y = [-0.3\,a, 0.6\,a]$ and Re $= 4700$. A clear cut distinction between the 'fully developed' flow field and the area disturbed by the actuator is no longer possible.

In conclusion, within a certain distance up and downstream of the actuator the flow field is affected by the rolling motion of the sphere. In sufficient distance to the actuator the flow seems not influenced by the actuator though and the flow field can be considered as a fully developed pipe flow.

5.2.2 Comparison of velocity profiles

To verify the acquired data and to make sure that no major errors have slipped in, a comparison of results obtained from PIV measurements, LDV measurements and numerical computations by Schwab (2011) is presented in fig. 35. The figure shows axial (streamwise) velocity profiles at Re = 3000 along the horizontal axis of the cross section. The overall picture is as expected: the position of the maximum axial velocity and therewith the whole profile is severely skewed to the outer wall. All curves yield a maximum at about $1.6\,U$. The gently s-shaped 'back' of the slope is reproduced slightly differently by every source, but the agreement is very good. Excellent qualitative agreement is also found with e.g. Hüttl et al. (1999), although no quantitative comparison is possible as these authors presented data for different curvature ratios and Reynolds numbers.
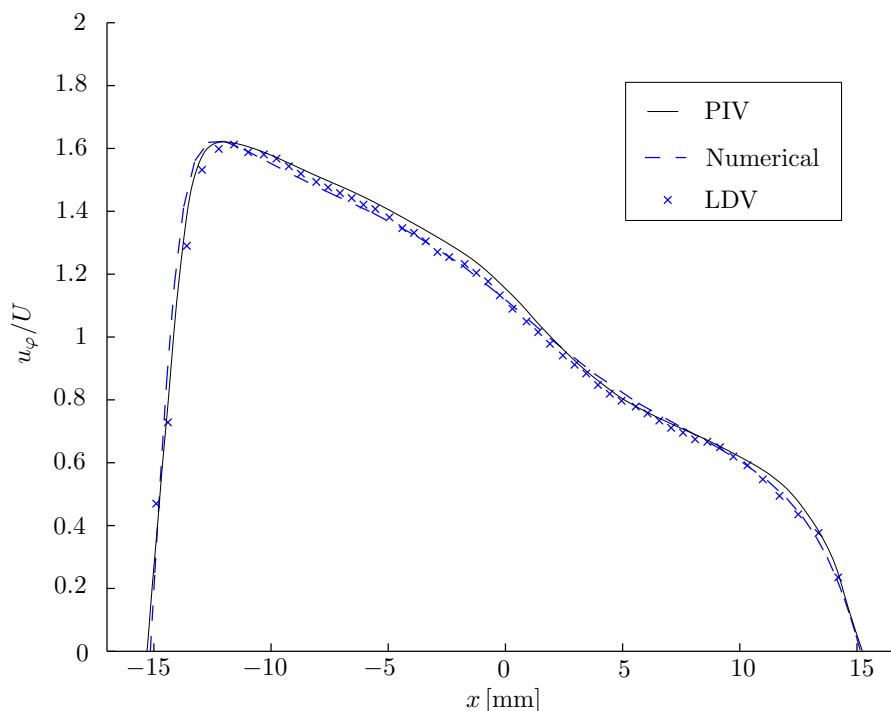
Figure 35: Horizontal profiles of the streamwise velocity at Re = 3000 along the horizontal axis of the cross section. The curves were obtained from 3D-PIV, LDV and numerical calculations by Schwab (2011). For PIV the RMS of the measurement data is less than 1%, for LDV the RMS is $\cong 5\%$.
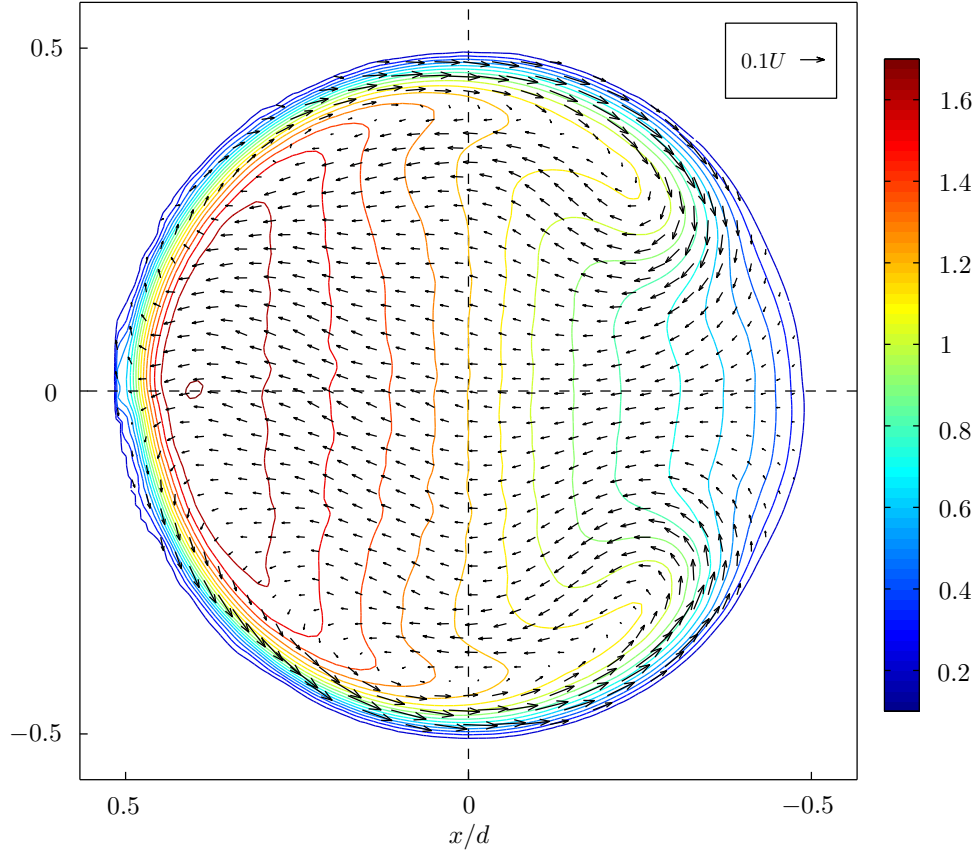
Figure 36: Streamwise (color contours) and in-plane (vector field) velocities at Re = 3600, both normalized with the bulk velocity. To eliminate measurement noise, the flow field is an average of 400 PIV-images. In the left half of the cross section the vectors of the in-plane velocity field are not perfectly symmetric in regards to the horizontal centerline.

5.2.3 Evaluation of the entire cross-sectional flow field

Looking at results obtained from 3D-PIV measurements of the entire cross-sectional flow field as shown in fig. 36 it is obvious that the whole flow field is well resolved. The contour lines of the streamwise velocity show the steep velocity gradient along the horizontal axis near the outer wall and a weaker gradient towards the inner wall. Only the very outer contour lines show some wiggles which are caused by reflections at the pipe wall, which make near wall measurements difficult.

Even though the in-plane velocities are about a magnitude smaller than the streamwise velocities, the vector field indicating the secondary flow is clearly visible. The secondary flow field exhibits a two-vortex structure with velocity maxima close to the upper and lower walls. The secondary flow directed inwards arises in rather thin regions close to the upper and lower pipe wall, while the flow directed toward the outside of the torus is quite evenly distributed over the rest of the cross section. Comparison to velocity distributions provided in the literature (see also fig. 7 and fig. 13) verify high accordance.

Although the flow is symmetric in respect to the horizontal centerline, especially in the mid-
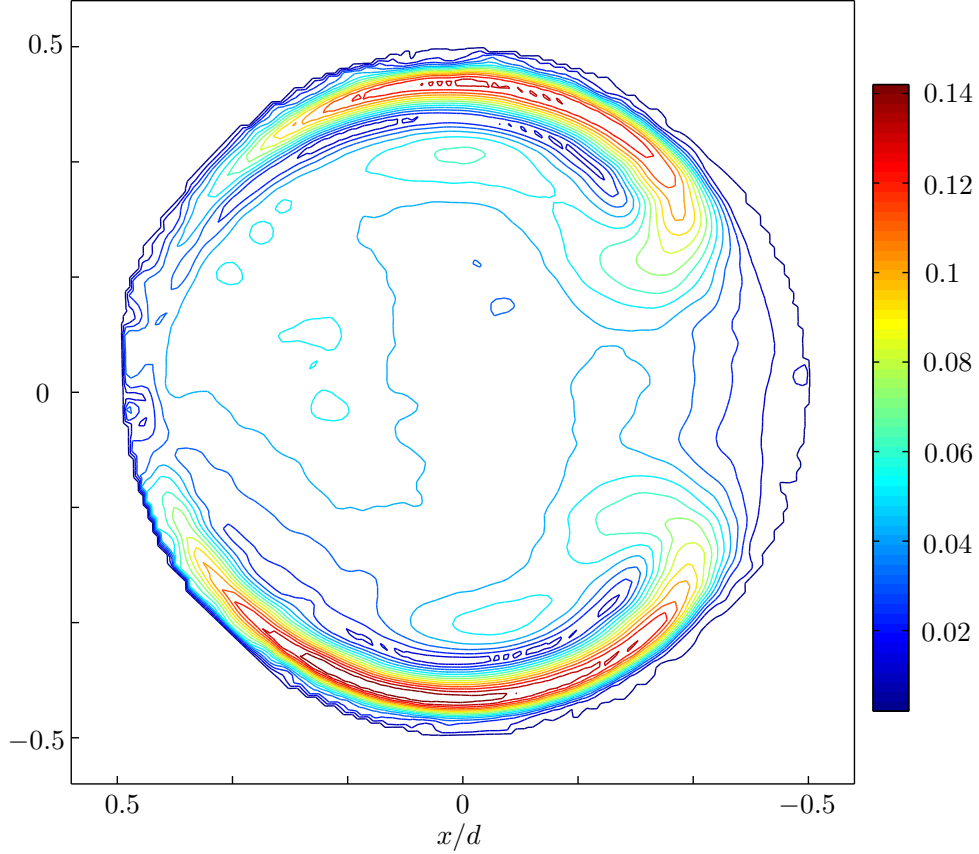
Figure 37: Color coded contours of the in-plane velocity ($\sqrt{u_r^2 + u_\alpha^2}$) at Re = 3600, normalized with the bulk velocity. The flow field is an average of 400 PIV-images. In the left half of the cross section the in-plane velocity field is not perfectly symmetric in regards to the horizontal centerline.

dle and lower left of the figure a distinct deviation from perfect symmetry is visible. A slight misalignment and offset of the vector field towards the upper pipe wall is apparent. This observation is further supported by a closer look at the contours of the in-plane velocity $\sqrt{u_r^2 + u_\alpha^2}$ as shown in fig. 37, where the deviation from perfect symmetry is best seen in the left part of the figure.

As can be seen in fig. 38, which is a vertical cut through the contours of the in-plane velocity in fig. 37 at a different Reynolds number, the deviation is also present in the cross stream wall layer (see fig. 8), i.e. in the area of maximum in-plane velocity. While the peak of the in-plane velocity at the left in the figure (i.e. in the upper cross stream wall layer) is $\sim 0.15\,U$, the peak at the right (i.e. in the lower cross stream wall layer) is $\sim 0.14\,U$. This implies a difference of $\simeq 7\%$, meaning that the in-plane velocity profile, which should be absolutely symmetric regarding the horizontal centerline, is skewed by $\simeq 7\%$. Note that this does *not* apply to the streamwise velocity profiles (see e.g. the vertical profiles in fig. 41).

The search for possible reasons has not brought definitive results. Two major origins of the deviation are possible. One is that the deviation is actually based on the flow field and has its source in the physical flow field. The other possibility is that the deviation is based on measurement errors, in particular an erroneous calibration.

Figure 38: Vertical profile of the in-plane velocity ($\sqrt{u_r^2 + u_\alpha^2}$) at Re = 2400, normalized with the bulk velocity. Two sharp peaks close to the borders, indicating relatively high local velocities in the cross stream wall layer, are visible. The minor deviation from symmetry in regards to the vertical midplane by $\simeq 7\%$ is presumably due to calibration or the influence of the actuator.
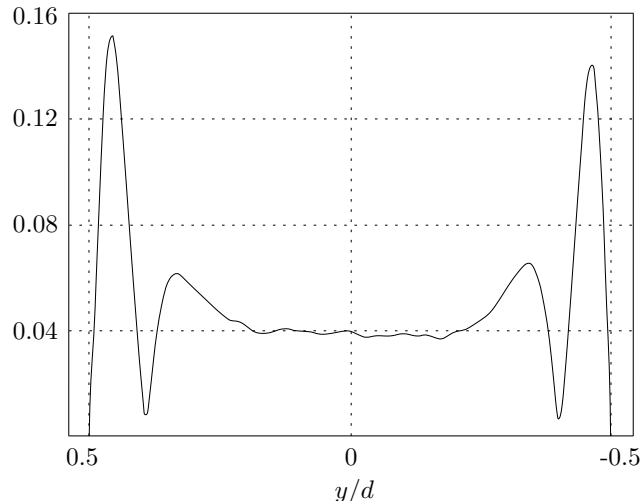
If the first was true it could still have more than one reasons, as the flow field might not be as fully developed as sec. 5.2.1 suggests. Hence the deviation would imply a flow field which is not fully developed but disturbed by the actuator. This disturbance could either result from the rolling motion and the related perturbed flow field in the vicinity of the actuator or the leak flow past the actuator. It could also be that the actuator imposes a velocity profile as boundary condition (i.e. a spherically curved profile when using a sphere or a 'block profile' when using the plug design) on the flow such that the result is the observed small deviation from symmetry. The driving flow of the actuator definitely breaks the vertical symmetry with respect to $y = 0$ in the vicinity of the actuator. It is also worth recalling that according to sec. 2.3.5 the development length needed is far out of reach.

The origin of the deviation could also be geometric imperfections of the torus, for example if the two plexiglass plates where not perfectly aligned but slightly displaced, causing a small step within the torus wall. This is, however, the least probable reason, as careful assembly and the low manufacturing tolerances given in sec. 4.1 assure a high geometrical accuracy.

A slightly faulty calibration seems also possible, especially when looking at the rather high manufacturing tolerances of the calibration target (sec. 4.7). The final judgment between non-fully developed flow field and faulty calibration would need further measurement campaigns with the stereo PIV system and a better target for calibration.

From the results presented here it can be concluded that the overall flow field is very well resolved, even for the relatively small in-plane velocities. Furthermore, the results are consistent with existing results found in the literature. Strong indication is found that the flow field can be considered as *practically* fully developed in sufficient distance of the actuator. A minor deviation from perfect horizontal symmetry in the range of up to $\simeq 7\%$ regarding the mirror-symmetric maxima of the in-plane velocities in the cross stream wall layer, presumably caused by imperfections of the calibration target or the influence of the actuator, is observed.

5.3 Velocity profiles

5.3.1 Velocity profiles of the steady base flow

As already seen in the flow field in fig. 36 and highlighted in fig. 39 as a three-dimensional view of the streamwise velocity profile, the characteristic appearance of the mean streamwise velocity field in the laminar regime is as follows:

The flow is steady and axisymmetric except with respect to the vertical midline of the cross section of the tube. The core region in the bulk of the flow is centrifugally driven toward the outer wall. Fluid with high streamwise velocity in the outer boundary is convected toward the inner wall by the cross-stream flow leading to elongated contour shapes of the streamwise velocity. With increasing Reynolds number and/or increasing curvature these wall layers – where the cross-stream flow is returned to the inner wall – become thinner and confined to a distance very close to the wall.
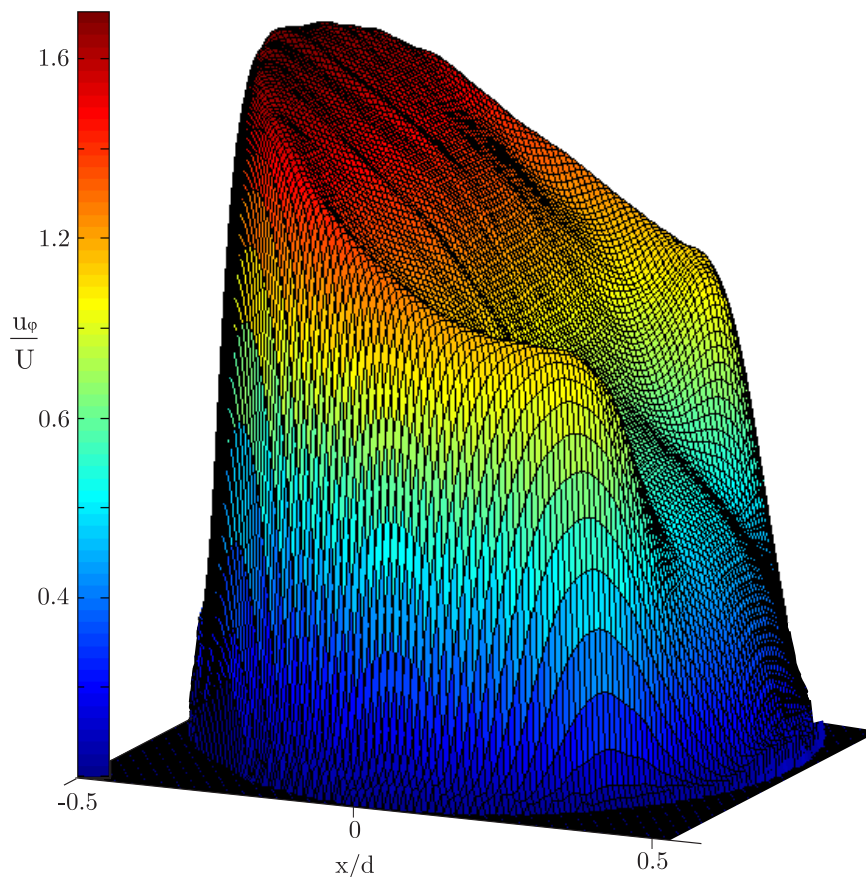
Figure 39: Three-dimensional view of the characteristic profile of the streamwise velocity at Re = 3600, time averaged over 400 PIV images. As the maximum velocity is strongly skewed toward the outer periphery and the gently s-shaped 'back' of the core region is encircled by distinctly superior elongated contour shapes ('arm rests') of the cross-stream wall layer, the appearance reminds of a padded armchair. The armchair lacks in a modest even place to rest on though.

The position of the maximum axial velocity and therewith the whole profile is severely skewed to the outer wall, causing a sharp peak about $0.24\,a$ (at Re = 2400, see fig. 41) off the outer tube wall with a maximum at about 1.6 of the mean velocity. The contour lines of the streamwise velocity hence show a steep gradient along the horizontal axis near the outer wall of order $0.67\,U/0.1\,a$ (at Re = 2400) and a substantially more snugly inclined gradient towards the inner wall. The 'back' of this snugly inclined slope along the horizontal midplane is gently wavy or s-shaped, yielding an inflection point in the inner half of the tube, about $0.5\,a$ from the tube centerline. In the upper and lower cross-stream wall layer (see fig. 8), i.e. in the regions of maximum in-plane velocity, the streamwise velocity profile develops two characteristic local maxima near the wall. These local maxima are best seen in the 3D view provided in fig. 39, showing the mean streamwise velocity profile at Re = 3600.
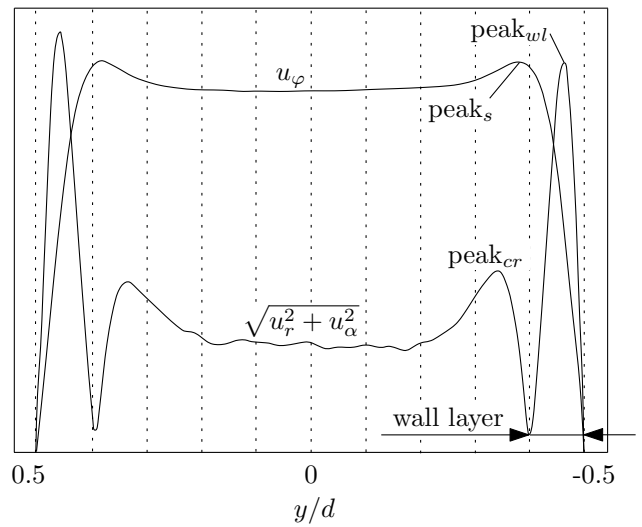
Figure 40: Superposition and comparison of vertical profiles of the streamwise (u_φ) and in-plane ($\sqrt{u_r^2 + u_\alpha^2}$) velocities at Re = 2400. Velocities not to scale.

In the 3D view the two local maxima take the appearance of distinctly superior 'arm rests', inducing a shape which reminds of an padded armchair that has no even place to sit on. These near wall regions of distinctly higher streamwise velocity match with the local maxima of the in-plane velocity as shown in fig. 38 and, color coded for the whole cross section, in fig. 37. In this figure it becomes most obvious that the in-plane velocity is relatively small and uniformly distributed over the whole cross section except for a small region near the upper and lower tube wall. Close to the inside of the bend the in-plane velocity is almost negligible.

Fig. 40 compares the streamwise and in-plane velocities by superposition. The cross stream wall layer is distinctly confined to a distance of $0.2\,a$ off the wall for $\sqrt{u_r^2 + u_\alpha^2}$. The in-plane velocity exhibits two major maxima: one peak in the cross stream *wall layer* (peak_{wl}) and one smaller peak practically at the outer border of the high speed *core region* (peak_{cr}). The peak of the *streamwise* velocity, peak_s, falls quite centric into the space between peak_{cr} and peak_{wl} and matches well with the local minimum of the in-plane velocities. I.e. the cross stream wall layer is restricted to the area $0.2\,a$ off the wall, confined by the local minimum of the in-plane velocity and by the local maximum of the streamwise velocity.
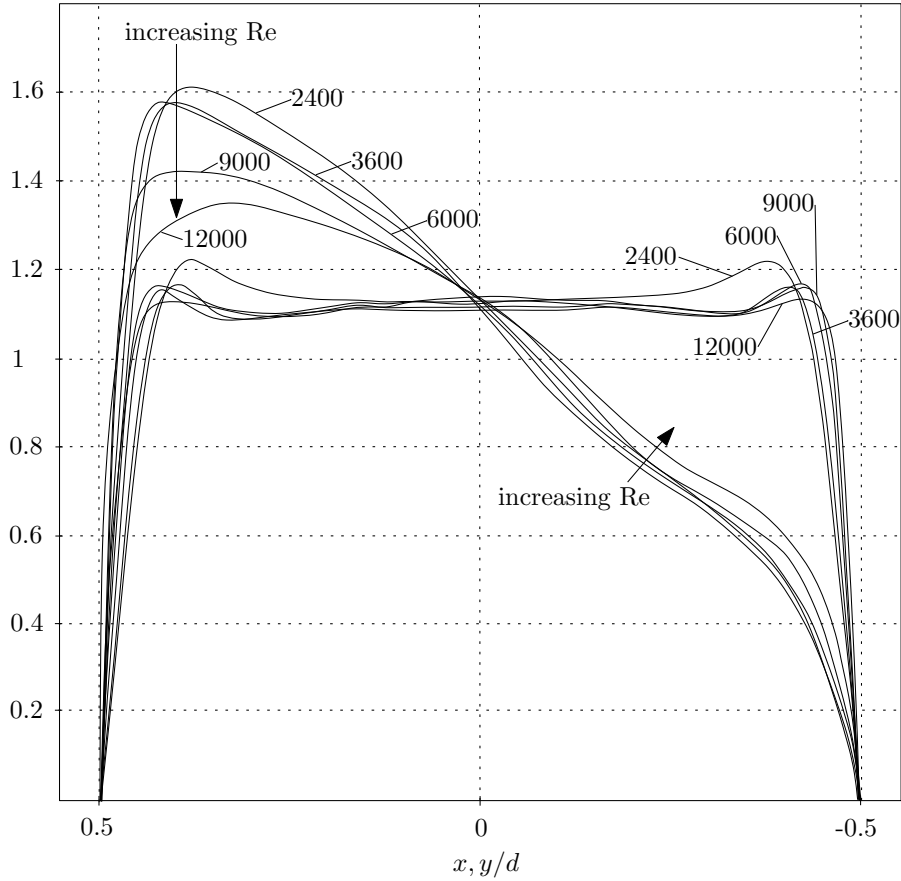
Figure 41: Horizontal and vertical profiles of the streamwise velocity for different Reynolds numbers. Profiles at Re = 2400, 3600 and 6000 were obtained by averaging over 400 images, profiles at Re = 9000 and 12000 by averaging over 200 images.

5.3.2 Mean velocity profiles for increasing Reynolds number

The dependence of the mean streamwise velocity on the Reynolds number is presented in figure 41. For Re = 2400 the horizontal and vertical profile exhibits the highest maximum velocity of all Reynolds numbers shown. The maximum of the horizontal profile is $\simeq 0.24\,a$ off the outer wall at just about $1.6\,U$ and the two local maxima of the vertical profile are also $\simeq 0.24\,a$ off the wall at $\sim 1.2\,U$. For Re = 3600 both the horizontal and vertical profile show slightly decreased maxima just below $1.6\,U$ and $1.2\,U$ respectively. Simultaneously the distance from the outer pipe wall has decreased for the horizontal profile and is now $\simeq 0.16\,a$ off the outer wall, while for the vertical profile the location of the peak has shifted only marginally towards the wall and is found $\simeq 0.22\,a$ off the wall. As will be shown in the next chapter, Re = 3600 is still in the steady laminar regime.

Between the profile at Re = 3600 and the one at Re = 6000 almost no difference is seen, except that the peak's distance to the pipe wall has *in*creased again in the horizontal profile. Neither the vertical nor the horizontal profile exhibit any substantial changes in the overall appearance nor in the heights of their peaks. Only a very close look reveals that the peak of the horizontal profile is now $\simeq 0.2\,a$ off the wall, i.e. a little more far away than at Re = 3600,
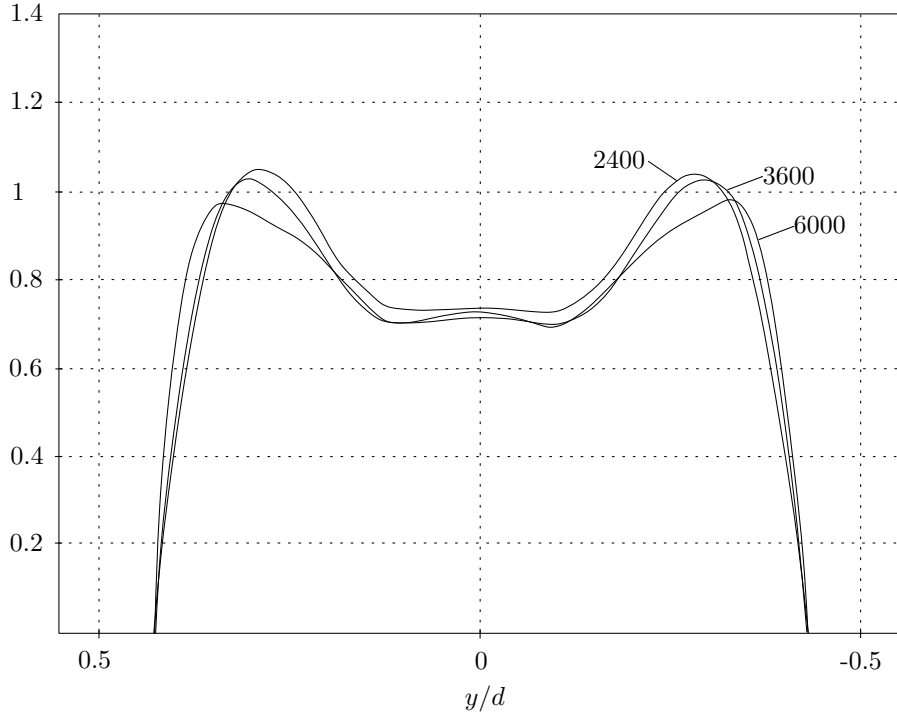
Figure 42: Vertical profiles of the streamwise velocity as in fig. 41, but at $x = -0.5\,a$, i.e. $0.5\,a$ from the vertical midplane towards the inside of the bend. For this cut the difference between the profile at $\mathrm{Re} = 3600$ and the one at $\mathrm{Re} = 6000$ is more distinct.

while the peak of the vertical profile has come closer to the wall ($\simeq 0.16\,a$ off the wall). This marginal change in the appearance between $\mathrm{Re} = 3600$ and $\mathrm{Re} = 6000$ is even more amazing, as $\mathrm{Re} = 6000$ is already clearly in the transitional regime and the instantaneous flow field intensely time dependent (see next chapter). The *averaged* flow field seems to be unaffected though.

At a further increase of the Reynolds number to $\mathrm{Re} = 9000$, and then again to $\mathrm{Re} = 12000$, a far more distinct change of the overall appearance is realized, at least for the horizontal profile. The peak is considerably lowered ($\simeq 1.42\,U$ at $\mathrm{Re} = 9000$ and $\simeq 1.35\,U$ at $\mathrm{Re} = 12000$), its sharpness decreased and its distance to the pipe wall increased ($\simeq 0.36\,a$ at $\mathrm{Re} = 12000$). The vertical profiles exhibit only minor changes again, in particular a minor decrease of the peaks, which also become less sharply shaped. The 'arm rests' hence 'flatten out' and the whole profile, which was sharply skewed towards the outer pipe wall for lower Reynolds numbers, is becoming more uniformly distributed over the pipe cross section somewhere above $\mathrm{Re} = 6000$. The exact Reynolds number or – since it seems to be a gradual change – the range of Reynolds numbers at which this process starts has not been investigated more closely in this work.

71

5.4 Transition, first instability

5.4.1 Instantaneous flow field

In contrast to the mean velocity profiles, where almost no difference is found between $Re = 3600$ and $Re = 6000$, according to the visual observations the instantaneous flow field is already known to become time dependent. According to the visual observations, time dependency is expected above $Re_{crit} \simeq 4000$ (see sec. 5.4.3 concerning the exact determination of Re_{crit}).

Fig. 33 and in particular fig. 43 shows the temporal oscillation, which starts to appear above the critical Reynolds number, for $Re = 4300$ at $x, y = [-0.3\, a, 0.6\, a]$. At this Reynolds number u_φ is oscillating with approx. $\pm 10\%$ compared to $\bar{u}_\varphi$. The modulation has a frequency of $3.25\,\text{Hz}$ or $\hat{f} = 0.45$ respectively (at $Re = 4300$). The in-plane velocities u_r and u_α exhibit the same frequency at a different amplitude and distinctly shifted in phase. Interestingly, the frequency of the modulation is not observed to change for $Re_{crit} \leq Re \leq 4500$. This means in return, that $\hat{f}$ decreases with increasing Reynolds number. For a more detailed analysis of the frequencies see sec. 5.4.3.

The first instability, establishing above Re_{crit}, is hence mainly characterized by a regular periodical modulation of the instantaneous flow field. Fig. 44 illustrates the incipient modulation of the streamwise velocity by means of a sequential arrangement of the contours of the instantaneous streamwise velocity during one wavelength λ at $Re = 4300$. As the in-plane velocities show comparatively negligible modulation which is practically unrecognizable on the scale of the streamwise velocity, the figure displays only contour lines for u_φ. $Re = 4300$ is chosen for illustration as the modulation is already well established at this Reynolds number.
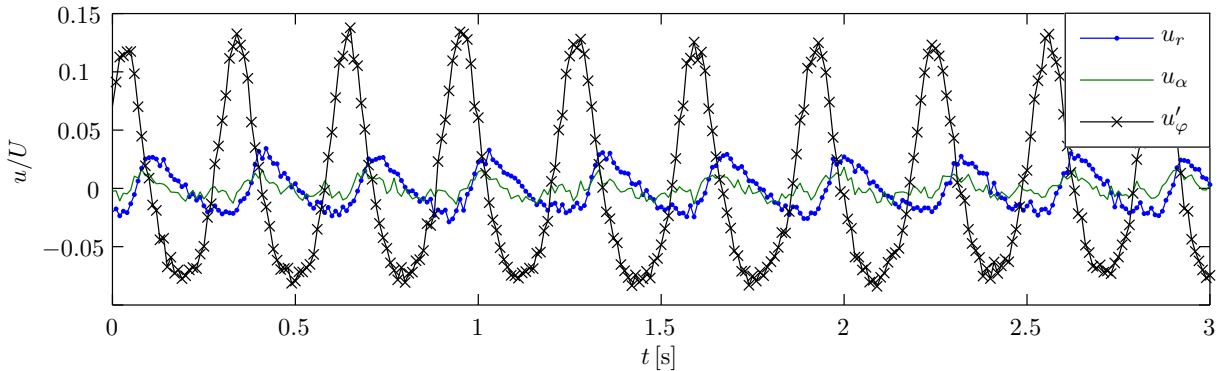
Figure 43: Streamwise and in-plane velocity for $Re = 4300$ at $x, y = [-0.3\, a, 0.6\, a]$. To enable comparison, the bulk velocity $\bar{u}_\varphi$ has been subtracted from u_φ. All three velocities show a characteristic modulation with a period of $0.3076\,\text{s}$. The signal is obviously not strictly sinusoidal.

For the level of $1.55\,U$ and its vicinity, including the entire high speed core region, a rather small but evident difference and hence modulation can be observed in fig. 44 during one wavelength. This region is subject to minor 'swell', i.e. a change between a slightly more or less pronounced peak considering a vertical velocity profile. The modulation in the low speed core region seems negligible. By far most notably the modulation resides in the vicinity of level $1\,U$, especially at the 'end' of the cross stream wall layer or in region 1 respectively. Thus fig. 45
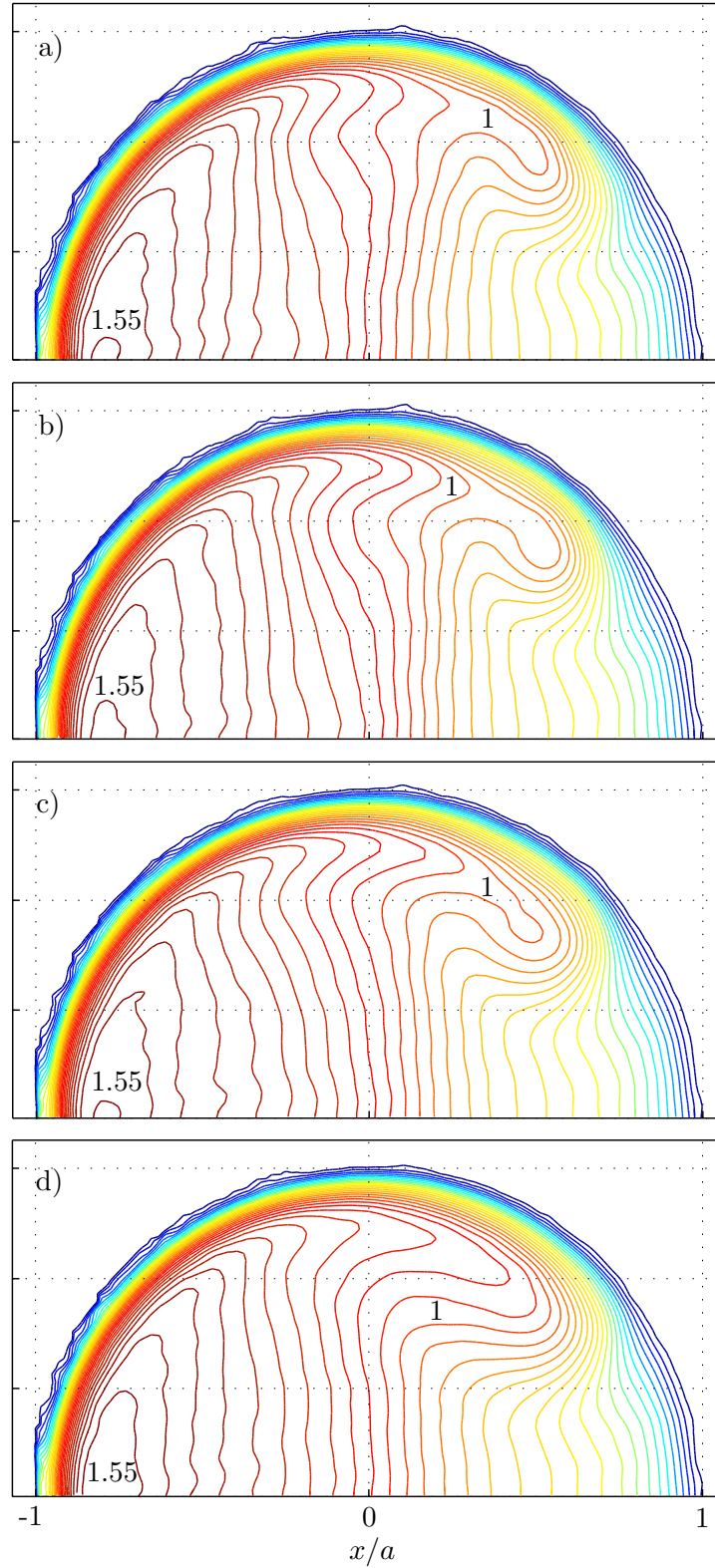
Figure 44: Contours of the (instantaneous) streamwise velocity over one wavelength λ at Re = 4300. a) $\lambda = 0$, b) $\lambda = 1/4$, c) $\lambda = 1/2$ and d) $\lambda = 3/4$. The level of $1.55\,U$ and $1\,U$ is indicated for reference. Each image is the average of 8 periods. See also *mov-Re4300.streamwisevelocity.contour.avi* and *mov-Re4300.streamwisevelocity.contourf.avi* for a fully time resolved picture.

73
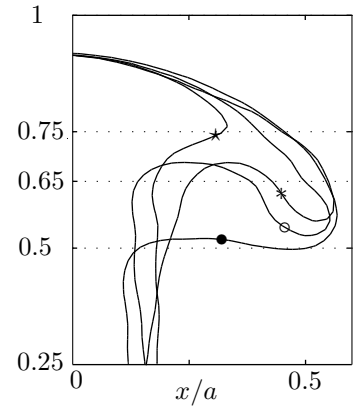
Figure 45: Detail of the contours of the streamwise velocity for level $1\,U$ over one wavelength λ at $\mathrm{Re} = 4300$, superposed in a single picture. $(*)\lambda = 0$, $(\star)\lambda = 1/4$, $(\circ)\lambda = 1/2$ and $(\bullet)\lambda = 3/4$.

shows a closeup of this region to elaborate the change of the contour line at $1\,U$ during one period.

To round out the picture fig. 46 provides details of the periodic modulation of the velocity field by presenting the variation of horizontal profiles along $y = 0.65\,a$, i.e. through the upper 'arm' of the 'armchair'. In this view it is most obvious that the strongest alteration of the flow field is located in region 1, realized by periodic lifting and receding of the 'armrests'. Note furthermore the local minimum for $\lambda = 0, 1/4$ and $1/2$, which almost disappears for $\lambda = 3/4$. A process which appears like the periodic development or lengthening and broadening of an somehow finger like appendix in fig. 45.
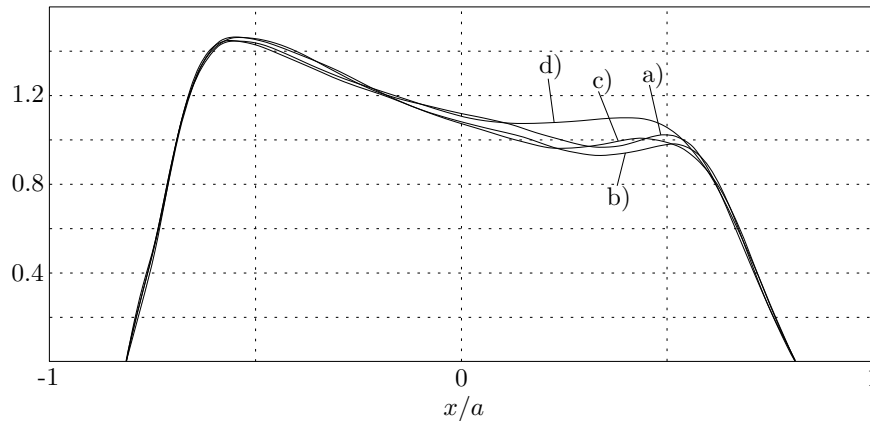
Figure 46: Horizontal profiles (along $y = 0.65\,a$, see fig. 45, i.e. through the upper 'arm' of the 'armchair') of the instantaneous streamwise velocity during one wavelength λ at $\mathrm{Re} = 4300$. a) $\lambda = 0$, b) $\lambda = 1/4$, c) $\lambda = 1/2$ and d) $\lambda = 3/4$.

5.4.2 Large scale velocity fluctuations

As a next step the large scale velocity fluctuations (similarly used: perturbations) are explored at the same Reynolds number of 4300. Fig. 47 and 48 show the vector 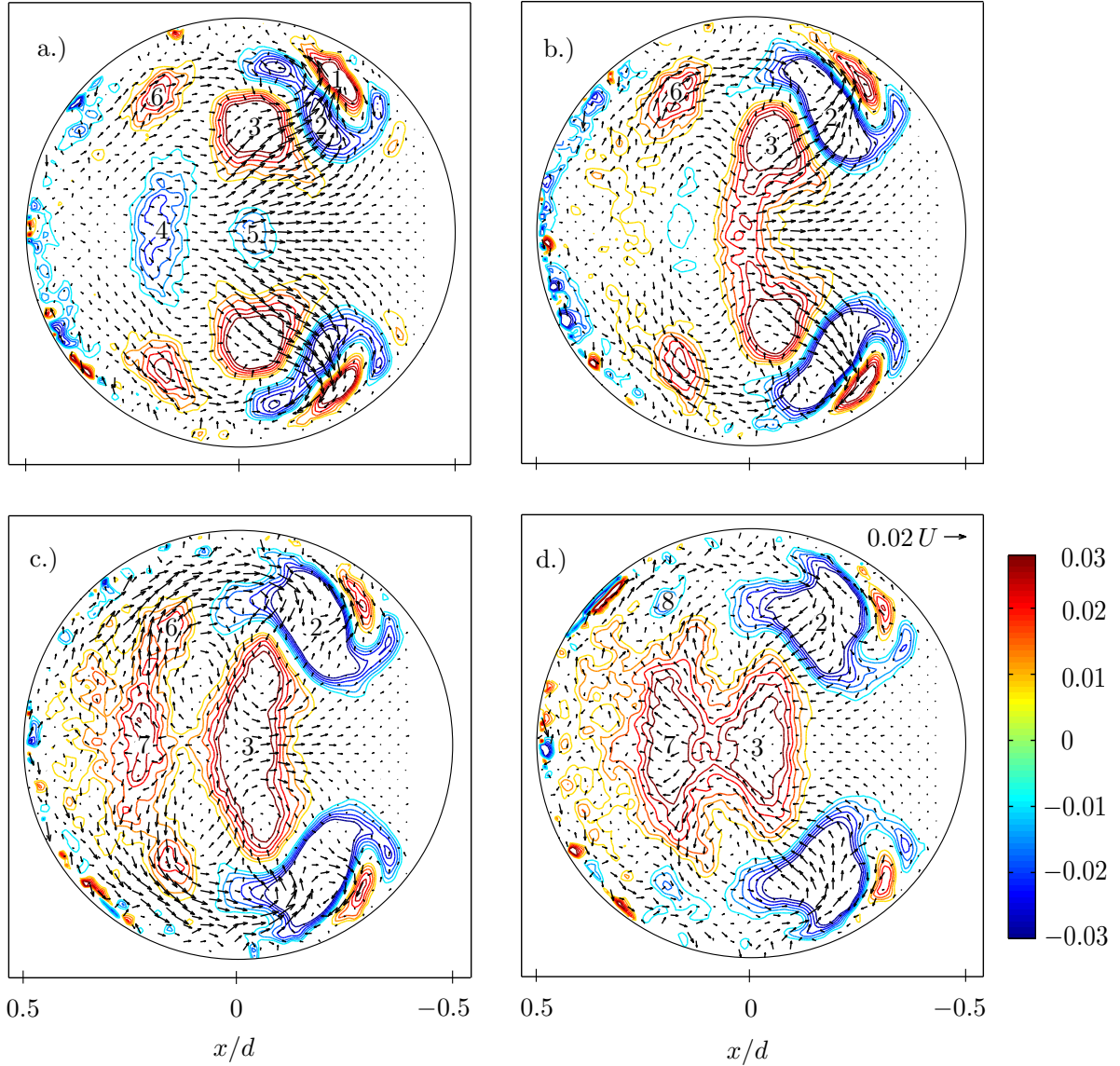field of the cross-stream velocity fluctuations, i.e. the cross-stream velocity field minus the cross-stream mean velocity $(u_r - \bar{u}_r, u_\alpha - \bar{u}_\alpha)$, and contours of the streamwise velocity fluctuations $(u_\varphi - \bar{u}_\varphi)$, again during one period of the modulation. The contours of streamwise velocity fluctuations hence indicate regions where the instantaneous flow field is faster or slower than the mean streamwise velocity. For a higher time resolution the period is displayed in increments of $1/8\lambda$.

At first sight the time dependent development of the fluctuations is quite complex, the perfect mirror symmetric appearance regarding the horizontal plane is clear without ambiguity though. The following description is only related to the upper half of the tube hence. The magnitude of the fluctuations in the streamwise direction is of order $\pm 0.06\,U$, the magnitude of the fluctuations of the in-plane velocity of order $\pm 0.02\,U$.

Looking solely at the streamwise fluctuations in the first instance, for $\lambda = 0$ a kind of convoluted arrangement of areas of positively and negatively directed fluctuations is seen in region 1. Closest to the pipe wall, at the end of the cross stream wall layer, a small area (1) of positive fluctuations is seen. Directly adjacent a triple peaked area (2) of negative fluctuations is found, embracing on half of area (1). Neighboring towards the center of the tube a large area (3) with opposite sign is located. In the left middle of the cross section and in the very center two more areas (4 and 5) of rather small negatively directed fluctuation, spreading across the horizontal axis, is seen. Furthermore area (6), where a small positive fluctuation is seen, resides in the upper left half below the cross stream wall layer. The small irregular 'islands' at the very left close to the outer tube wall, characterized by relatively steep gradients, are regarded as measurement noise coming from reflections of the tube wall.

During $\lambda = 1/8$, $\lambda = 2/4$ and $\lambda = 3/8$ area (1) is shrinking and simultaneously moving slightly downwards to the right, i.e. with the direction of the cross stream wall layer. At the same time area (2) grows considerably, while area (3) coalesces with its mirroring counterpart and moves to the center and then leftward, where it coalesces again with the new area (7). Area (7) seems to develop simultaneously to (6) and is not clearly different. For $\lambda = 3/8$ the relatively small fluctuation in area (8), where previously (6) had been located, has changed signs. Area (4) and (5) vanish between $\lambda = 1/8$ and $\lambda = 2/4$.

For $\lambda = 1/2$ area (3) in the center of the tube has vanished, only (7) is still visible but also vanishes until $\lambda = 5/8$. Between $\lambda = 3/8$ and $\lambda = 1/2$ area (2) has split into two separate regions (2) and (3), whereof the one closer to the wall (2) experiences the same fading out until $\lambda = 7/8$ as area (1) for $\lambda = 0$ to $\lambda = 3/8$. At the same time the part of (2) which is closer to the center of the tube (3) experiences the same process as area (3) for $\lambda = 0$ to $\lambda = 3/8$, only with opposite sign. For $\lambda = 7/8$ (3) is vanishing in the center of the pipe, whereby it becomes clear that (4) and (5) for $\lambda = 0$ are just the continuation of it. Between $\lambda = 1/2$ and $\lambda = 5/8$ a rather sudden expansive development of area (1) into the former place of the now separate areas (2) is observed. (1) hence is kind of the positively directed counterpart of (2).

Figure 47: Fluctuating velocities during one wavelength λ at Re = 4300. Vector field of the cross-stream velocity fluctuations and contours of the streamwise velocity fluctuations, both normalized with the bulk velocity U. For the sake of clearer representation $u_\varphi - \bar{u}_\varphi$ is displayed only for ± 0.008 to ± 0.03 in increments of 0.004. The maximum levels would be about ± 0.065. a) $\lambda = 0$, b) $\lambda = 1/8$, c) $\lambda = 1/4$ and d) $\lambda = 3/8$. Each image is the average of 8 periods. See also *mov-Re4300.fluctvelocity.avi* for a fully time resolved picture.
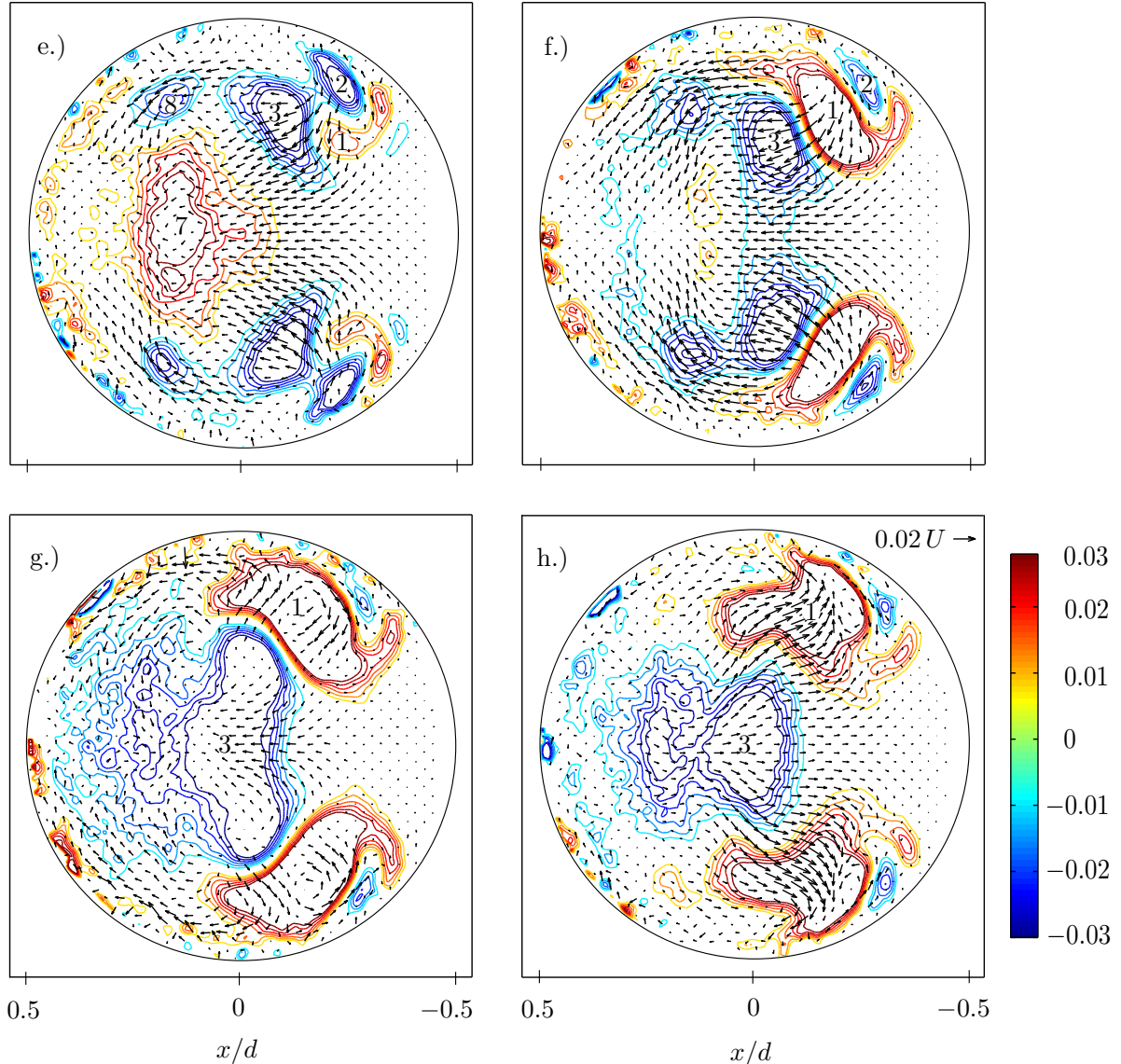
Figure 48: Continuation of fig. 47. a) $\lambda = 1/2$, b) $\lambda = 5/8$, c) $\lambda = 3/4$ and d) $\lambda = 7/8$.

A matter best seen in the movie (*mov-Re4300.fluctvelocity.avi*) is the clockwise (valid for the upper region 1, counterclockwise for the lower region 1) turning around of two areas of oppositely directed fluctuations within region 1. Looking closely at region 1 in the direct vicinity of the pipe wall it is noted, that at any instant of time there is both a positively and negatively directed fluctuation present. Each of them goes through a cycle of being small at the pipe wall while simultaneously moving along the wall with the direction of the flow in the cross stream wall layer, followed by sudden growth until more or less covering the whole region 1, then split, whereas the smaller part close to the upper pipe wall starts the cycle again.

Looking at the fluctuations of the in-plane velocity, the main activity is found in the area directly in between region 1 in the upper and lower half of the cross section (approximately the region called 'high RMS' in fig. 8). Most eye-catching is the periodic change of direction of $u_r - \bar{u}_r$: during $\lambda = 7/8, 0, 1/8$ and, less distinct, $\lambda = 1/4$, this area in the vicinity of

(a) View from the inside of the bend

(b) View from the outside of the bend
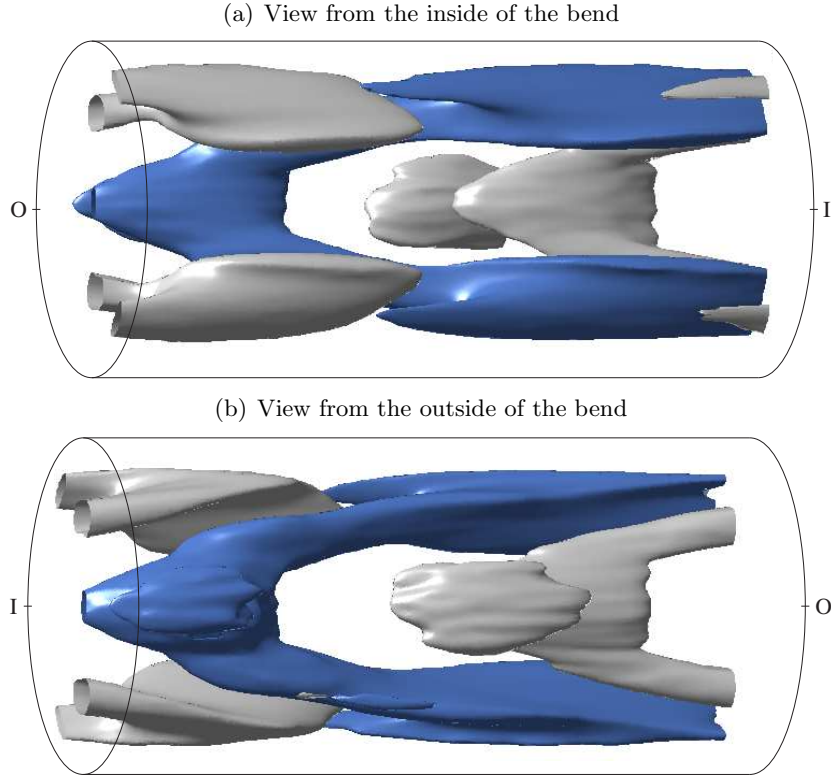
Figure 49: Isosurfaces of streamwise velocity fluctuations during one wavelength λ at $\pm 0.028\,U$ and $\text{Re} = 4300$. Views from the inside and the outside of the bend (I denotes inner bend, O outer bend). Fluid flows rightwards. Blue (dark gray) for negative, light gray for positive. The images are an average of 8 periods. The velocity field is mapped to a straight pipe.

the horizontal axis is dominated by a fluctuation towards the right or the inside of the torus respectively, while during $\lambda = 1/2, 5/8$ and $3/4$ it is dominated by a fluctuation towards the outside of the bend. Additionally the fluctuation is directed back and forth towards region 1 the closer it is located to region 1. Furthermore a comparatively weaker fluctuation is observed *adjacent* to the cross stream wall layer, as seen e.g. for $\lambda = 1/8$ in the vicinity of area (6). It is very obvious though that only minor fluctuations of the in-plane velocity can be seen *within* the cross stream wall layer. The center of the high speed core region, especially the area of the highest streamwise velocity, and the whole low speed core region are not subject to in-plane fluctuations.

For a time and space resolved 3-dimensional view of the observed large scale fluctuations in the streamwise direction isosurfaces at $\pm 0.028\,U$ are shown in fig. 49 as seen from the inside and from the outside of the bend, again for $\text{Re} = 4300$. Regions where the streamwise velocity is slower or faster than the purely laminar profile are coded in blue (dark gray) and light gray, respectively.

The convoluted arrangement of areas of positively and negatively directed fluctuations, yielding a twofold streamwise periodicity of regularly interchanging regions, is clearly seen. Furthermore the mirror symmetric appearance in all cross-sections regarding the horizontal axis is
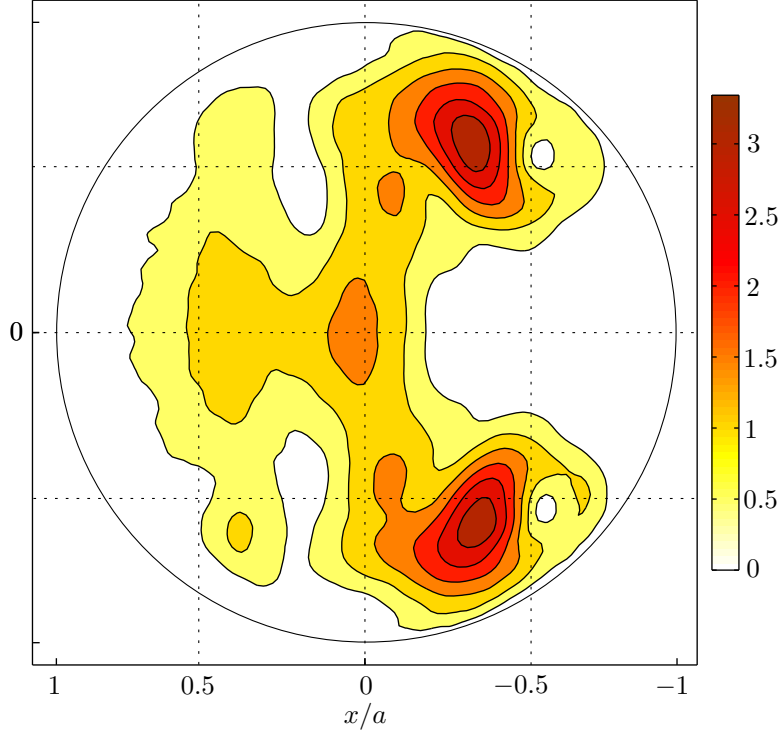
Figure 50: Distribution of the amplitude of the streamwise velocity fluctuations across the cross section for the characteristic dominant frequency at Re = 4300. Amplitude in arbitrary units.

obvious. While the fluctuations in region 1 and the high RMS region (area (1), (2) and (3) in fig. 47 and 48) appear interdigitated and closely connected, the fluctuations in the high speed core region (area (4) and (7) in fig. 47 and 48) constitute only loose and disconnected cloudlets.

Looking at the distribution of the strength of the streamwise velocity perturbations at the frequency which is dominant and characteristic for the first instability, the largest amplitude is expectedly found in region 1 again. Fig. 50 shows the largest amplitude around $x, y = [-0.36\,a, 0.57\,a]$ and a second, considerably smaller peak in the very center of the tube. The high speed core region is weakly modulated, while the low speed core region lacks of any modulation. Interestingly very close to the highest modulation, immediately adjacent to the right from region 1, a small island of zero amplitude is found (around $x, y = [-0.56\,a, 0.5\,a]$). In general the figure clearly retraces the emphasized areas of region 1 and the high RMS region as in the model of fig. 8.

Fig. 51 reveals the cross sectional distribution of the amplitude of the in-plane velocity fluctuations for the characteristic dominant frequency at Re = 4300. The border of the cross stream wall layer is clearly displayed. Strong modulation is found, rather broadly strewn, in the high RMS region again, stretching quite far into the high speed and low speed core regions. Furthermore an unaccented peak in region 1 and another peak directly adjacent to the cross stream wall layer at around $x, y = [0.12\,a, 0.75\,a]$ is found. Within the cross stream wall layer minor modulation is found, except for the area adjacent to the peak just mentioned before and in the area where the wall layer ends up in region 1.
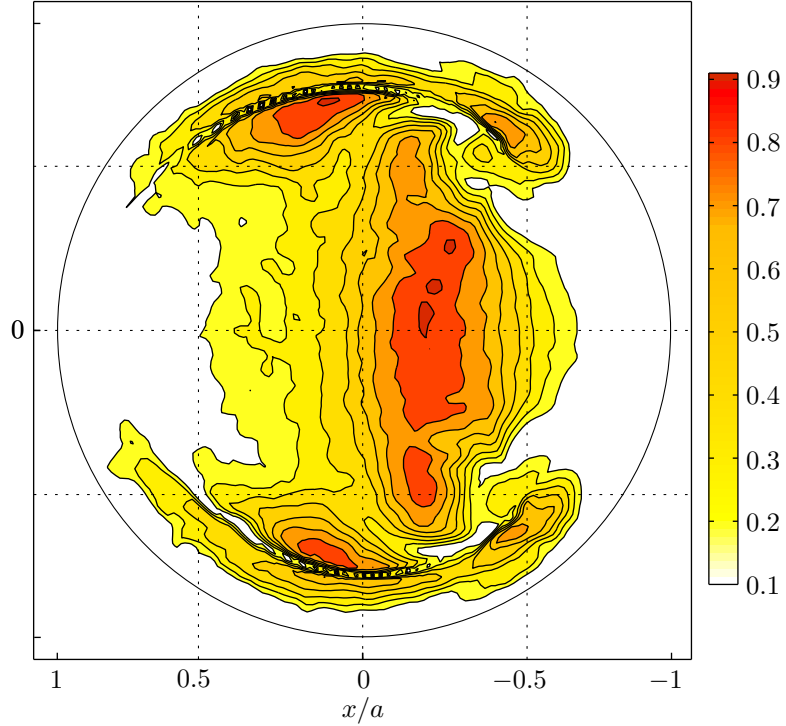
Figure 51: Distribution of the amplitude of the in-plane ($\sqrt{u_r^2 + u_\alpha^2}$) velocity fluctuations across the cross section for the characteristic dominant frequency at Re = 4300. Amplitude in arbitrary units.

Summing up, the streamwise fluctuations seem to emanate from region 1. In a periodic process areas of positively and negatively directed fluctuation originate in region 1 at a small area close to the wall. The areas then split into two, whereof one area travels towards the center and, after coalescing with a weak but rather widespread area of fluctuation in the high speed core region vanishes, while the other area shrinks to a tiny region near the wall before it starts to grow again. The fluctuations of the in-plane velocity reside in the area directly in between region 1 in the upper and lower half of the cross section and the center of the pipe, and, weaker though, in the vicinity of the upper and lower border of the high speed core region. Even though the in-plane velocity takes by far the highest values in the cross stream wall layer (see sec. 5.3), no major fluctuations of the in-plane velocity are found in this area.

5.4.3 Analysis of velocity power spectra

To detect the exact critical Reynolds number for transition to take place, to find the characteristic development of the bifurcation and to quantify the frequency spectra, LDV measurements of the streamwise velocity at different Reynolds numbers were subjected to a Fourier transformation. The first occurrence of a distinct dominant frequency within the velocity power spectra is considered as an indication of the critical Reynolds number. The development of the respective amplitude of the modulation with varying Reynolds number is considered as indication for the bifurcation scenario (see sec. 2.1).

Fig. 52 shows a time trace for Re = 4350 of the streamwise velocity in the center of region 1, i.e. at the location of the largest amplitude $(x, y = [-0.36\,a, 0.57\,a]$, see sec. 5.4.2), for 4 full revolutions of the actuator. The time trace was measured by means of LDV. The distinct and substantial periodic modulation of the streamwise velocity can be observed best at this point, as the signal-to-noise ratio yields the best values especially close to the critical Reynolds number. The amplitude, i.e. the intensity of the streamwise velocity fluctuations, is of order $\simeq \pm 0.07\,U$ at this point for the Reynolds number displayed. The disturbance of the modulation in the vicinity of the actuator is again well seen. Further away from the actuator the modulation is constant within $\simeq \pm 10\%$. As already stated in sec. 5.2.1, if the actuator is considered to be located at the toroidal angle $\varphi = 0$, only the range $[0.85\pi, 1.15\pi]$ of each revolution is examined hence.
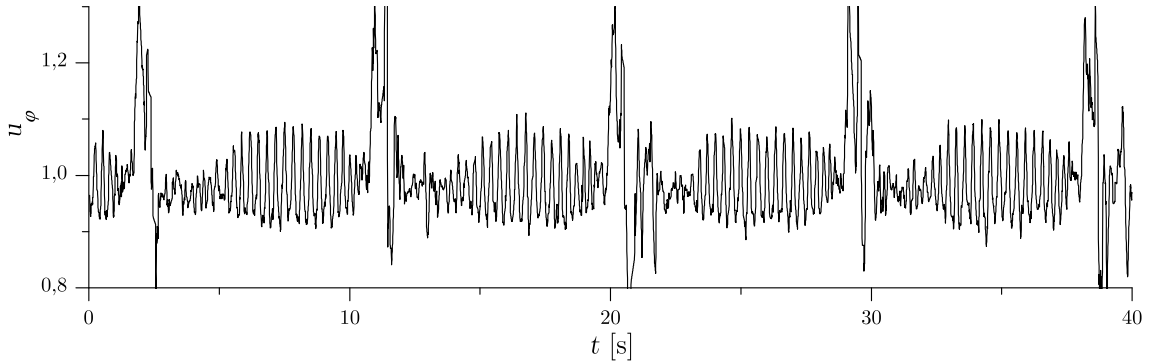
Figure 52: Typical time trace of 4 full revolutions of the actuator for Re = 4350 of the streamwise velocity in the center of region 1, i.e. at the location of the largest amplitude. Each revolution shows a slightly different course of the curve concerning the steadiness of the modulation and also concerning the direct vicinity of the actuator. The time trace was measured by means of LDV.

Fig. 53 (a) shows the velocity power spectra for the same Reynolds number and location as fig. 52 for one revolution of the actuator. The single dominant and characteristic frequency f_1 at 3 Hz with an amplitude of 0.075 is clearly resolved. The amplitude corresponds to the absolute value of the velocity fluctuation at $x, y = [-0.36\,a, 0.57\,a]$, expressing the intensity of the fluctuation in streamwise direction. The maximum intensity is hence of the order of 15% of the mean velocity for Re = 4350. The 2nd harmonic $(2f_1)$ of the dominant frequency at 6 Hz is also well resolved, showing an amplitude of less than one third of the dominant frequency.

Close to the first onset of the oscillations, i.e. in the range $4080 \leq$ Re ≤ 4150, a critical slowing

(a)

(b)
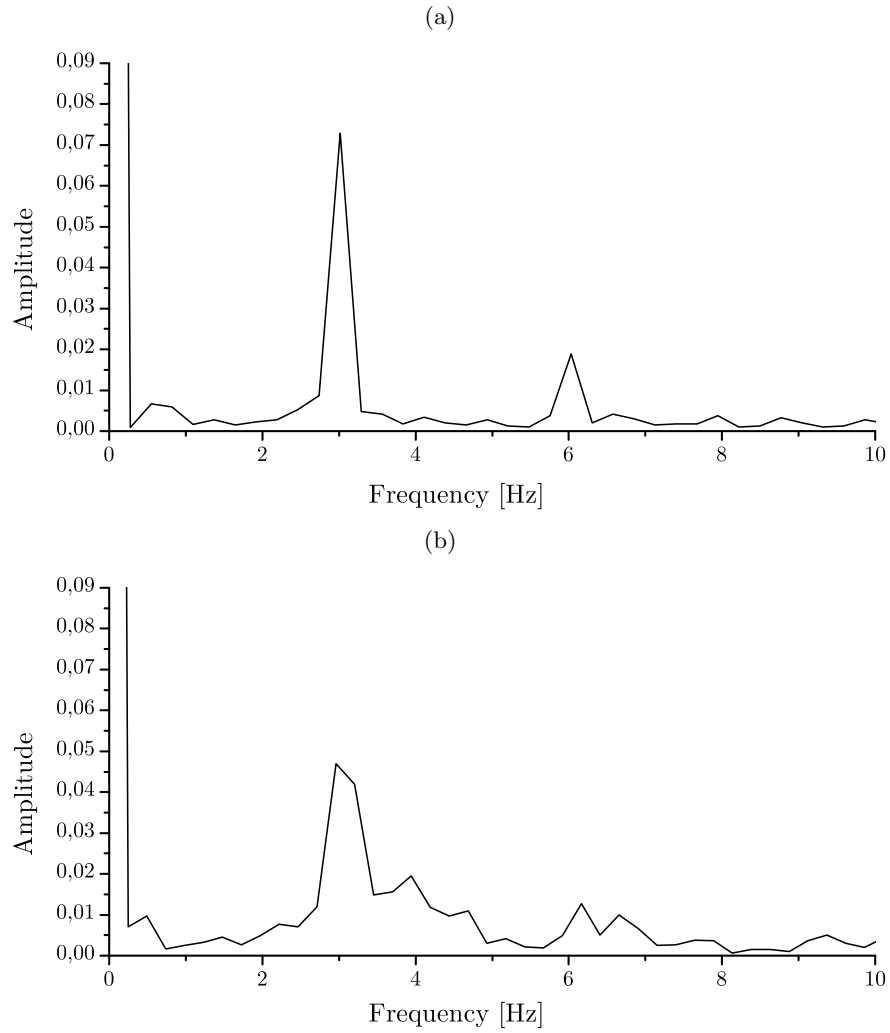
Figure 53: Amplitude and frequency of the velocity power spectra of one revolution in the range $\varphi = [0.85\pi, 1.15\pi]$. The amplitude corresponds to the absolute value of the streamwise velocity fluctuation, normalized with the mean velocity. a.) Re = 4350: A single dominant frequency f_1 at 3 Hz and its 2nd harmonic ($2f_1$) at 6 Hz is clearly resolved. The exact values for f_1 are practically constant for each revolution, while the respective amplitude varies considerably (see fig. 56). b.) Re = 4400: the same single frequency f_1 is still dominant, yet its (mean) amplitude is lower than for Re = 4350. Furthermore, one or more additional frequencies in the immediate vicinity of the dominant frequency are detectable, every revolution gives considerably differing results though. The detection of a mean value would require significantly longer observation times.
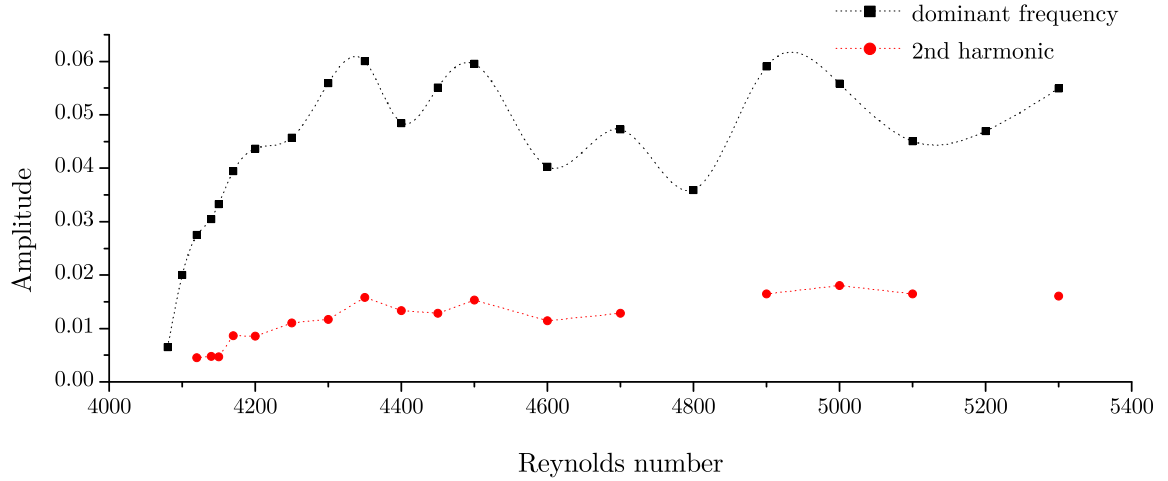
Figure 54: Amplitude of the dominant frequency f_1 and its 2nd harmonic for increasing Reynolds number. The amplitude corresponds to the absolute value of the streamwise velocity fluctuation, normalized with the bulk velocity. The first detection of the dominant frequency is at Re = 4080. Below Re = 4120 and at Re = 4800 and Re = 5200 no values for the 2nd harmonic were detected.

down (see sec. 2.1.1) regarding the absolute values of the amplitude was observed. The exact relaxation rate was not investigated. After max. 5 minutes of waiting time at the same Reynolds numbers the amplitude of the modulation would reproducibly exhibit almost the same (mean) value, independent of if the Reynolds number had been increased or decreased to the current value. No effects of hysteresis were found.
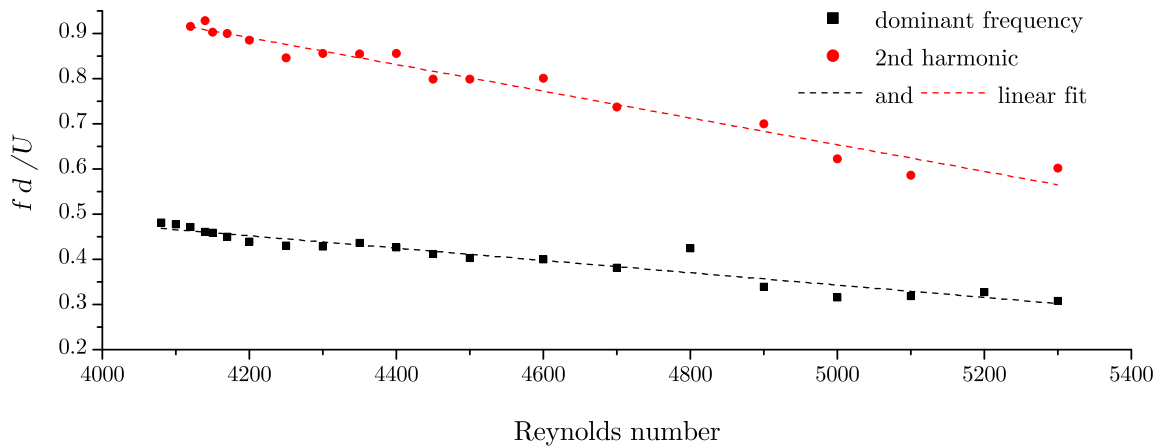
Figure 55: Nondimensional dominant frequency and its 2nd harmonic for increasing Reynolds number. Below Re = 4120 and at Re = 4800 and Re = 5200 no values for the 2nd harmonic were detected. $\hat{f}_1$ sets in with $\simeq 0.5$ at Re_{crit} an then slowly though quite constantly decreases with increasing Reynolds number.

Nevertheless, every revolution still exhibited a slightly different dominant frequency and (mean) amplitude, even after the effect of critical slowing down had been ruled out. 5 revolutions were hence analyzed for each Reynolds number and then the mean value taken. Fig. 54
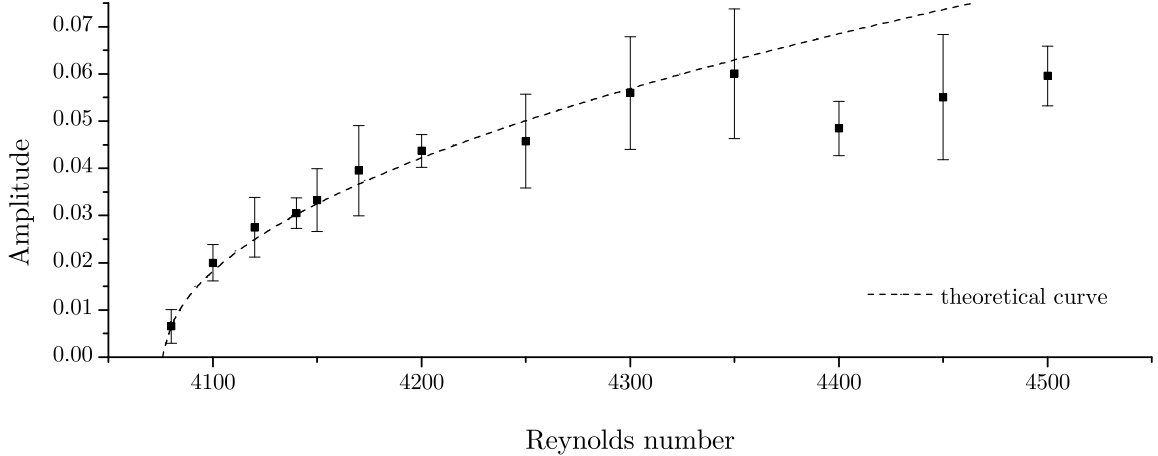
Figure 56: Amplitude of the dominant frequency and theoretical curve of a square root function for $4000 \leq \text{Re} \leq 4500$. Error bars represent the maximum deviation of the measured values for single revolutions. From Re = 4080 to Re = 4350 the measured values coincide very well with $y = [1.45 \times 10^{-5} \, (\text{Re} - \text{Re}_{crit})]^{0.5}$, shown as theoretical curve (dashed line).

and 55 show such mean values of the single dominant frequency and its corresponding amplitude for the range $4000 \leq \text{Re} \leq 5400$. The values for the 2nd harmonic are also shown. A slight inharmonicity is observed, as the values of the 2nd harmonic deviate from being an exact twofold of f_1 with up to 3%.

The normalized dominant frequency $\hat{f}_1 \cong 0.5$ at Re_{crit} and then slowly decreases with increasing Reynolds number. A linear fit to the curve (dashed line in fig. 55) gives

$$\hat{f}_1 = \frac{f_1 d}{U} = -1.37 \times 10^{-4}\text{Re} + 1.02 \tag{30}$$

The decrease is mainly due to the increasing velocity, as f_1 is quite constant for $\text{Re}_{crit} \leq \text{Re} \leq 4700$. No further dominant frequencies are found in the velocity spectra in the range $\text{Re}_{crit} \leq \text{Re} \leq 4350$. The emergence of the dominant frequency at Re = 4080 is very well resolved. The amplitude quickly increases close to its first appearance, seemingly following the curve of a square root function. This conjecture is further supported by fig. 56 and 57. In fig. 56 the onset of the frequency and the development of the amplitude until Re = 4500 has been plotted with a theoretical curve of $y = [1.45 \times 10^{-5} \, (\text{Re} - \text{Re}_{crit})]^{0.5}$. Starting from Re = 4080 to Re = 4350 the measured values coincide very well with the root function. In fig. 57 the squares of the amplitudes are plotted. The resulting data points can be linearly fitted well by

$$A^2_{dominant} = 1.29 \times 10^{-5}\text{Re} - 0.05 \tag{31}$$

and

$$A^2_{2ndharmonic} = 9.17 \times 10^{-5}\text{Re} - 0.004, \tag{32}$$

again for Re = 4080 to Re = 4350. At Re $\approx$ 4400 routes separate though.

Re $\approx$ 4400 is the range where the characteristic wavelength λ was visually observed to start varying between $2-4d$ (see sec. 5.1). In particular when considering fig. 53 (b) it seems likely that

84
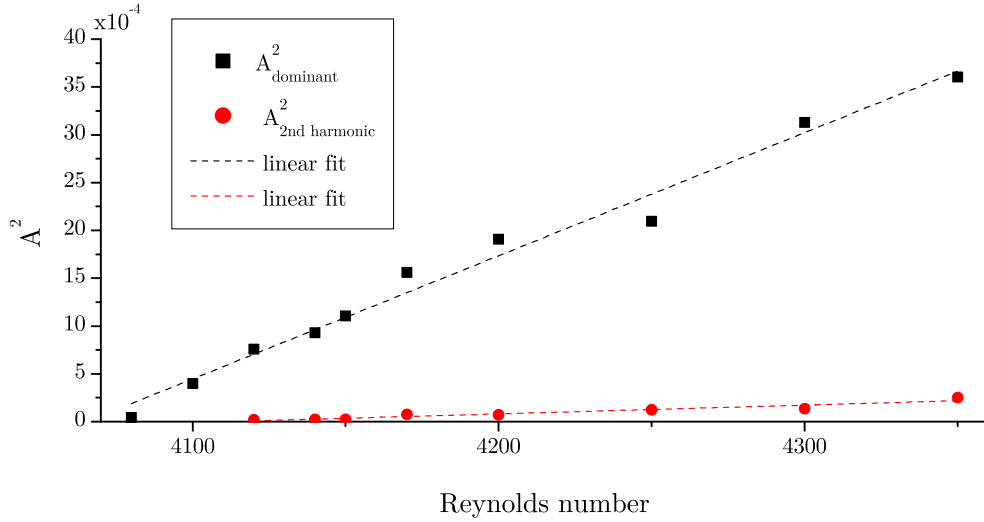
Figure 57: Amplitudes squared of the dominant frequency and its 2nd harmonic for increasing Reynolds number. The amplitude corresponds to the absolute value of the streamwise velocity fluctuation, normalized with the bulk velocity.

in this range a further bifurcation to a state of two different, incommensurate frequencies $\hat{f}_1$ and $\hat{f}_2$ takes place. The second frequency $\hat{f}_2$ is conjectured to exhibit a value closely above the first frequency. In spite of careful investigation of the velocity spectra no further seperate *dominant* frequency could be identified in the range directly above Re = 4350, as every revolution exhibited different spectra. The detection of a mean value might require significantly longer observation times.

It is noted that the single dominant frequency $\hat{f}_1$ of the first instability is clearly preserved at higher Reynolds numbers, i.e. it can be traced even in the regime where the system has obviously gone through one or more further instabilities. No attempt has been made to trace the signal to even higher Reynolds numbers than 6000.

5.4.4 Pressure drop during one wavelength

To investigate the modulation of the pressure drop in the streamwise direction during one wavelength, Δp was measured between two pressure holes in a very short distance of just $1d$, which is approx. the distance of half a wavelength λ (see sec. 5.1). It would certainly be interesting to also measure pressure differences between two different radial positions, i.e. within the same cross section. Since pressure holes at locations for $\alpha \neq \pi/2$ would have needed some additional tricky modifications to the experimental setup this has not been done within the present work.

Fig. 58 shows that the modulation of the streamwise velocity field is also reflected in the streamwise pressure drop. During one full wavelength λ the pressure drop measured at $\alpha = \pi/2$ varies with $\sim \pm 0.05\,\mathrm{Pa}$ or $\sim 10 - 15\%$ of the total pressure drop. Compared with the results for the modulation of the streamwise velocity (sec. 5.4.2) this seems quite high, as the streamwise velocity fluctuation exhibits a comparable relative magnitude only in region 1. Future measurements of the circumferential pressure profile during one full wavelength might shed more light on this observation.

A Fourier analysis of the data shown in fig. 58 yields the same dominant frequency $(\hat{f}_1)$ as for the streamwise velocity (see sec. 5.4.3). It should be recalled however that water has been used as working fluid for pressure drop measurements (sec. 3.2.4), resulting in a different absolute time scale in fig. 58.
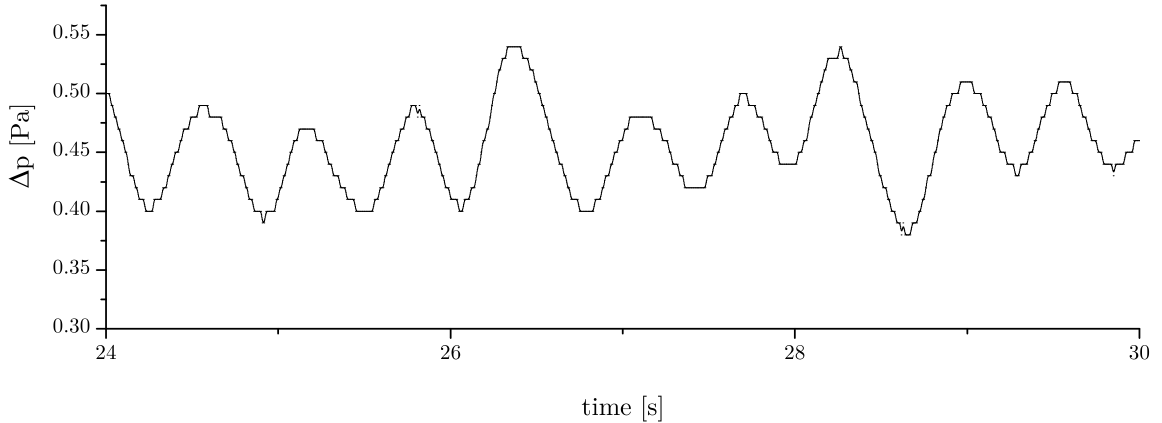
Figure 58: Typical time trace of the pressure drop during 6 seconds (corresponding to $\sim 43.5\%$ of one full revolution or the range $[0.75\pi\varphi, 1.25\pi\varphi]$ if the actuator is considered to be located at $\varphi = 0$) at Re = 4350. Δp was measured between two pressure holes in a short distance of just $1d$ or $\Delta\varphi = 0.031\pi$ respectively, i.e. in the distance of half a wavelength λ. On a very small scale of $\sim \pm 0.05\,\mathrm{Pa}$ in the streamwise direction the dominant frequency is also reproduced in the pressure drop measurements.

5.4.5 Summary of the results on the first instability

For Re $= 4080 \pm 2\%$ a supercritical Hopf-bifurcation from the basic toroidally symmetric flow to a laminar flow which is periodically modulated in the streamwise (toroidal) direction is found. The emerging pattern is almost stationary in a frame of reference moving with the actuator, exhibiting a wave celerity slightly above ($\sim 12\%$) the mean bulk velocity of the flow. Close to the critical Reynolds number the amplitude of the streamwise modulation is very weak. With increasing Reynolds number, the modulation amplitude of the streamwise velocity grows and the associated flow pattern becomes more distinct.

The amplitude of the perturbation is largest for the contour-line value $1U$, especially in region 1. The strongest alteration of the flow field is, hence, realized by periodic speeding up and slowing down of the streamwise velocity in the area located in region 1, i.e. at the end of the cross-stream wall layer. The nondimensional frequency $\hat{f}_1$ of the modulation is found to set in with $\simeq 0.5$ at Re_{crit} an then slowly though quite constantly decrease with increasing Reynolds number. A linear fit gives $\hat{f}_1 = a\mathrm{Re} + b$ with $a = -1.37 \times 10^{-4}$ and $b = 1.02$. The intensity of the streamwise velocity fluctuations in region 1 is of the order of up to 15% (at Re $= 4350$) of the mean velocity. The modulation of the streamwise velocity field is also distinctly reflected in the streamwise pressure drop.

The single dominant frequency f_1, which could be regarded as the 'fingerprint' of the first instability, is preserved to higher Reynolds numbers. At a second critical Reynolds number of ~ 4400 a transition to a flow with two (or more) incommensurate frequencies f_1 and f_2 is found. The two frequencies seem to be irrationally related, hence this is a quasi-periodic flow. The exact value of f_2 has not been identified though narrowed down to a value close to the one of the first dominant frequency f_1.

5.5 Transition, higher Reynolds number regime

The flow at Reynolds numbers above ~ 4400 is found to become increasingly more complex. Therefore, only a few properties of the flow will be highlighted and some characteristic features indicated in the following. Issues are only touched upon and certainly need further investigation and clarification for definitive and satisfactory results.

As already observed and described in sec. 5.3.2 (see in particular fig. 41), differences are small between the velocity profile at Re = 3600, where the flow is still steady, and the one at Re = 6000. Neither the vertical nor the horizontal profiles of the streamwise velocity exhibited any substantial changes in the overall appearance and in the normalized heights of their peaks. The previous section (5.4) has shown that for $\text{Re}_{c1} = 4080$ a supercritical transition from the steady, toroidally symmetric basic flow to a laminar flow which is periodically modulated in the streamwise (toroidal) direction takes place. The rotational invariance regarding φ is replaced by a discrete periodic rotational invariance. The symmetry with respect to the horizontal midplane of the cross section is preserved.

For $\text{Re}_{c2} \simeq 4400$ strong indication of a further bifurcation was found. Visual observations (see sec. 5.1) showed a departure from exact streamwise periodicity of the flow patterns and the analysis of velocity power spectra (sec. 5.4.3) indicated two or more different, incommensurate frequencies.

To further investigate the characteristics of the presumed second instability, fig. 59 displays PIV measurements of the instantaneous flow field at Re = 4500 and Re = 4600, i.e. in the range just above the assumed second bifurcation. Both instances of time shown are more or less arbitrarily chosen out of the temporal evolution of the flow. Both images clearly demonstrate the breaking of the mirror symmetry regarding the horizontal midplane of the cross section.

The movies *mov-Re4500.totalvelocity.4s.avi* and *mov-Re4600.totalvelocity.4s.avi* illustrate the temporal evolution of the flow better, where fig. 59 (a) corresponds to the flow field after $0.36\,\text{s}$ in *mov-Re4500.totalvelocity.4s.avi* and (b) to the flow field after $0.6\,\text{s}$ in *mov-Re4600.totalvelocity.4s.avi*. In the movies it is also seen that the dominant, periodic modulation of region 1 and the symmetry regarding the horizontal midplane is *mainly* preserved, while *only from time to time* the periodicity in the flow field seems to 'break down' and the symmetry regarding the horizontal midplane is lost. The loss of symmetry indicates a symmetry breaking instability. It is not clear though if the loss is caused by an instability of the bulk flow or an instability of the wall layer.

Without further explanation as mere observation it is noted that fig. 59 also presents an interesting development in the high speed core region, namely in the high speed core region very close to the (outer) pipe wall. Only vaguely recognizable in (a) but already clearly visible in (b) at the moment of breakdown of symmetry regarding the horizontal midplane a 'peninsula' of relatively slow streamwise velocity develops, extending right into the high speed core region. The streamwise length of this presumably vortex-like structure close to the wall is approx. $3-4d$, its location being shifted slowly along the outer wall.

In order to characterize the temporal and spatial behavior of the second instability in a single
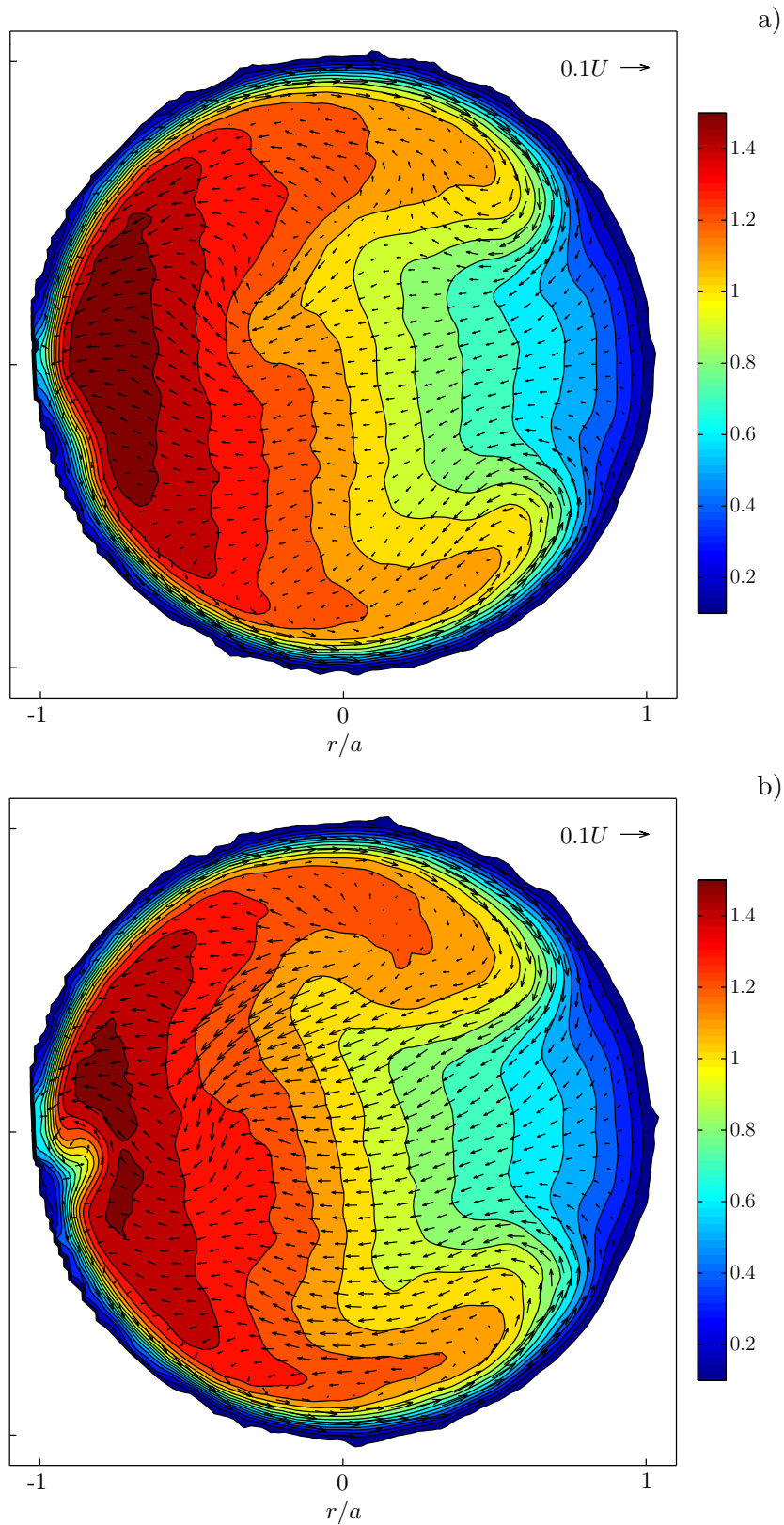
Figure 59: Instantaneous flow fields showing a moment of breakdown of symmetry regarding the horizontal midplane. a.) Re = 4500. b.) Re = 4600. See also *mov-Re4500.totalvelocity.4s.avi* and *mov-Re4600.totalvelocity.4s.avi* for the temporal evolution of the flow.
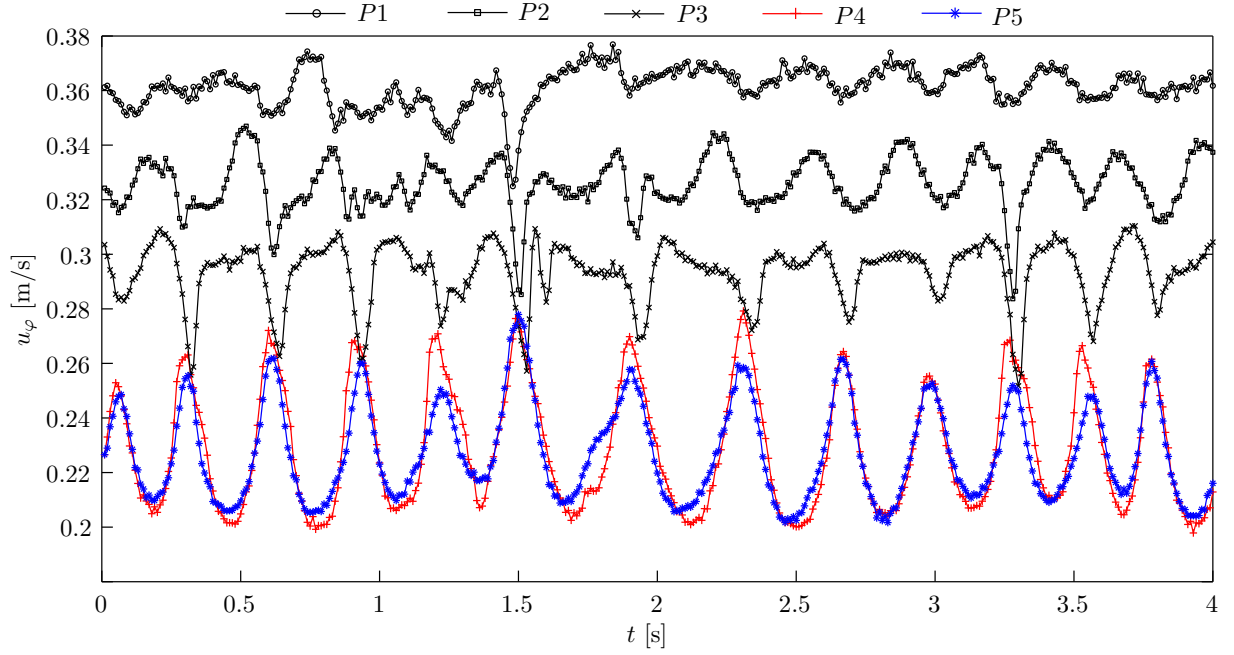
Figure 60: Time traces of the streamwise velocity during 4 seconds (corresponding to $\sim 50\%$ of one full revolution or the range $[0.5\pi\varphi, 1.5\pi\varphi]$ if the actuator is considered to be located at the toroidal angle $\varphi = 0$) at Re = 4600 for 5 different points within the cross section. $P1[0.77\,a, 0]$, $P2[0.51\,a, 0]$ and $P3[0.19\,a, 0]$ are points along the horizontal midplane within the high speed core region of the flow, while $P4[-0.3\,a, 0.6\,a]$ and $P5[-0.3\,a, -0.6\,a]$ represent each center of region 1 in the upper and lower half of the tube. See also *mov-Re4600.totalvelocity.4s.avi* for the temporal evolution of the entire cross section of the flow field.

figure, fig. 60 displays time traces of the streamwise velocity u_φ during 4 seconds at Re = 4600 for 5 different points within the cross section. $P1$, $P2$ and $P3$ are placed along the horizontal midplane within the high speed core region of the flow, while $P4$ and $P5$ represent each center of region 1 in the upper and lower half of the tube.

For a Reynolds number below Re_{c1} these time traces would reproduce, apart from a little noise, straight horizontal lines at all 5 points (as in fig. 31). For a Reynolds number between Re_{c1} and Re_{c2} these time traces would reproduce the signal of a single dominant frequency and its higher harmonics (as in fig. 33), just that especially for $P1$ but also $P2$ and $P3$ the modulation is weak compared to $P4$ and $P5$, as became clear in e.g. fig. 44 and 50. Furthermore, the signal would be perfectly in phase for $P4$ and $P5$, exhibiting the same amplitude and frequency, since both points are mirror symmetric in respect to the horizontal centerline.

For a Reynolds number above Re_{c2} these velocity time traces show a sectionally phase-shifted signal for $P4$ and $P5$, also amplitudes vary individually. The periodicity is clear yet seems slightly disturbed, figuratively speaking as if 'out of balance' just once in a while. By and large the signals of $P4$ and $P5$ are symmetric and periodic though throughout the entire observation time. The signals at $P1$ (weakest), $P2$ and $P3$ (stronger) also indicate some periodicity, but seemingly random events of 'bursts' with relatively high amplitudes (see e.g. the signal at $1.5\,\mathrm{s}$) interfere and perturb the flow field.
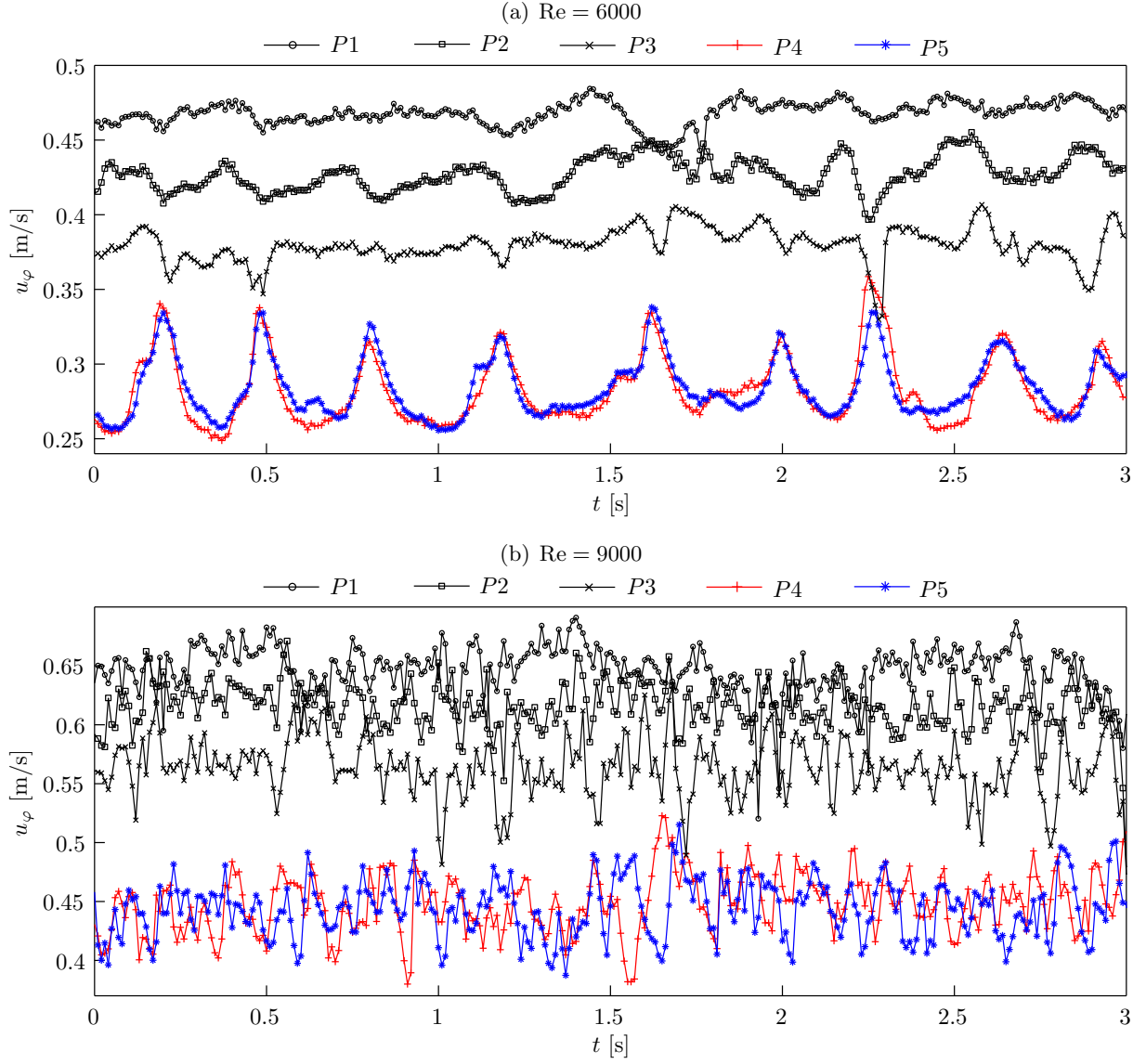
Figure 61: Time traces of the streamwise velocity during 3 seconds (corresponding to $\sim 50\%$ of one full revolution for (a) and $\sim 70\%$ for (b) respectively) at Re = 6000 (a) and Re = 9000 (b) for 5 different points within the cross section. $P1[0.77\,a, 0]$, $P2[0.51\,a, 0]$ and $P3[0.19\,a, 0]$ are points along the horizontal midplane within the high speed core region of the flow, while $P4[-0.3\,a, 0.6\,a]$ and $P5[-0.3\,a, -0.6\,a]$ represent each center of region 1 in the upper and lower half of the tube.

As can be seen in fig. 61 (a), for a Reynolds number of Re = 6000, which is already quite far above Re_{c2}, the velocity time traces are similar to those at Re = 4600. For $P4$ and $P5$ the periodicity is clear yet slightly disturbed. The signal is sectionally phase-shifted and amplitudes vary, but the velocity time traces of $P4$ and $P5$ stay highly congruent in the whole. For the signals of $P1$, $P2$ and $P3$ the difference compared to fig. 60 is a little more articulate, as most of the obvious periodicity is lost. Additionally, high-frequency components can be found in the frequency spectra. A comparison with fig. 61 (b), the velocity time traces at Re = 9000, makes clear that even at Re = 6000 the flow can not be considered (fully) turbulent. But considering the shape of the curves for $P1$, $P2$ and $P3$ in fig. 61 (a) there is strong indication to suppose that turbulent characteristics develop *first* in the high speed core region of the flow.

At Re = 9000, see fig. 61 (b), a fundamentally different behavior is found compared to Re = 6000, as all velocity time traces of the 5 points within the cross section now indicate a primarily random fluctuation of the signal. The obvious high frequency fluctuations of the streamwise velocity evidence turbulent characteristics. It is noted that the overall intensity (i.e. the amplitudes) of the maximum fluctuation have actually decreased at $P4$ and $P5$ and the fluctuation in region 1 has ceased to be dominated by a single frequency.

As the transitional process above Re = 6000 seems to take place in a rather gradual manner, no further incremental steps are shown. To describe and illustrate transition for the range $6000 \leq Re \leq 9000$ to a clearly turbulent state, apart from the visual inspection of velocity time traces, the RMS values of the velocity do not provide an appropriate and reliable measure. Only a detailed analysis of e.g. velocity power spectra for different points within the cross section at different Reynolds numbers may provide a further threshold to distinguish between the state which is still not fully turbulent (small, limited number of frequencies) and a state which indicates mainly turbulent properties (broadband spectrum).

For a qualitative impression of the temporal evolution of the flow at higher Reynolds numbers the following movies of the flow field are provided in the supporting material: *mov-Re4800.totalvelocity.4s.avi*, *mov-Re5000.totalvelocity.2s.avi*, *mov-Re6000.totalvelocity.2s.avi*, *mov-Re9000.totalvelocity.1s.avi* and *mov-Re12000.totalvelocity.1s.avi*.

Summing up the findings for the range above $Re_{c2} = 4400$, a presumably quasi-periodic state exists up to Reynolds numbers > 6000. This state is still dominated by a single frequency in region 1, though the symmetry regarding the horizontal midplane as well as the discrete, periodical symmetry with respect to φ is lost. Transition seems to be considerably different in different areas of the cross section, as high frequency fluctuations of the streamwise velocity are found first in the high speed core region. Further investigations are necessary to determine or at least better narrow down yet another critical Reynolds number, marking the threshold to turbulence. Such threshold might comprise properties of an arbitrary set decision though, as no clear cut value might be found.

5.6 Determination of the friction factor for 1000≤ Re ≤15.000

Apart from the extensive optical measurements the friction behavior in the transitional range of $1000 \leq \text{Re} \leq 15.000$ was obtained by measuring pressure differences between two pressure holes in a distance of $\varphi = \pi/4$ or 12.5% of one full revolution. Similarly as for optical measurements the data were only taken while the actuator was passing through the opposite side of the measurement distance. The pressure holes were located at the top of the upper side of the tube ($\alpha = \pi$). See also sec. 3.2.4 for further details.

Fig. 62 shows a typical time trace of Δp during 20 seconds at Re = 6000. As the figure indicates regions of practically constant pressure drop, apart from providing further evidence of fully developed flow in sufficient distance of the sphere (as shown in sec. 5.2.1), the creation of a friction-factor chart based on these data appears acceptable. Experiments have shown that up to Reynolds numbers of ~ 18.000 the area of temporary constant pressure drop is sufficient for the determination of Δp. Above Re ~ 18.000 Δp does not adapt to a temporary constant value anymore, at least not in a measurement distance of $\varphi = \pi/4$ (for further details see also Kovacs 2012).
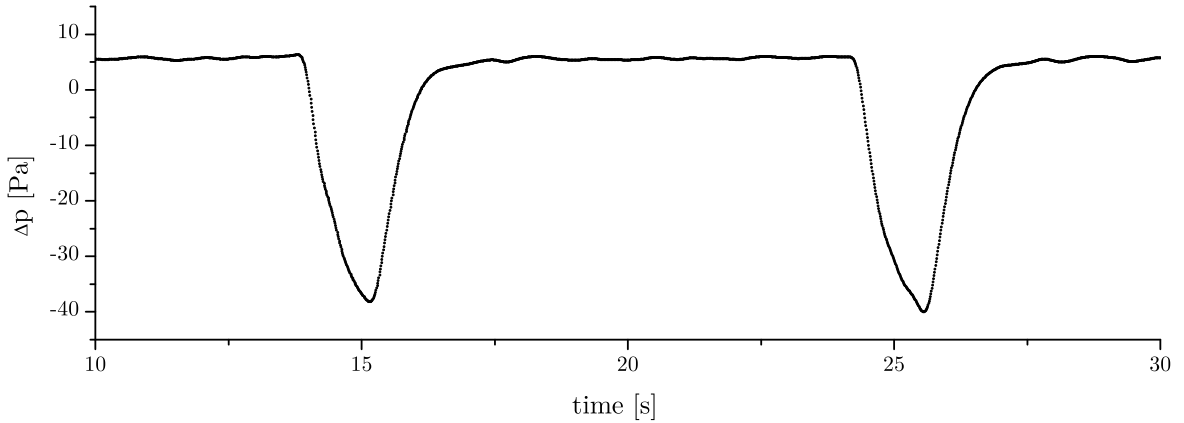
Figure 62: Typical time trace of the pressure drop during 20 seconds at Re = 6000, measured between two pressure holes in a distance of $\varphi = \pi/4$ or 12.5% of full torus length. During transit of the sphere through the measuring section the value drops to $-40\,\text{Pa}$ due to the adverse pressure gradient, hence the transit of the sphere is clearly seen. In sufficient distance to the sphere the pressure drop exhibits quite a constant value with a standard deviation of just 0.2 Pa or 3.5% of the mean value.

Fig. 63 provides the graphical representation of the Fanning friction factor determined from pressure-loss measurements according to (14). For the purpose of comparison with published data the correlations for f_{CL} and f_{CT} from (Mishra & Gupta 1979, given in table 1) are reproduced, too. The present results show very high accordance, especially for the steady laminar regime. Above Re ~ 2500 a minor though distinct departure from the correlation for f_{CL} of Mishra & Gupta (1979) is observed, while for $\sim 5500 \leq \text{Re} \leq 8500$ the accordance is very high again. Beginning with Re ~ 8000 the measured data seemingly follow the shape of f_{CT} in a smaller and smaller distance.

The log-log representation of the measured values shows a soft kink of the curves at Re ~ 8000.

93
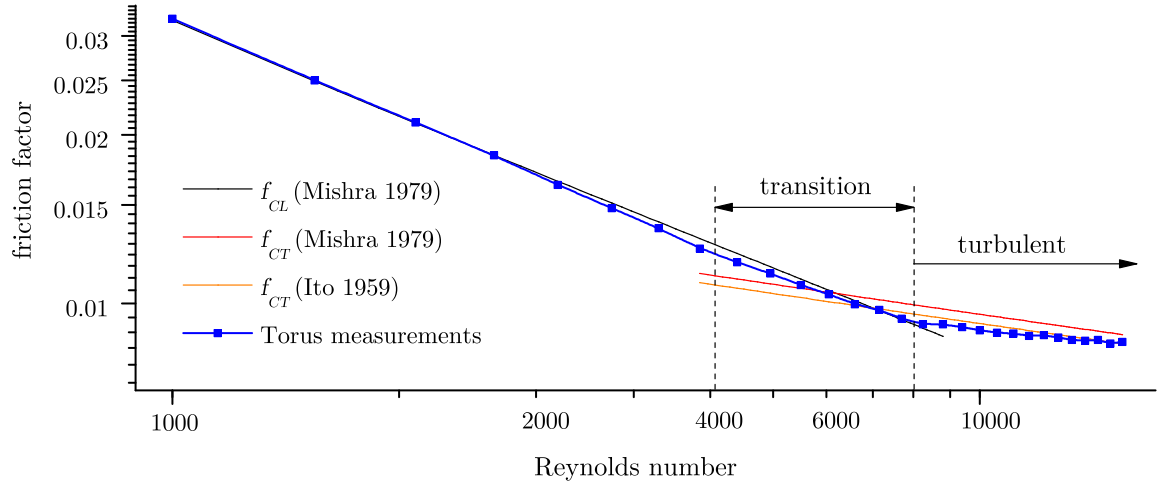
Figure 63: Fanning friction factor determined from pressure loss measurements in the torus according to eq. 14. Measurements were taken in increments of $+500\,\mathrm{Re}$. For comparison selected correlations for f_{CL} and f_{CT} from Mishra & Gupta (1979) and Ito (1959) are also shown (same as in fig. 9 and table 1).

It is obvious that it makes sense to use two different curves to fit the laminar and the turbulent regime. Hence $\mathrm{Re}_{c3} \approx 8000$ can be considered as a third critical Reynolds number for transition to turbulence proper, where a broadband spectrum with high frequency fluctuations dominates the flow.

However, a remarkable feature of fig. 63 is that the present results do not exhibit any sudden change or discontinuity in the trend for the first and the second instability. Contrary to the flow in a straight pipe, in correspondence with transition from stationary to unsteady laminar and to chaotic flow no discontinuity is observed. This indicates that the corresponding unsteady phenomena, up to the regime of manifest turbulence, are not intense enough to influence the overall friction factor significantly.

Compared to straight pipes the increase in the radial gradient of the streamwise velocity leads to an increase of drag in curved pipes. By relating the friction factor chart to the streamwise velocity profiles for increasing Reynolds number (as presented in sec. 5.3.2) it becomes also obvious that the strong radial displacement of the peak streamwise velocity and the respective laminar velocity profile correlate well with the friction factor chart. Fig. 41 has shown that the stretched, sharply contoured typical profile of the laminar flow, where the strong radial displacement of the peak streamwise velocity is dominating the maximum circumferential and axial wall shear stresses along the centerline, is maintained up to Reynolds numbers of $\mathrm{Re} > 6000$. Above this Reynolds number the profile continuously changes to the less sharply contoured profile of turbulent flow, where the displacement of the peak streamwise velocity is distinctly reduced. This is well reflected in fig. 63, where the trends of the curve change exactly in this range. This also explains why the difference between the friction coefficient for curved and that for straight pipes decreases from a maximum value in the laminar flow to a minimum in turbulent flow (displayed in fig. 9).

94

5.7 Abstract table of key points of the transition scenario

In spite of the continuous transition scenario concerning pressure drop and turbulent properties, the present investigation has clearly revealed a few distinct key points of the transition scenario. For the purpose of clarity they are summarized in table 4. Based on the Ruelle-Takens-Newhouse-scenario (see sec. 2.1), a Hopf-bifurcation is conjectured for Re_{c2}.

range	description of state	bifurcation	symmetry
$Re < Re_{c1} = 4080$, $De < De_{c1} = 906$	steady, laminar basic flow		toroidally (rotationally with respect to φ); mirror symmetric regarding the horizontal midplane; mirror symmetric regarding the vertical midplane (only for very small Re)
$Re_{c1} < Re < Re_{crit2} = 4400$, $De_{c1} < De < De_{c2} = 977$	the flow is periodically modulated in the streamwise (toroidal) direction	Hopf, super-critical	discrete/periodical toroidally (rotationally with respect to φ); mirror symmetric regarding the horizontal midplane
$Re_{c2} < Re < Re_{c3} \approx 8000$	quasi-periodic*, still dominated by the modulation in region 1	Hopf*, supercritical*	
$Re > Re_{c3}$	turbulent properties dominate the flow		

Table 4: Key points of the transition scenario found. * denotes conjectures.

6 Discussion

In the present chapter the results are recapitulated and discussed in the context of existing literature on curved pipe flow transition. The generalizable character of the experimental setup and the findings concerning transitional phenomena and critical Reynolds numbers is considered. Two possible mechanisms of the instability are contemplated. Open questions and topics for possible future research are highlighted.

6.1 Comparison with existing publications

The results presented in the previous chapter have been obtained for a toroidal tube of aspect ratio $A_r = 20.26$. A steady, laminar basic flow at low Reynolds numbers, a supercritical transition to a flow of a single frequency at Re_{c1}, a (presumably) quasi-periodic flow above Re_{c2} and finally a transition to a turbulent state in the range of a not well defined Re_{c3} have been found. The measured friction factor has not indicated any obvious changes in the trend corresponding to these changes of state.

The results apply only to the special circumstances of the chosen setup though: a flow arising in a torus due to a rolling sphere which is driven by a magnet. And the rolling sphere does indeed cause a strong perturbation to the flow within a certain range of influence. Sec. 5.2 gave strong support that at a sufficient distance to the actuator the flow can actually be regarded as independent of the drive and hence treated as practically fully developed flow through a curved tube. The only constraint to this generalization comes from a minor deviation of up to 7% regarding the top-bottom symmetry of the in-plane (but not the streamwise) velocity, whose origin is not yet completely clear. As this minor deviation might nevertheless play a role concerning the stability properties of the flow it can not be ignored. However, a comparison of the (mean) velocity profiles presented in sec. 5.3 and the measured friction factor (sec. 5.6) with existing publications has brought high accordance and hence further support for the generalizability of the results. The universal character of the findings concerning transitional phenomena and critical Reynolds numbers has yet to be considered though. This will also shed light on the issue of the adequacy of the present experimental setup, yielding a flow through a torus, as a general model for curved pipe flow configurations.

As already mentioned in sec. 2.3.4, most correlations for the critical Reynolds or Dean number for transition in curved pipes were based on empirical relations found in friction factor measurements. The exemplary selection shown in table 2 showed that there is rather poor agreement amongst the various correlations published concerning critical Reynolds numbers serving as distinct thresholds. Most striking is the fact that the critical Reynolds number Re_{c1} identified in the previous chapter is considerably below any of the critical thresholds provided in table 2. The critical Reynolds number Re_{c3} for transition to a notably turbulent state, roughly found to be located in the range $6000 \leq \mathrm{Re} \leq 9000$ (sec. 5.5), corresponds much better to the still vast range of table 2.

The main reason for these discrepancies is the continuous transition scenario concerning pressure drop and turbulent properties. In configurations characterized by the presence of secondary

flow, pressure drop is largely caused by recirculation and may be significantly higher than in parallel flow also under stationary laminar conditions; the appearance of unsteadiness, and even of turbulence, results in an added frictional term which increases gradually with the Reynolds number and, in low-turbulence flows, may represent just a minor contribution to the overall pressure drop (Piazza & Ciofalo 2011). As the friction factor does not exhibit any obvious change in the trend in correspondence with neither $\mathrm{Re}_{c\,1}$ or $\mathrm{Re}_{c\,2}$ nor for the transition to turbulent flow (see sec. 5.6), the overall dissipation in the flow does not seem to be influenced substantially by those unsteady phenomena. Practical working definitions of a laminar and a turbulent regime for e.g. engineering applications based on the friction factor seem to rely on a great deal of judgement and arbitrary definition. They are hence certainly acceptable, but a proper definition and description of transition in curved pipes based on the friction factor seems futile.

Considering the present results concerning critical thresholds and bifurcation scenarios, only the works of Sreenivasan & Strykowski (1983), Webster & Humphrey (1993, 1997) and Piazza & Ciofalo (2011) can serve for comparative purposes. All these publications agree on the fact that the loss of stability of the basic steady flow occurs in the range $4000 \leq \mathrm{Re} \leq 6000$ for the respective curvature ratios investigated. These values are lower than the values predicted by the correlations in table 2. By trend they also all agree on a scenario of subsequent bifurcations via a periodic state of the flow.

The mainly qualitative observations of Sreenivasan & Strykowski (1983) show good agreement with the present findings, as their hot-wire traces (fig. 10) qualitatively coincide. Near the inside wall they found *a selected frequency to grow to a fairly large amplitude before higher harmonics started to appear* (quoted verbatim from Sreenivasan & Strykowski (1983); the term *higher harmonics* seems to be improperly used, as they probably meant *additional* frequencies and not *higher harmonics* in the sense of $2f$, $3f$ etc., which could only have been detected in the frequency spectra). Fig. 10 shows a slight unsteadiness of the signal already at $\mathrm{Re} = 4200$. At $\mathrm{Re} = 5000$ the single selected frequency is clearly seen.

It is important to recall that the hot wire traces were taken in the *horizontal midplane* of the cross section in a small distance (about $0.25a$) from the inner and outer wall respectively of a curved pipe. As the present investigation has shown (see especially fig. 50), these points are not well suited to detect the modulation of the streamwise velocity as an indicator for the first instability. It is, therefore, not surprising that Sreenivasan & Strykowski (1983) find only a slight unsteadiness at $\mathrm{Re} = 4200$. As their aspect ratio of $A_r = 17.2$ is not too far from the present one the conjecture, that the deviation would have been more distinct if it had been measured at the center of region 1, seems admissible. It is very likely that the first critical Reynolds number in their experiments is very close to Re_{c1} of the present case. Furthermore, as Sreenivasan & Strykowski (1983) did not analyze the frequency spectra it is possible that for $\mathrm{Re} = 5000$ they actually did not observe only a single selected frequency but in fact presented measurements of already the next instability, i.e. the presumably quasi-periodic flow. This is further supported by the small 'burst' at $\mathrm{Re} = 5000$ appearing in the middle of the time interval shown for the hot wire trace placed $0.25a$ from the outer wall. Sec. 5.5 has shown that the second instability produces such irregular 'bursts' in consequence of irregular breakdowns of the

top-bottom symmetry above Re_{c2}.

In good agreement with the present results the traces at $\text{Re} = 5870$ and $\text{Re} = 6730$ show higher and higher frequencies appear in a relatively short span of Reynolds numbers and the formation and coalescence of 'bursts' of high-frequency turbulence near the outer wall. As the results of Sreenivasan & Strykowski (1983) are presented without quantitative values for e.g. wavelengths and amplitudes no further comparison is possible.

Webster & Humphrey (1993) made experimental observations of a nominally fully developed flow through a helically coiled pipe with an aspect ratio of $A_r = 18.2$, i.e. even closer to the one of the present work. They presented *midplane* velocity profiles of the mean and RMS values of two velocity components, measured by means of laser-Doppler velocimetry. In the range $5060 \leq \text{Re} \leq 6330$ they found periodic flow oscillations with nondimensional frequencies $\hat{f} = 0.25$ and 0.5 in the inner half of the pipe cross section and related them to a traveling-wave instability.

From (30), the linear fit for $\hat{f}$, the values of Webster & Humphrey (1993) correspond very well with the present findings (equation (30) gives $\hat{f} = 0.32$ for $\text{Re} = 5060$ and $\hat{f} = 0.15$ for $\text{Re} = 6330$, both very close to 0.25). They did not report a decrease but only two constant values independent of Re. What they call 'frequency doubling phenomenon' from $\hat{f} = 0.25$ to 0.5, found near the center of the pipe, is easily explained by the appearance of a second harmonic as also detected and clearly demonstrated in the present results (see especially fig. 55).

It is important to note that Webster & Humphrey (1993), in contrast to Sreenivasan & Strykowski (1983), used a 'flow straightener' (packed soda straws) and a straight entrance section in the upstream straight pipe of the helical coil. They hence had a laminar flow as inlet condition to the helical pipe section, while Sreenivasan & Strykowski (1983) had an undefined inlet condition. Based on the short references to that topic provided in the text it can be assumed they had at least intermittently turbulent flow above $\text{Re} \sim 3000$. In other words: while Webster & Humphrey (1993) had a more or less fully developed laminar Hagen-Poiseuille profile as inlet condition and did not trigger any perturbation to the flow in the helical section, Sreenivasan & Strykowski (1983) had a rather not well defined state of (probably intermittent) low turbulence at the beginning of the coiled section. The low turbulence inlet condition corresponds much better to the perturbed boundary condition due to the actuator of the current setup. The fact, that Webster & Humphrey (1993) find Re_{c1} to be 5060, i.e. well above Sreenivasan & Strykowski (1983) and the present results, must therefor be due to the different inlet conditions. The fact that Webster & Humphrey (1993) find only constant values for $\hat{f}$ will be considered further below.

As already mentioned in sec. 2.3.6, a few years later Webster & Humphrey (1997) supplemented their LDV measurements with complementary flow visualization photographs and numerical calculations, providing estimates of the wavelength and wave speed of the traveling wave instability. They specified a λ of $18.4°$ for $\text{Re} = 5060$. At this Reynolds number the present investigation could not find an identifiable single wavelength anymore (see sec. 5.1). The (varying) λ of $11.25° - 22.5°$ found in the Reynolds number range $4400 \leq \text{Re} \leq 5050$ is in very good agreement with Webster & Humphrey (1997). However, their wave phase speed of $c = 0.825U$

differs considerably to the one found in the present investigation ($c \sim 1.12U$). Yet again at different Reynolds numbers and hence not directly comparable.

The numerical calculations of Webster & Humphrey (1997) revealed many important aspects of the time-dependency of the flow field during one full wavelength, showing that the instability is most intense *off* the midplane and the maximum streamwise velocity fluctuation exactly located in the center of region 1. Though a comparison of the contours of the streamwise velocity during one wavelength (Webster & Humphrey (1997), fig. 7 with fig. 44 of the present work) differs slightly, this result was clearly proven by the present findings (see fig. 50).

When comparing the present results to Sreenivasan & Strykowski (1983) and Webster & Humphrey (1993, 1997) it is tacitly assumed that the small torsion of the helical winding does not significantly modify the basic flow. This assumption is supported by many previous works (see e.g. Berger et al. 1983). As Piazza & Ciofalo (2011) point out, neither a finite torsion nor a finite pipe length or even a departure from equilibrium conditions seems to modify too radically the basic phenomenology of curved pipe flow.

The only study known to the author dealing with transition to turbulence of a steady basic flow in a torus just as in the present work is the recent three-dimensional, time-dependent numerical simulation of Piazza & Ciofalo (2011). They investigated two curvatures of $\delta = 0.1$ and 0.3 in a Reynolds number range between 3500 and 14700 and found consecutive transitions from stationary to periodic, quasi-periodic and chaotic flow. At first sight these results seem to confirm the current findings. And the overall transition scenario is indeed found to be similar. However, in many important details the scenario differs considerably.

For $\delta = 0.3$, a value very different to the present investigation, and $4556 < \mathrm{Re} < 4605$ ($1441 < \mathrm{De} < 1456$) they report a supercritical Hopf bifurcation, giving rise to a traveling wave which takes the form of a varicose streamwise modulation of the Dean vortex ring intensity. The secondary Hopf bifurcation for $5042 < \mathrm{Re} < 5270$ led to a quasi-periodic flow characterized by two independent fundamental frequencies associated with distinct traveling waves. The first is described to be affecting mainly the Dean vortex rings and to be similar to that observed in purely periodic flow, the second to be localized mainly in the secondary flow boundary layers and manifesting itself as an array of oblique vortices produced at the edge of the Dean vortex regions. Both the periodic and the quasi-periodic regimes found were characterized by an instantaneous *anti-symmetry* of the oscillatory components with respect to the equatorial midplane of the torus.

For $\delta = 0.1$, a value much closer though still considerably different to the present investigation, Piazza & Ciofalo (2011) found a *direct transition from steady to quasi-periodic flow* between $5139 < \mathrm{Re} < 5208$ ($1625 < \mathrm{De} < 1647$) associated with *hysteresis*. Starting from the quasiperiodic solution and letting the Reynolds number decrease, they obtained both quasi-periodic and periodic stable solutions at Reynolds numbers below the critical value, suggesting the existence of a subcritical Hopf bifurcation followed by a secondary Hopf bifurcation. They found the traveling modes for $\delta = 0.1$ to be instantaneously symmetric with respect to the equatorial midplane of the torus.

A comparison of these results, of course under the restriction of considerably different cur-

vature ratios, to the present results (table 4) exhibits a rather poor accordance in most of the details. Neither the critical Dean numbers, the top-bottom symmetry for the quasi-periodic state nor the details of the transition scenario etc. can be confirmed or at least brought in line with the present experimental findings, as e.g. no hysteresis or direct transition from steady to quasi-periodic flow were found. In parts, e.g. concerning the sequence of bifurcations, the accordance is even higher with the case $\delta = 0.3$ than with $\delta = 0.1$. Although the present findings are no counterevidence to the results of Piazza & Ciofalo (2011) especially concerning $\delta = 0.1$ in the strict sense, they represent serious doubts to the admissibility of these results.

It is therefore noted that the present results are compatible with the (very few) published experimental and computational results, especially concerning the general features of transition in curved and helical pipes and the related scenarios. Since the data published is somewhat sparse a good part of the comparison is based on conjectures and more specific quantitative comparisons are mostly not possible. In details considerable deviation is found, only partly explainable by different experimental setups and conditions.

Summing up the findings the present experimental setup and the toroidal geometry used can be assessed as an adequate and appropriate model for curved pipe flows in general, yielding basically the same results as in open systems. A major source of deviation is the actuator, representing constant perturbation at the boundaries triggering transition. Furthermore the 2π–periodicity and the length of the actuator might play an important role in selecting or imposing certain precise wavelengths and wave speeds on the coherent structures.

6.2 Instability mechanism

The physical mechanism of the instability of the steady basic flow has not been addressed yet. Webster & Humphrey (1997) concluded from their results, that energy is transferred to the traveling wave from the basic flow through a complex interaction between the centripetal acceleration acting in the inner half of the pipe cross-section and the flow in the cross-stream wall layer. Taking for granted that the flow perturbation consists of a pair of counter-rotating vortices aligned in the cross-stream circumferential direction they suggested that the traveling wave is a result of a *centrifugal instability of the cross-stream flow* (distinct from the centrifugal force due to the streamwise velocity).

Based on an analysis of Rayleigh´s centrifugal stability criterion and their numerical results, Piazza & Ciofalo (2011) consider the Dean vortex regions as most likely candidates for the locus of origin of the first instability. They hence state that the transition from stationary to unsteady regimes is driven by a *centrifugal instability of the main (streamwise) flow located in the Dean vortex region, and not of the secondary flow.*

As the basic flow in toroidal direction is characterized by a strong shear gradient, small perturbations of the flow in poloidal direction lead to large fluctuations of the streamwise velocity. These fluctuations can be regarded as periodic streaks. The present work has shown that the perturbation flow is indeed strong near region 1. The perturbation arises in this region in the form of streamwise vortices. These vortices transport mean streamwise momentum, giving rise to strong streaks. Region 1 is most susceptible to streamwise vortices, as high gradients are present in the basic flow and these gradients are sufficiently away from the pipe wall. It is clear that the streamwise perturbation vortices drive the streaks, but from the present investigation the mechanism by which the streamwise vortices are maintained can not be unambiguously identified. Presumably, however, the streaks themselves are unstable and feed back on the streamwise vortices, very much like the regeneration mechanism suggested by Waleffe (1997) for transitional shear flows.

No direct evidence for a centrifugal instability mechanism is found. However, the instability builds on the particular primary flow structure which is a result of the centrifugally-induced secondary motion of the basic flow.

6.3 Traveling waves in pipe flow and analogies to other canonical flows

As this study has clearly shown, a *stable* traveling wave, representing a spatio-temporal periodic flow solution, arises through a bifurcation at a critical threshold in curved pipe flow. Such periodic solutions are stationary states when viewed from a frame translating with a constant phase speed (which depends on the wave structure) down the pipe and therefore represent the lowest rung in the hierarchy of phase space structures which could potentially be used to characterize mean properties of the flow either in the transitional or fully turbulent regime (Kerswell 2005). As stated in sec. 2.2 it has previously been shown that the dynamics in phase space of the turbulent state in shear flows depends on the existence of periodic orbits, representing traveling waves, which have first been found in plane Couette flow (Waleffe 1998, 2001, 2003) and, more recently, also in straight pipe flow (Faisst & Eckhardt 2003, Wedin & Kerswell 2004, Hof et al. 2004). On an increase of the Reynolds number in a straight pipe all periodic orbits (waves) are created by saddle-node bifurcations and they are all *unstable*. Very recent studies have shown a vast multitude of time-dependent solutions including spiralling, modulated-travelling, modulated-spiralling, doubly-modulated-spiralling and mildly chaotic waves in straight pipes (Pringle & Kerswell 2007, Pringle et al. 2008, Mellibovsky & Eckhardt 2011, 2012). Closely related transition scenarios have also been found in e.g. duct flow (Biau et al. 2008, Okino & Nagata 2012).

The present study provides strong support to a similar scenario of subsequent destabilization of the basic flow trough traveling wave solutions, finally leading to chaotic dynamics, as a succession of transitions leading from a simple traveling wave to chaotic time-dependence was found. The existence of the first traveling wave was clearly traced to the low turbulence regime (sec. 5.5). The main and very major difference to straight pipes is just the stabilization of traveling waves through the centrifugal forces induced by curvature. However, it is not yet clear how and if traveling wave solutions in curved and straight pipes interrelate.

The present findings also reveal striking analogies regarding the canonical Taylor–Couette flow (among countless others, see e.g. Fenstermacher et al. 1979, Di Prima & Swinney 1985, Andereck et al. 1986). In such a flow between concentric rotating cylinders two instabilities in the flow, namely from steady two-dimensional to time-independent Taylor vortex flow and then to time-dependent wavy vortex flow, have been known for long. Beyond the onset of wavy vortex flow, when the flow is strictly periodic, the velocity power spectra contain a single sharp frequency component and its harmonics. As the Reynolds number is increased, a second sharp frequency component appears, yielding a quasi-periodic flow. It is thus in both cases the equivalent scenario of a steady secondary flow (Dean vortices versus Taylor vortices) being destroyed by centrifugal instabilities and replaced by a periodic unsteady flow as the Reynolds number is increased. A full supercritical bifurcation sequence from stationary to periodic, then to quasi-periodic flow and finally to turbulence is observed both here and there.

Apart from Taylor–Couette flow also the transition to turbulence in e.g. the so-called lid-driven cavity is subject of countless publications (Shankar & Deshpande 2000, Albensoeder & Kuhlmann 2002). Common to all these flows is an ordered sequence of bifurca-

tions through which the flow becomes progressively more complicated in space and time.

Furthermore, it is interesting to consider the analogy to blood flow. For simplicity arterial bends are commonly modelled as helical and/or curved pipes (see e.g. Zabielski & Mestel 1998*a*, Alastruey et al. 2012). Although the details of blood flow are extremely complex (the arterial centerline is a curve with varying, non-uniform torsion as well as curvature; arteries have flexible walls and a lot of bends and bifurcations; the pulsatile flow is driven by the pumping action of the heart, causing a complex periodic time dependence; blood exhibits weakly non-Newtonian behavior at low shear rates etc.) there is a strong qualitative similarity between blood flow and flow through curved pipes in general. It is noteworthy that in the circulatory systems of humans and smaller mammals blood flow is mostly laminar (Pedley 1995).

In addition to the well-known similarities concerning the overall flow structure of blood flow and flow through curved and helical pipes, the present results regarding the first instability in the torus flow suggest a further interesting connection. As Ku (1997) points out, Reynolds numbers in blood flow are on the order of 4000 at peak systole. This alone does not define the Dean numbers. It is interesting to note though that the quoted 'order of 4000' is close to the value Re_{c1} found in the present case, where the flow is becoming distinctly periodic. In blood flow the periodic time dependence comes (mainly?) from the pumping action of the heart, while in curved pipe flow the periodicity appears due to the first instability. The flow regimes in terms of Reynolds numbers seem to overlap. Furthermore, the frequencies found in the present investigation seem to be strikingly close to the frequency of the cardiac cycle, namely the typical resting heart rate (heartbeats) in adults, which is 60-90 beats per minute (bpm) or 1-1.5 Hz. With water as fluid the frequency found at Re_{c1} was in the range of 1.6 Hz in the present experimental setup.

As blood is reported to exhibit viscosities considerably higher than water (in dependence of the diameter of the artery) more information on the actual Dean numbers and nondimensional frequencies in arteries would be needed in order to shed light on a possible cross-connection between the periodicity due to the first instability and the periodicity of the cardiac cycle. Furthermore, the time-dependent flux might render the flow too different to be compared to constant mass flux. It can be suspected, however, that the first instability and the range of transitional flow is at least partially met during the cardiac cycle and the respective instabilities hence indeed appear in blood flow.

6.4 Future research and open questions

The present results open up the way for numerous further investigations. It is hereby assumed to be established and proven that the introduced experimental setup can be deployed as yet another standard system. The relatively simple geometry facilitates the experimental exploration of the transitional phenomena. In addition, the comparison of results from experiments and calculations is quite simple. The setup replicates periodic boundary conditions which are the natural choice for numerical simulations, and a combination of experimental and theoretical techniques (numerical simulation) strongly supports the mutual validation.

The present work has explored well the range of the first instability and its main characteristics. For the higher transitional range above $\mathrm{Re}_{c\,2}$ many topics are yet to be explored and illuminated. A more detailed statistical analysis of the respective ranges will shed light on the actual transition to the ultimate chaotic regime of turbulence. Fully developed turbulent curved-pipe flow, which emerges above the transition range of Reynolds numbers, has not been in the focus of the experimental investigations at all. It should be noted, however, that the current setup is very easily adaptable to measure turbulence quantities as well in future experiments. Single-point statistics including mean velocity, root-mean-square (RMS) of the streamwise and wall-normal velocities, Reynolds stress, and vorticity can be obtained with LDA measurements, while multi-point statistics can be obtained with PIV measurements. There is no substantial reason why the experimental setup, after some adjustments regarding motor, gear ratio, magnetic force etc. would not work for Reynolds numbers up to 100.000 or more.

Apart from investigating the regime of higher Reynolds numbers, the variation of the curvature ratio is a logical next step to better explore the influence of curvature on the transitional process. Preliminary tests with a torus of $\delta = 0.1$, the results of which have not found their way into the present work, indicated to also work well. The usable range, within which the flow can be considered fully developed (see sec. 5.2.1) is of course considerably reduced. Investigations of even stronger curvature might hence be limited in their viability. At the same time investigations in the other direction, i.e. investigations of tori with curvature towards zero, are technically only limited by producibility and manufacturability. A δ of 0.01, at the same diameter as used here, seems well within reach. The tube could – instead of machining it out of single plexiglas plates on a turning lathe – be patched of several parts which are then mounted on a support structure. In any case, however, the production on a turning lathe can be used for smaller diameter tubes. Investigations of $\delta \to 0$ would definitely yield very interesting results.

Another open question is the exact role of the length and design type of the actuator in selecting certain wavelengths and wave speeds of the coherent structures. The boundary condition of imposing constant perturbation to the flow and its exact nature would be worth of increased attention as well.

Furthermore, it would be interesting to apply the principle used in the present setup to drive the flow in other geometries. As theoretically many different kinds of toroids can be obtained by revolving a plane geometrical figure about an axis external to that figure which is parallel to the plane of the figure and does not intersect the figure, e.g. a toroid consisting of a square

curved tube is an obvious possibility. It would not be too much effort to produce and realize such a geometry for an experiment. The solution of using a plunger (see sec. 4.4.2) instead of a sphere to drive the flow provides a feasible solution.

As described in sec. 3.2.4, the setup can be equipped with highly accurate pressure transducers. Within the present investigations the pressure holes were only located at the top of the upper side of the tube ($\alpha = \pi$). With some modifications of the setup the pressure (drop) could also be measured at various small pressure holes at the pipe wall for $\alpha \neq \pi$. It would certainly be interesting to measure pressure differences between two different radial positions, i.e. within the same cross section, during one full wavelength λ. Only the location of the seals and the need to place a – with respect to the plexiglas plates – inclined bore is rendering such modifications a little tricky.

As the flow in the torus is driven by means of a torque which must balance the friction along the pipe wall, high precision torque measurements could be an interesting addition and complement to the pressure drop measurements. As e.g. Zimmerman et al. (2011) in turbulent, rotating spherical Couette flow or Lathrop et al. (1992) and Lim & Tan (2004) in Taylor–Couette flow, investigations of the torque scaling as a function of the Reynolds number in the torus flow may yield further insights into the transitional process and the relation of wall shear stress and its time derivative to global torque measurements. The torque required to maintain constant velocity in the torus flow will provide a global picture of angular momentum transport and power dissipation. Initial tests with the present setup, using estimates of the motor torque from electrical current measurements, have not yet brought any satisfactory results due to low accuracy (see Schiebel 2012). Highly sensitive, calibrated strain-gauge torque sensors would be needed for exact measurements. It could be, however, that the flow around and in the vicinity of the actuator and the resulting friction is too dominant compared to the bulk flow.

Coming back to the similarities between blood flow and flow through curved pipes, the drive of the present setup could rather easily be modified from a constant drive to a time-dependent drive. As the drive is a system consisting of controller unit and variable frequency motor with speedometer (see sec. 4.8), by setting an appropriate function for the drive the flow could also be driven periodically. The physiological pulse of the heart is characterized by a large peak in the first half of the time-cycle called systole and a fairly steady behavior in the second usually referred to as diastole (McDonald 1974, Zabielski & Mestel 1998b). Only the limited ability of the actuator to follow drastic velocity changes of the magnet might restrict such a velocity function. By means of a strong magnet and an exact control function for the drive the pulsatile pumping action of the heart and the blood flow through curved arteries might be mimicked.

Finally, as pointed out by Kerswell (2005), the most frequently quoted practical reason for studying transition to turbulence is the desire to delay or even prevent its onset, i.e. to *control* the flow. Turbulence control in pipe flow usually intends to reduce the skin-friction drag. Known strategies are based on influencing the flow on small and large scales, involving *passive* (e.g. Riblets, large eddy break-up devices, sinusoidal wavy walls, non-Newtonian additives) or *active* devices which need auxiliary power (e.g. local blowing or suction through the wall, spanwise wall oscillations, spatially or temporally oscillating spanwise-oriented Lorentz forces). Despite all

these efforts, neither an effective general-purpose control scheme nor a method that is sufficiently simple and robust exists. Reviews and approaches on the various techniques of turbulence control devised and implemented have been given, among many others, by Bushnell & McGinley (1989), Gad-el-Hak (1989, 1994, 1996, 2000), Fiedler & Fernholz (1990), Moin & Bewley (1994), Quadrio & Ricco (2004) and Quadrio et al. (2009).

An important result of these efforts is that turbulence in wall-bounded flows is primarily created and caused by organized structures. These structures provide a handle to turbulence control. As the existence of traveling waves is a necessary precursor (as Re increases) for transition to turbulence, this suggests concentrating on delaying their emergence or ideally eliminating them completely might enable control of the flow (Kerswell 2005). Hence control, i.e. systematic manipulation of the stable traveling waves in curved pipe flow, could be a promising field of activity.

In summary, a multitude of opportunities for future experimental research is opening up based on the current setup. Variations of the Reynolds number, the curvature ratio, the toroidal cross section, the drive and its velocity function, the type of the actuator etc. as well as the addition of further instrumentation and finally the large area of flow control offer plenty of space for further investigations.

7 Conclusions

A novel experiment which realizes a flow with precisely adjustable flow rate in a toroidal pipe was designed, set up, tested and put into operation. At the same time, the experimental set-up already provided the possibility for detailed investigations of transition to turbulence in curved pipe flow.

The facility is designed and optimized to investigate curved pipe flow by state-of-the-art non-intrusive measurement techniques at arbitrary Reynolds numbers. A quantitative evaluation of the novel experimental setup including considerations of the influence of the actuator, a comparison of velocity profiles acquired from different sources and an evaluation of the cross sectional flow field has been presented. Mean velocity profiles, especially for increasing Reynolds number, and investigations of the instantaneous flow field at the first instability and the respective large scale velocity fluctuations have been determined and described. The frequency spectrum has been analyzed. The first critical Reynolds number has been determined very accurately to be $\mathrm{Re}_{c\,1} = 4080 \pm 2\%$. The bifurcation scenario has been investigated and was found to be supercritical. Considerations of the flow field at higher Reynolds number, i.e. above the second critical Reynolds number ($\mathrm{Re}_{c\,2} \approx 4400$), were made. Finally the friction factor has been measured in the range of $1000 \leq \mathrm{Re} \leq 15.000$.

Although only a single value of the curvature ratio has been examined, the present investigation has shed light on many aspects of transition to turbulence in a curved pipe. A succession of transitions has been found, leading from a laminar, steady basic flow trough periodic and quasi-periodic flow subsequently to chaotic behavior. No previous experimental study has provided quantitative information on the subsequent regimes that precede turbulent flow and the flow field itself in curved pipes comparable in accuracy and extent.

The findings conclusively prove the present experimental setup and the toroidal geometry used as an adequate and appropriate model for curved pipe flows in general, yielding similar results as in open systems. The results acquired with the experimental setup concerning transitional phenomena were shown to be highly compatible with the (rather few) published experimental and computational results, especially regarding the general features of transition in curved and helical pipes and the related scenarios.

The simple geometry facilitates the exploration of transitional phenomena. In addition, the comparison of results from experiments and calculations is uncomplicated. As the experimental setup replicates periodic boundary conditions which are the natural choice for numerical simulations combination of experimental and theoretical techniques (numerical simulation), mutual validation is strongly supported and enabled. Hence, almost as an aside of the original objective of investigating transition to turbulence in curved pipe-flow, a novel experimental setup has been created bearing the potential for a benchmark problem.

References

Adler, M. (1934), 'Flow in curved tubes', *Z. Angew. Math. Mech.* **14**, 257–275.

Adrian, R. & Westerweel, J. (2011), *Particle Image Velocimetry*, Cambridge University Press.

Agrawal, Y., Talbot, L. & Gong, K. (1978), 'Laser anemometer study of flow development in curved circular pipes', *J. Fluid Mech.* **85**, 497–518.

Alastruey, J., Siggers, J. H., Peiffer, V., Doorly, D. J. & Sherwin, S. J. (2012), 'Reducing the data: Analysis of the role of vascular geometry on blood flow patterns in curved vessels', *Physics of Fluids* **24**, 031902.

Albensoeder, S. & Kuhlmann, H. C. (2002), 'Linear stability of rectangular cavity flows driven by anti-parallel motion of two facing walls', *Journal of Fluid Mechanics* **458**, 153–180.

Ali, S. (2001), 'Pressure drop correlations for flow through regular helical coil tubes', *Fluid Dyn. Res.* **28**, 295.

Allen, J., Shockling, M., Kunkel, G. & Smits, A. (2007), 'Turbulent flow in smooth and rough pipes', *Philosophical Transactions of the Royal Society A: Mathematical, Physical and Engineering Sciences* **365**(1852), 699–714.

Andereck, C. D., Liu, S. S. & Swinney, H. L. (1986), 'Flow regimes in a circular couette system with independently rotating cylinders', *Journal of Fluid Mechanics* **164**, 155–183.

Austin, L. R. & Seader, J. D. (1974), 'Entry region for steady viscous flow in coiled circular pipes', *AIChE J.* **20**, 820.

Avila, K., Moxey, D., de Lozar, A., Avila, M., Barkley, D. & Hof, B. (2011), 'The onset of turbulence in pipe flow', *Science* **333**(6039), 192–196.

Bandyopadhyay, P. R. (1986), 'Aspects of the equilibrium puff in transitional pipe flow', *J. Fluid Mech.* **163**, 439–458.

Bénard, H. (1900), 'Les tourbillons cellulaires dans une nappe liquide', *Revue Gén. Sci. Pur. Appl.* **11**, 1261–1271.

Benjamin, T. B. (1978*a*), 'Bifurcation phenomena in steady flows of a viscous fluid. i. Theory', *Proceedings of the Royal Society of London. A. Mathematical and Physical Sciences* **359**(1696), 1–26.

Benjamin, T. B. (1978*b*), 'Bifurcation phenomena in steady flows of a viscous fluid. ii. Experiments', *Proceedings of the Royal Society of London. A. Mathematical and Physical Sciences* **359**, 27–43.

Berger, S. A., Talbot, L. & Yao, L. S. (1983), 'Flow in curved pipes', *Annu. Rev. Fluid Mech.* **15**, 461–512.

Biau, D., Soueid, H. & Bottaro, A. (2008), 'Transition to turbulence in duct flow', *Journal of Fluid Mechanics* **596**, 133–142.

Bovendeerd, P. H. M., Steenhoven, A. A. V., Vosse, F. N. V. D. & Vossers, G. (1987), 'Steady entry flow in a curved pipe', *Journal of Fluid Mechanics* **177**, 233–246.

Buckingham, E. (1915), 'The principle of similitude', *Nature* **96**, 396–397.

Budwig, R. (1994), 'Refractive index matching methods for liquid flow investigations', *Experiments in Fluids* **17**, 350–355.

Bushnell, D. M. & McGinley, C. B. (1989), 'Turbulence control in wall flows', *Annu. Rev. Fluid Mech.* **21**, 1–20.

Chandrasekhar, S. (1961), *Hydrodynamic and Hydromagnetic Stability*, Oxford University Press, Oxford.

Cioncolini, A. & Santini, L. (2006), 'An experimental investigation regarding the laminar to turbulent flow transition in helically coiled pipes', *Experimental Thermal and Fluid Science* **30**(4), 367 – 380.

Colebrook, C. F. (1938), 'Turbulent flow in pipes with particular reference to the transition region between the smooth and rough pipe laws', *J. Inst. Civ. Eng.* **39**, 133.

Couette, M. M. (1890), 'Études sur la frottemont des liquides', *Ann. Chim. Phys.* **6**(Ser. 21), 433–510.

Dang, L., Wei, H., Wang, Z. & Yan, W. (2009), 'Solubility of ammonium thiocyanate in different solvents', *Journal of Chemical & Engineering Data* **54**, 1063–1064.

Darbyshire, A. G. & Mullin, T. (1995), 'Transition to turbulence in constant-mass-flux pipe flow', *J. Fluid Mech* **289**, 83–114.

Daskopoulos, P. & Lenhoff, A. M. (1989), 'Flow in curved ducts: bifurcation structure for stationary ducts', *Journal of Fluid Mechanics* **203**, 125–148.

Dean, W. R. (1927), 'Note on the motion of fluid in a curved pipe', *Philos. Mag.* **4**, 208–223.

Dean, W. R. (1928), 'The streamline motion of fluid in a curved pipe', *Philos. Mag.* **7**, 673–695.

del Pino, C., Hewitt, R. E., Clarke, R. J., Mullin, T. & Denier, J. P. (2008), 'Unsteady fronts in the spin-down of a fluid-filled torus', *Physics of Fluids* **20**(12), 124104.

Dennis, S. C. R. & Ng, M. (1982), 'Dual solutions for steady laminar flow through a curved tube', *Q. J. Mech. Appl. Math.* **35**, 305–324.

Dennis, S. C. R. & Riley, N. (1991), 'On the fully developed flow in a curved pipe at large dean number', *Proc. R. Soc. London, Ser. A* **434**, 473–478.

Di Prima, R. & Swinney, H. (1985), Instabilities and transition in flow between concentric rotating cylinders, *in* H. Swinney & J. Gollub, eds, 'Hydrodynamic Instabilities and the Transition to Turbulence', Vol. 45 of *Topics in Applied Physics*, Springer Berlin / Heidelberg, pp. 139–180.

Draad, A. A. & Nieuwstadt, F. T. M. (1998), 'The earth's rotation and laminar pipe flow', *Journal of Fluid Mechanics* **361**, 297–308.

Drazin, P. G. (2002), *Introduction to hydrodynamic stability*, Cambridge University Press, Cambridge.

Drazin, P. G. & Reid, W. H. (1981), *Hydrodynamic Stability*, Cambridge University Press, Cambridge.

Duggleby, A., Ball, K. S., Paul, M. R. & Fischer, P. F. (2007), 'Dynamical eigenfunction decomposition of turbulent pipe flow', *J. Turbulence* **8**, 1–24.

Durst, F., Melling, A. & Whitelaw, J. H. (1987), *Theorie und Praxis der Laser-Doppler-Anemometrie*, Braun-Verlag, Karlsruhe.

Durst, F., Ray, S., Unsal, B. & Bayoumi, O. A. (2005), 'The development lengths of laminar pipe and channel flows', *J. Fluids Eng.* **127**, 1154–1160.

Eckert, M. (2008), 'Turbulenz - ein problemhistorischer Abriss', *NTM Zeitschrift fuer Geschichte der Wissenschaften, Technik und Medizin* **16**, 39–71.

Eckert, M. (2010), 'The troublesome birth of hydrodynamic stability theory: Sommerfeld and the turbulence problem', *The European Physical Journal H* **35**, 29–51.

Eckhardt, B., Faisst, H., Schmiegel, A. & Schumacher, J. (2002), Turbulence transition in shear flows, *in* I. P. Castro, P. E. Hancock & T. G. Thomas, eds, 'Advances in Turbulence IX: Proceedings of the Ninth European Turbulence Conference', International Center for Numerical Methods in Engineering (CIMNE), Barcelona, pp. 701–708.

Eckhardt, B., Schneider, T. M., Hof, B. & Westerweel, J. (2007), 'Turbulent transition in pipe flow', *Annu. Rev. Fluid Mech.* **39**, 447–468.

Eckmann, J. (1981), 'Roads to turbulence in dissipative dynamical systems', *Reviews of Modern Physics* **53-4**, 643–654.

Eliahou, S., Tumin, A. & Wygnanski, I. (1998), 'Laminar-turbulent transition in poiseuille pipe flow subjected to periodic perturbation emanating from the wall', *J. Fluid Mech.* **361**, 333.

Eustice, J. (1910), 'Flow of water in curved pipes', *Proc. R. Soc. London, Ser. A* **84**, 107–118.

Eustice, J. (1911), 'Experiments of streamline motion in curved pipes', *Proc. R. Soc. London, Ser. A* **85**, 119–131.

Faisst, H. & Eckhardt, B. (2003), 'Traveling waves in pipe flow', *Phys. Rev. Lett.* **91**, 224502.

Faisst, H. & Eckhardt, B. (2004), 'Sensitive dependence on initial conditions in transition to turbulence in pipe flow', *J. Fluid Mech.* **504**, 343–352.

Fenstermacher, P. R., Swinney, H. L. & Gollub, J. P. (1979), 'Dynamical instabilities and the transition to chaotic taylor vortex flow', *Journal of Fluid Mechanics* **94**(01), 103–128.

Fiedler, H. E. & Fernholz, H. (1990), 'On management and control of turbulent shear flows', *Prog. Aerospace Science* **27**, 305.

Foote, H. W. (1921), 'Equilibrium in the system ammonia: Water: Ammonium thiocyanate.', *Journal of the American Chemical Society* **43**, 1031–1038.

Gad-el-Hak, M. (1989), 'Flow control', *Appl. Mech. Rev.* **42**, 10.

Gad-el-Hak, M. (1994), 'Interactive control of turbulent boundary layers: a futuristic overview', *AIAA J.* **32**(9), 1753.

Gad-el-Hak, M. (1996), 'Modern developments in flow control', *Appl. Mech. Rev.* **49**, 365.

Gad-el-Hak, M. (2000), *Flow Control: Passive, Active, and Reactive Flow Management*, Cambridge University Press, London.

Germano, M. (1982), 'On the effect of torsion in helical pipe flow', *J. Fluid Mech.* **125**, 1–8.

Germano, M. (1989), 'The dean equations extended to a helical pipe flow', *J. Fluid Mech.* **203**, 289–305.

Goldstein, R. J. (1996), *Fluid mechanics measurements*, Taylor and Francis, Philadelphia.

Guan, X. & Martonen, T. B. (2000), 'Flow transition in bends and applications to airways', *J. Aerosol Sci.* **31**, 831.

Gupta, R., Wanchoo, R. K. & Jafar Ali, T. R. M. (2011), 'Laminar flow in helical coils: A parametric study', *Industrial & Engineering Chemistry Research* **50**(2), 1150–1157.

Hamilton, J. M., Kim, J. & Waleffe, F. (1995), 'Regeneration mechanisms of near-wall turbulence structures', *J. Fluid Mech.* **287**, 317–348.

Hasson, D. (1955), 'Streamline flow resistance in coils', *Res. Corresp.* **1**, 1.

Hewitt, R. E., Hazel, A. L., Clarke, R. J. & Denier, J. P. (2011), 'Unsteady flow in a rotating torus after a sudden change in rotation rate', *Journal of Fluid Mechanics* **688**, 88–119.

Hof, B., de Lozar, Kuik, D. J. & Westerweel, J. (2008), 'Repellor or attractor? selecting the model for the onset of turbulence in pipe flow', *Phys. Rev. Lett.* **101**, 214501.

Hof, B., Juel, A. & Mullin, T. (2003), 'Scaling of the turbulence transition threshold in a pipe', *Phys. Rev. Lett.* **91**, 244502.

Hof, B., van Doorne, C. W. H., Westerweel, J., Nieuwstadt, F. T. M. & Faisst, H. (2004), 'Experimental observation of nonlinear traveling waves in turbulent pipe flow', *Science* **305**, 1594–1598.

Hopkins, L. M., Kelly, J. T., Wexler, A. S. & Prasad, A. K. (2000), 'Particle image velocimetry measurements in complex geometries', *Experiments in Fluids* **29**, 91–95.

Humphery (1977), 'Numerical calculations of developing laminar flow in pipes of arbitrary curvature radius', *Can. J. Chem. Eng.* **56**, 151.

Hüttl, T. J. & Friedrich, R. (2000), 'Influence of curvature and torsion on turbulent flow in helically coiled pipes', *Int. J. Heat Fluid Flow* **21**, 345–353.

Hüttl, T. J. & Friedrich, R. (2001), 'Direct numerical simulation of turbulent flows in curved and helically coiled pipes', *Comput. Fluids* **30**, 591–605.

Hüttl, T., Wagner, C. & Friedrich, R. (1999), 'Navier-Stokes solutions of laminar flows based on orthogonal helical coordinates', *International Journal for Numerical Methods in Fluids* **29**(7), 749–763.

Iooss, G. & Joseph, D. D. (1997), *Elementary stability and bifurcation theory*, Springer New York.

Ito, H. (1959), 'Friction factors for turbulent flow in curved pipes', *J. Basic Eng. Trans. ASME* **81**, 123–134.

Ito, H. (1987), 'Flow in curved pipes', *JSME International Journal* **30**, 543–552.

Jayanti, S. & Hewitt, G. F. (1992), 'A numerical study of bifurcation in laminar flow in curved ducts', *International Journal for Numerical Methods in Fluids* **14**(3), 253–266.

Jeong, J. & Hussain, F. (1995), 'On the identification of a vortex', *Journal of Fluid Mechanics* **285**, 69–94.

Kelvin, L. W. (1871), 'Hydrokinetic solutions and observations', *Phil. Mag.* **42**, 362–377.

Kerswell, R. R. (2005), 'Recent progress in understanding the transition to turbulence in a pipe', *Nonlinearity* **18**, R17.

Kestin, J., Sokolov, M. & Wakeham, W. A. (1978), 'Viscosity of liquid water in the range -8°c to 150°c', *J. Phys. Chem. Ref. Data* **7**, 941–948.

Kovacs, K. (2012), 'Druckverlustmessungen am Torus', Bachelor thesis, Institute of Fluid Mechanics and Heat Transfer, Vienna University of Technology.

Ku, D. (1997), 'Blood flow in arteries', *Annual Review of Fluid Mechanics* **29**, 399–434.

Kubair, V. & Varrier, C. B. S. (1961), 'Pressure drop for liquid flow in helical coils', *Trans. Indian Inst. Chem. Eng.* **14**, 93.

Kuhlmann, H. (2010), 'Hydrodynamische Stabilität. Skript zur Vorlesung'.

Kuik, D. J., Poelma, C. & Westerweel, J. (2010), 'Quantitative measurement of the lifetime of localized turbulence in pipe flow', *J. Fluid Mech.* **645**, 529–539.

Lathrop, D. P., Fineberg, J. & Swinney, H. L. (1992), 'Transition to shear-driven turbulence in couette-taylor flow', *Phys. Rev. A* **46**, 6390–6405.

Lim, T. T. & Tan, K. S. (2004), 'A note on power-law scaling in a Taylor–Couette flow', *Physics of Fluids* **16**(1), 140–144.

Lin, C. X. & Ebadian, M. A. (1999), 'The effects of inlet turbulence on the development of fluid flow and heat transfer in a helically coiled pipe', *Int. J. Heat Mass Transfer* **42**, 739.

Liu, S. & Masliyah, J. H. (1993), 'Axially invariant laminar flow in helical pipes with a finite pitch', *J. Fluid Mech.* **251**, 315–353.

Lowe, M. L. & Kutt, P. H. (1992), 'Refraction through cylindrical tubes', *Experiments in Fluids* **13**, 315–320.

Lugt, H. J. (1979), *Wirbelstroemung in Natur und Technik*, G. Braun, Karlsruhe.

Madden, F. N. & Mullin, T. (1994), 'The spin-up from rest of a fluid-filled torus', *J. Fluid Mech.* **265**, 217–244.

McConalogue, D. J. & Srivastava, R. S. (1968), 'Motion of a fluid in a curved tube', *Proc. R. Soc. London, Ser. A* **307**, 37.

McDonald, D. A. (1974), *Blood Flow in Arteries*, Southampton: The Camelot Press Ltd.

McKeon, B. J., Zagarola, M. V. & Smits, A. J. (2005), 'A new friction factor relationship for fully developed pipe flow', *Journal of Fluid Mechanics* **538**, 429–443.

Mellibovsky, F. & Eckhardt, B. (2011), 'Takens-bogdanov bifurcation of travelling-wave solutions in pipe flow', *Journal of Fluid Mechanics* **670**, 96–129.

Mellibovsky, F. & Eckhardt, B. (2012), 'From travelling waves to mild chaos: a supercritical bifurcation cascade in pipe flow', *Journal of Fluid Mechanics* **709**, 149–190.

Mishra, P. & Gupta, S. N. (1979), 'Momentum transfer in curved pipes 1. newtonian fluids; 2. non-newtonian fluids', *Ind. Eng. Chem. Process Des. Dev.* **18**, 130.

Moehlis, J., Faisst, H. & Eckhardt, B. (2004), 'A low-dimensional model for turbulent shear flows', *New J. Phys.* **6**, Art. 56.

Moin, P. & Bewley, T. (1994), 'Feedback control of turbulence', *Appl. Mech. Rev.* **47**, 3–13.

Moody, L. F. (1944), 'Friction factors for pipe flow', *Trans. ASME* **66**, 671.

Mullin, T. (1993), *The nature of chaos*, Oxford Univ. Press, Oxford.

Mullin, T. (2011), 'Experimental studies of transition to turbulence in a pipe', *Annual Review of Fluid Mechanics* **43**(1), 1–24.

Mullin, T. & Peixinho, J. (2006), 'Transition to turbulence in pipe flow', *J. Low Temp. Phys.* **145**, 75.

Nandakumar, K. & Masliyah, J. H. (1982), 'Bifurcation in steady laminar flow through curved tubes', *J. Fluid Mech.* **119**, 475–490.

Naphon, P. & Wongwises, S. (2006), 'A review of flow and heat transfer characteristics in curved tubes', *Renewable Sustainable Energy Rev.* **10**, 463–490.

Newhouse, S., Ruelle, D. & Takens, F. (1978), 'Occurrence of strange axiom A attractors near quasi periodic flows on t^m, $m \geq 3$', *Communications in Mathematical Physics* **64**, 35–40.

Nikitin, N. V. (1994), 'Direct numerical modeling of three-dimensional turbulent flows in pipes of circular cross section', *Fluid Dyn.* **29**, 749–758.

Nikuradse, J. (1933), 'Strömungsgesetze in rauhen Rohren', *VDI-Forsch.-Heft* **361**, 1–22.

Okino, S. & Nagata, M. (2012), 'Asymmetric travelling waves in a square duct', *Journal of Fluid Mechanics* **693**, 57–68.

Panzer, L. (2012), 'Torus Flow - Ermittlung der Rahmenbedingungen des Versuchsaufbaus', Bachelor thesis, Institute of Fluid Mechanics and Heat Transfer, Vienna University of Technology.

Patankar, S. V., Pratap, V. S. & Spalding, D. B. (1974), 'Prediction of laminar flow and heat transfer in helically coiled pipes', *J. Fluid Mech.* **62**, 539–551.

Patankar, S. V., Pratap, V. S. & Spalding, D. B. (1975), 'Prediction of turbulent flow in curved pipes', *J. Fluid Mech.* **67**, 583–595.

Pedley, T. (1995), *Fluid Mechanics of Large Blood Vessels*, Cambridge University Press.

Peixinho, J. & Mullin, T. (2006), 'Decay of turbulence in pipe flow', *Phys. Rev. Lett.* **96**, 094501.

Piazza, I. D. & Ciofalo, M. (2011), 'Transition to turbulence in toroidal pipes', *Journal of Fluid Mechanics* **687**, 72–117.

Prasad, A. K. (2000), 'Stereoscopic particle image velocimetry', *Experiments in Fluids* **29**, 103–116.

Pringle, C. C. T., Dugyuet, Y. & Kerswell, R. R. (2008), 'Highly-symmetric travelling waves in pipe flow', *Philos. Trans. R. Soc. Lond. Ser. A* **367**, 457.

Pringle, C. C. T. & Kerswell, R. R. (2007), 'Asymmetric, helical, and mirror-symmetric traveling waves in pipe flow', *Phys. Rev. Lett.* **99**, 074502–1–074502–4.

Quadrio, M., Auteri, F., Baron, A., Belan, M. & Bertolucci, A. (2009), Experimental assessment of turbulent drag reduction by wall traveling waves, *in* B. Eckhardt, ed., 'Advances in Turbulence XII', Vol. 132 of *Springer Proceedings in Physics*, Springer Berlin Heidelberg, pp. 657–660.

Quadrio, M. & Ricco, P. (2004), 'Critical assessment of turbulent drag reduction through spanwise wall oscillations', *J. Fluid Mech.* **521**, 251–271.

Raffel, M., Willert, C., Wereley, S. & Kompenhans, J. (2007), *Particle Image Velocimetry: A Practical Guide*, Springer-Verlag.

Rayleigh, L. (1879), 'On the instability of jets', *Proc. London Math. Soc.* **10**, 4–13.

Rayleigh, L. (1880), 'On the stability, or instability, of certain fluid motions', *Proc. London Math. Soc.* **11**, 57–70.

Reynolds, O. (1883), 'An experimental investigation of the circumstances which determine whether the motion of water shall be direct or sinuous and of the law of resistance in parallel channels', *Philos. Trans. R. Soc. Lond. Ser. A* **174**, 935.

Romeo, E., Royo, C. & Monzon, A. (2002), 'Improved explicit equations for estimation of the friction factor in rough and smooth pipes', *Chem. Eng. J.* **86**, 369.

Ruck, B. (1990), *Laser-Doppler-Anemometrie, Berührungslose opt. Strömungsgeschwindigkeitsmesstechnik*, AT-Fachverlag, Stuttgart.

Schiebel, A. (2012), 'Transition einer Strömung durch ein gebogenes Rohr', Bachelor thesis, Institute of Fluid Mechanics and Heat Transfer, Vienna University of Technology.

Schmid, P. J. & Henningson, D. S. (1994), 'Optimal energy growth in Hagen-Poiseuille flow', *J. Fluid Mech.* **277**, 197–225.

Schmid, P. J. & Henningson, D. S. (2001), *Stability and Transition in Shear Flows*, Vol. 142 of *Appl. Math. Sci.*, Springer, New York,Berlin.

Schwab, M. (2011), 'Numerical investigations on a curved pipe flow', Bachelor thesis, Institute of Fluid Mechanics and Heat Transfer, Vienna University of Technology.

Schwegel, M. (2012), 'Optimierung des Torus Flow', Bachelor thesis, Institute of Fluid Mechanics and Heat Transfer, Vienna University of Technology.

Shankar, P. N. & Deshpande, M. D. (2000), 'Fluid mechanics in the driven cavity', *Annual Review of Fluid Mechanics* **32**(1), 93–136.

Shockling, M. A., Allen, J. J. & Smits, A. J. (2006), 'Roughness effects in turbulent pipe flow', *Journal of Fluid Mechanics* **564**, 267–285.

Siggers, J. H. & Waters, S. L. (2005), 'Steady flows in pipes with finite curvature', *Physics of Fluids* **17**, 077102.

Singh, M. P. (1974), 'Entry flow in curved pipes', *J. Fluid Mech.* **65**, 517.

Spurk, J. H. (1992), *Dimensionsanalyse in der Stroemungslehre*, Springer-Verlag, Darmstadt.

Sreenivasan, K. R. & Strykowski, P. J. (1983), 'Stabilization effects in flow through helically coiled pipes', *Exp. Fluids* **1**, 31–36.

Srinivasan, P. S., Nandapurkar, S. S. & Holland, F. A. (1968), 'Pressure drop and heat transfer in coils', *Chem. Eng.* p. 113.

Taylor, G. I. (1923), 'Stability of a viscous liquid contained between two rotating cylinders', *Philos. Trans. R. Soc. London, Ser. A* **223**, 289.

Taylor, G. I. (1929), 'The criterion for turbulence in curved pipes', *Proc. Roy. Soc. London A* **124**, 243–249.

Taylor, G. I. (1938), 'The spectrum of turbulence', *Proc. R. Soc. Lond. A* **164**, 476–490.

Trefethen, L. N., Trefethen, A. E., Reddy, S. C. & Driscoll, T. A. (1993), 'Hydrodynamic stability without eigenvalues', *Science* **261**, 578.

Tritton, D. J. (1988), *Physical Fluid Dynamics*, Oxford University Press.

Tropea, C., Yarin, A. L. & Foss, J. F. (2007), *Springer handbook of experimental fluid mechanics*, Springer Verlag, Berlin Heidelberg.

van Doorne, C. W. H. (2004), Stereoscopic PIV on transition in pipe flow, PhD thesis, Technische Universiteit Delft.

van Doorne, C. W. H. & Westerweel, J. (2007), 'Measurement of laminar, transitional and turbulent pipe flow using stereoscopic-PIV', *Exp. Fluids* **42**, 259–279.

van Heijst, G., Molenaar, D. & Clercx, H. (2004), Ruelle-Takens scenario in a confined two-dimensional flow, *in* 'APS Division of Fluid Dynamics Meeting Abstracts', p. 8.

Vashisth, S., Kumar, V. & Nigam, K. D. P. (2008), 'A review on the potential applications of curved geometries in process industry', *Industrial & Engineering Chemistry Research* **47**(10), 3291–3337.

von Helmholtz, H. (1868), 'Ueber discontinuirliche Fluessigkeits-Bewegungen', *Monatsber. Koenigl. Preuss. Akad. Wiss. Berlin* **23**, 215–228.

Waleffe, F. (1997), 'On a self-sustaining process in shear flows', *Phys. Fluids* **9**, 883.

Waleffe, F. (1998), 'Three-dimensional coherent states in plane shear flows', *Phys. Rev. Lett.* **81**, 4140.

Waleffe, F. (2001), 'Exact coherent structures in channel flow', *J. Fluid Mech.* **435**, 93.

Waleffe, F. (2003), 'Homotopy of exact coherent structures in plane shear flows', *Phys. Fluids* **15**, 1517.

Ward-Smith, A. (1980), 'Internal fluid flow - the fluid dynamics of flow in pipes and ducts', *NASA STI/Recon Technical Report A* **813**, 248.

Weast, R. C. & Astle, M. J. (1988), *CRC handbook of chemistry and physics*, CRC Press.

Webster, D. R. & Humphrey, J. A. C. (1993), 'Experimental observation of flow instability in a helical coil', *Journal of Fluids Engineering* **115**(3), 436–443.

Webster, D. R. & Humphrey, J. A. C. (1997), 'Traveling wave instability in helical coil flow', *Physics of Fluids* **9**, 407–418.

Wedin, H. & Kerswell, R. R. (2004), 'Exact coherent structures in pipe flow: traveling wave solutions', *J. Fluid Mech.* **508**, 333–371.

Westerweel, J. (1993), *Digital Particle Image Velocimetry - Theory and Application*, Delft University Press.

White, C. M. (1929), 'Streamline flow through curved pipes', *Proc. Roy. Soc. London A* **123**, 645–663.

Wieneke, B. (2005), 'Stereo-PIV using self-calibration on particle images', *Experiments in Fluids* **39**, 267–280.

Williams, G. S., Hubbell, C. W. & Fenkell, G. H. (1902), 'Experiments at detroit, michigan on the effect of curvature on the flow of water pipes', *Trans. Am. Soc. Civ. Eng.* **47**, 1.

Wygnanski, I. J. & Champagne, F. H. (1973), 'On transition in a pipe. Part 1. The origin of puffs and slugs and the flow in a turbulent slug', *J. Fluid Mech.* **59**, 281–335.

Wygnanski, I. J., Sokolov, M. & Friedman, D. (1975), 'On transition in a pipe. Part 2. The equilibrium puff', *J. Fluid Mech.* **69**, 283–304.

Yamamoto, K., Akita, T., Ikeuchi, H. & Kita, Y. (1995), 'Experimental studies of the flow in helical circular tube', *Fluid Dyn. Res.* **16**, 237.

Yamamoto, K., Aribowo, A., Hayamizu, Y., Hirose, T. & Kawahara, K. (2002), 'Visualization of the flow in a helical pipe', *Fluid Dyn. Res.* **30**, 251.

Yamamoto, K., Yanase, S. & Yoshida, T. (1994), 'Torsion effect on the flow in a helical pipe', *Fluid Dyn. Res.* **14**, 259.

Yanase, S., Goto, N. & Yamamoto, K. (1989), 'Dual solution of the flow through a curved tube', *Fluid Dyn. Res.* **5**, 191.

Yao, L. S. & Berger, S. A. (1975), 'Entry flow in curved pipes', *J. Fluid Mech.* **67**, 177–196.

Zabielski, L. & Mestel, A. J. (1998*a*), 'Steady flow in a helically symmetric pipe', *J. Fluid Mech.* **370**, 297–320.

Zabielski, L. & Mestel, A. J. (1998*b*), 'Unsteady blood flow in a helically symmetric pipe', *J. Fluid Mech.* **370**, 321–345.

Zikanov, O. Y. (1996), 'On the instability of pipe poiseuille flow', *Phys. Fluids* **8**, 2923.

Zimmerman, D. S., Triana, S. A. & Lathrop, D. P. (2011), 'Bi-stability in turbulent, rotating spherical couette flow', *Physics of Fluids* **23**.

Curriculum Vitae

Personal Data

Name	Jakob Kühnen
Date of birth	June 24, 1978
Place of birth	Herdecke (Germany)
Nationality	Austria
Address	Liechtensteinstrasse 63/12, A-1090 Wien

phone: +43 (0)650 635 66 26

e-mail: jakob.kuehnen@tuwien.ac.at

Education

09/09–present	Doctorate in Technical Sciences at the Vienna University of Technology
09/97–03/06	Study of Wirtschaftsingenieurwesen-Maschinenbau (Industrial Engineering) at the Vienna University of Technology, Diploma thesis under supervision of Hendrik Kuhlmann: *Experimental Investigations of Hydrodynamic Instabilities in Triangular Cavities*
10/04–06/05	Masterclass CEE, Department of Strategic Management and Management Control, Vienna University of Economics and Business Administration
08/84–06/97	R. Steiner Schule Wien-Pötzleinsdorf (grammar and high school), Vienna

Army Service

02/98–01/99	Alternative civilian service at the *Multiple Sklerose Gesellschaft*, Vienna

Employment

05/06–present	*Project engineer*, Rolling Mills and Strip Processing Lines, Andritz AG
10/09–present	*Universitätslektor*, Institute of Fluid Mechanics and Heat Transfer, Vienna University of Technology

List of publications

1. L. M. González, M. Ahmed, J. Kühnen, H. Kuhlmann and V. Theofilis, Three-dimensional flow instability in a lid-driven isosceles triangular cavity, Journal of Fluid Mechanics **675**, 369–396 (2011).

2. J. Kühnen and H. Kuhlmann, An experimental investigation of the influence of curvature on localized turbulent spots in transitional pipe flow, 19. Fachtagung 2011 Lasermethoden in der Strömungsmesstechnik, Ilmenau, 06.–08.09.2011, in: *Lasermethoden in der Strömungsmesstechnik 19. Fachtagung 2011* (2011).